TAILORING THE WORK FUNCTION OF SURFACES: EFFECTS OF CHARGE TRANSFER IN SURFACE MODIFIERS ON METALS AND TRANSPARENT CONDUCTING OXIDES

A Dissertation
Presented to
The Academic Faculty

By

Alexander Steven Hyla

In Partial Fulfillment
of the Requirements for the Degree
Doctor of Philosophy in the
School of Chemistry and Biochemistry

Georgia Institute of Technology
May 2017

TAILORING THE WORK FUNCTION OF SURFACES: EFFECTS OF CHARGE TRANSFER IN SURFACE MODIFIERS ON METALS AND TRANSPARENT CONDUCTING OXIDES

Approved by:

Dr. C. David Sherrill, Advisor
School of Chemistry and Biochemistry
Georgia Institute of Technology

Dr. Jean-Luc Brédas, Thesis Advisor
School of Chemistry and Biochemistry
Georgia Institute of Technology
Physical Sciences and Engineering Division
King Abdullah University of Science and Technology

Dr. Seth R. Marder
School of Chemistry and Biochemistry
Georgia Institute of Technology

Dr. Kenneth Brown
School of Chemistry and Biochemistry
Georgia Institute of Technology

Dr. Bernard Kippelen
School of Electrical and Computer Engineering
Georgia Institute of Technology

Date Approved: November 21, 2016

To my entire family, especially my cousin Nick and Aunt Claudia, who were tragically taken too soon.

ACKNOWLEDGEMENTS

First of all, I would like to especially thank my amazing mother, Barb, and father, Gary, without whose love, guidance, and support I would not be here. My life would not have been the same without my two awesome sisters, Chelsea and Lydia, as well. My entire family has always been there to support me and I am eternally grateful for them. I would like to thank Mrs. Kristi Pruss for getting me interested in chemistry in high school. I am extremely grateful for Charles "Chick" Evans, the Evans Scholarship Foundation, and the Western Golf Association for support during my undergraduate career at the University of Michigan.

During my time at Georgia Tech, I have met many people who have made this one of the best experiences of my life. I would like to thank my advisor, Dr. Jean-Luc Brédas, for letting me join his research group and giving me the opportunity to grow and learn as a scientist. I would like to thank my Ph.D. thesis committee members for their guidance and support. The Brédators have always been there to support me, in particular Dr. Paul Winget, Dr. Hong Li, Stephen Shiring, Dr. Alexandr (Sasha) Fonari, and Dr. Yao-Tsung Fu. I need to thank my collaborators, with whom I have grown into the scientist I am today, especially Dr. Anthony Giordano, Hye-Kyung Kim, Dr. Stephen Barlow, Dr. Matthew Gliboff, Dr. Hsiao-Chu Lin, and Yilong Zheng. I would like to thank Erin Gawron, Dale Merz, DJ Crowell, Trent Parker, Shawn and Stephanie Marshall, Allison Harbottle, Hailey Bureau, Dom Sirianni, Brandon Bakr, Dr. Ray Shenje, Rayaj Ahamed, Cynthia Martin, and Dr. Karttikay Moudgil for good times and great memories.

I also need to thank the Atlanta Curling Club for giving me another passion in life, the sport of curling. I am grateful for the friendships of Chris and Hannah Hyde, Dan O'Toole, Becky and Dennis Kalman, Lou Urban, Derek Behmke, and Kael Stilp, along with the rest of the curlers that I have met at bonspiels across the country and learn to curl events.

TABLE OF CONTENTS

LIST OF TABLES

LIST OF FIGURES

LIST OF SYMBOLS AND ABBREVIATIONS

AEY	Auger Electron Yield
AOB	Acridine Orange Base
ARXPS	Angle Resolved X-ray Photoelectron Spectroscopy
BPA(s)	Benzyl Phosphonic Acid(s)
BZ	Brillouin Zone
Cp	Cyclopentadiene
Cp*	Pentamethylcyclopentadiene
CPD	Contact Potential Difference
DFT	Density Functional Theory
DFT-D2	Dispersion correction developed by Grimme for DFT, includes pairwise interactions
DFT-D3	Dispersion correction developed by Grimme for DFT, includes three-body interactions
DMOAP	N,N-dimethyl-N-octadecyl(3-aminopropyl)trimethoxysilyl chloride silane
DOS	Density of States
DSC	Detergent Solvent Cleaned
DTC	N,N-Dialkyl Dithiocarbamate
eV	Electronvolt
E_F or E_{Fermi}	Fermi Level Energy
E_{vac}	Vacuum Energy
E_{VBM}	Energy of the Valence Band Minimum
EXAFS	Extended X-ray Absorption Fine Structure Spectroscopy
FAQ	Octafluoroanthraquinone
F_4-TCNQ	2,3,5,6-tetrafluoro-7,7,8,8-tetracyanoquinodimethane

GGA	Generalized Gradient Approximation
GZO	Gallium-doped Zinc Oxide
HOPG	Highly Oriented Pyrolytic Graphite
IDipp	1,3-bis(2,6-diisopropylphenyl)-1,3-dihydro-2*H*-imidazol-2-ylidene
IiPr	1,3-diisopropyl-1,3-dihydro-2*H*-imidazol-2-ylidene
iPr_2bimy	1,3-Diisopropyl-1,3-dihydro-2*H*-benzo[*d*]imidazol-2-ylidene
IrCpCp*	Pentamethyliridocene
ITO	Indium Tin Oxide
k_B	Boltzmann's constant
KP	Kelvin Probe
KS	Kohn-Sham
L(S)DA	Local (Spin) Density Approximation
MV0	Neutral Methyl Viologen
NEXAFS	Near Edge X-ray Absorption Fine Structure Spectroscopy
NHC	N-Heterocyclic Carbene
NMA	9,9'-ethane-1,2-diylidene-bis(N-methyl-9,10-dihydroacridine)
OFETs	Organic Field Effect Transistors
OLEDs	Organic Light-Emitting Diodes
OPVs	Organic Photovoltaic Devices
PA(s)	Phosphonic Acid(s)
PAW	Projector Augmented Wave
PBE	Generalized Gradient Approximation of Perdew, Burke, and Ernzerhof
$PC_{61}BM$	[6,6]-phenyl-C_{61}-butyric acid methyl ester
PDI-PA(s)	Perylene Diimide Phosphonic Acid(s)
PDOS	Projected Density of States

PEI(E)	Polyethylenimine (Ethoxylated)
PTCDA	Perylene-3,4,9,10-tetracarboxylic dianhydride
PTCDI or PDI	Perylene-3,4,9,10-tetracarboxylicdiimide
PVDF-HFP	Poly(vinylidene fluoride-co-hexafluoro-propylene) co-polymer
SAM(s)	Self-Assembled Monolayer(s)
SIDipp	1,3-Bis(2,6-diisopropylphenyl)imidazolidin-2-ylidene
SIiPr	1,3-diisopropyl-1,3-dihydro-2*H*-imidazolidin-2-ylidene
TDAE	Tetrakis-(dimethylamino)ethylene
TEY	Total Electron Yield
THF	Tetrahydrofuran
TTF	Tetrathiafulvalene
U	Hubbard Parameter; usually DFT+U
UPS	Ultraviolet Photoelectron Spectroscopy
UV	Ultraviolet
VASP	Vienna Ab Initio Simulation Package
VESTA	Visualization for Electronic and Structural Analysis Program
WF or Φ	Work Function
XANES	X-ray Absorption Near Edge Spectroscopy
XPS	X-ray Photoelectron Spectroscopy
ZnO	Zinc Oxide
6Dipp	1,3-Bis(2,6-diisopropylphenyl)tetrahydropyrimidin-2(1*H*)-ylidene
ρ	Charge Density
$\Delta\Phi$	Change in Work Function; Work Function Modification
$\Delta\rho$	Change in Charge Density

SUMMARY

There has been much research into modifying the work function of metals and transparent conducting oxides for use in organic optoelectronic device applications, particularly as electrode materials in organic photovoltaic devices (OPVs) and organic light-emitting diodes (OLEDs). Materials' work functions may need to be raised or lowered depending on the desired application. OPVs and OLEDs require a low work function electrode to serve as the electron selective and electron injecting electrode, respectively. Traditional low work function materials are highly reactive to air and water and thus devices that use these materials require encapsulation for the device to operate as intended. Methods for making low work function materials are being examined, such as taking an air-stable, high work function material and using a modifier to lower the surface work function. This method would give a low work function electrode when interacting with the active materials and the material could still behave as a high work function material when interacting with the environment. Increasing the work function of an electrode material is also desirable in order to more efficiently extract holes from OPVs and inject holes into OLEDs. This is generally done with surface modifiers that have an internal dipole moment in which the negative end points away from the surface, in order to increase the electrostatic potential and thus raise the work function. In systems to both raise and lower the work function, charge transfer has been shown to affect the method in which the work function is modified. Charge transfer can be so important in the system that if it is not present, the work function modification will be reduced or the work function may possibly remain unchanged from the unmodified surface.

CHAPTER 1

INTRODUCTION

1.1 Overview

Organic optoelectronic devices, such as organic photovoltaics (OPVs), organic light emitting diodes (OLEDs), and organic field-effect transistors (OFETs), have come a long way since the first reported devices made by Tang *et al.*[1-2] OLEDs are now commonly found in consumer devices, such as in the screens of cell phones and televisions. OPVs have recently broken the 10% efficiency mark[3] and have now been reported to be over 12% efficient.[4] OFETs have charge mobilities that can reach on the order of several tens of $cm^2/V \cdot s$.[5] Organic devices have been investigated because of the tunability of desired properties, possible low production cost of the materials, and the potential to use low cost, large area manufacturing processes, such as printing or roll-to-roll processing.[6]

While the architectures of organic optoelectronic devices consist of layers that perform specific roles, there will always be interfaces between differing materials. These interfaces can be between purely organic layers, or between an organic layer and an inorganic layer; they will determine the morphology of the material to a significant extent, which will in turn determine the properties of the device.[7] If we take the example of an

OPV device, the interface(s), between the donor material and the acceptor material in the active layer is (are) important because it is where excitons, or bound electron-hole pairs, can overcome their Coulombic attraction and become free electrons and holes. Once the electrons and holes are separated, they need to move towards their respective electrodes for extraction, before they undergo a recombination event, such as finding a local energy trap or simply encountering another free charge of the opposite sign, known as bimolecular recombination, which can lead to radiative or non-radiative losses.

A different situation may arise when the active layer meets the electrode. The energy levels of the active layer and the electrode material may not be well-matched, leading to an extraction barrier, or the union of a hydrophobic organic layer with a hydrophilic oxide electrode can cause conformational and morphological changes that may prevent charge extraction/injection.[8] If these occur, the charges may sit at the interface or move back throughout the device where it can then undergo bimolecular recombination. An active area of research to make organic electronic devices more efficient and reduce unwanted energy losses is focusing on modifying the effective work function of the electrode materials, to better match the energy levels of the molecules in the active layer(s) of devices. The work function can be changed by applying surface modifiers, which will be described in more detail below. The method by which the work function is modulated can be related to charge transfer within the surface-modifier system, as shown by the research presented in Chapters 3 through 5 of this Thesis.

1.2 Work Function and Modification

The calculation and measurement of work functions on native (without modification) substrates and on substrates with a surface modifier are central aspects to the work presented in this Thesis. A brief introduction to this topic will include computational methodology as well as experimental techniques to measure work functions and some important reasons why work function modification is important to organic electronic devices. The units for work function which will be used in much of this Thesis are electronvolts (eV); we recall that 1.0 eV is equal to 96.5 kJ/mol, 23.1 kcal/mol, 8066 cm^{-1}, or 1.6×10^{-19} J, and represents the energy of a photon with a wavelength of 1240 nm.

1.2.1 Work Function

The work function (WF or Φ) is defined as the difference between the Fermi level energy and the energy of the vacuum level. The work function of a semiconductor can be defined as the average amount of energy required to remove an electron from a material to bring it to the vacuum level. Thus, thermodynamically, Φ is the work required to remove an electron from the material to a state of rest in the vacuum nearby the surface. The work function is surface and composition-dependent. The same material can have different work functions for different surfaces (crystallographic facets), which can vary from tenths of an eV[9] to around 1 eV.[10] With this in mind, it is important to know which facet is being modified, and thus which facet to model in calculations of the system. Also, the presence of any defects / contaminants / dopants can change the electronic structure of the surface and thus the work function of the surface, as described below in Section 1.2.2.

1.2.2 Physical Principles behind Work Functions and Modification

Electrons obey the Pauli Exclusion Principle, which states that no two identical fermions may simultaneously occupy the same quantum state. Thus, probabilistic analysis pertaining to the distribution of electrons within a system follows Fermi-Dirac statistics. The probability of finding an electron with energy E, P(E), is expressed as:

$$P(E) = \frac{1}{1 + e^{\frac{(E-E_F)}{k_B T}}} \tag{1.1}$$

where E_F denotes the Fermi level energy, k_B, the Boltzmann constant, and T, the temperature. The Fermi level energy is defined as the energy where the probability of a state being occupied is one half.[11] The difference between E_F and the energy of the vacuum level, E_{vac}, is the work function, Φ:

$$\Phi = E_{vac} - E_F \tag{1.2}$$

There are two general cases that need to be considered when looking at the density of electronic states, namely how they apply to conductors, such as metals, and semiconductors, such as metal oxides. In the case of metals, the density of states fills up to the Fermi level energy. There is no energy gap between the valence (occupied) levels and conduction (unoccupied) levels; the Fermi level energy occurs at their juncture. This is not the case for a semiconductor where the Fermi level energy appears in the bandgap between the top of the valence band and the bottom of the conduction band.[12] These cases hold true at absolute zero (0 K), but examination of Equation 1.1 shows that this situation is modified at other temperatures. Figure 1.1 shows band diagrams for metals and semiconductors at varying temperatures. These band diagrams illustrate that temperature plays an important role in determining the occupation of states. With temperatures higher than 0 K, the

occupation of charges in the conduction band increases upon promotion from the valence band means it is now possible for some electrons to have energies above the Fermi level energy.

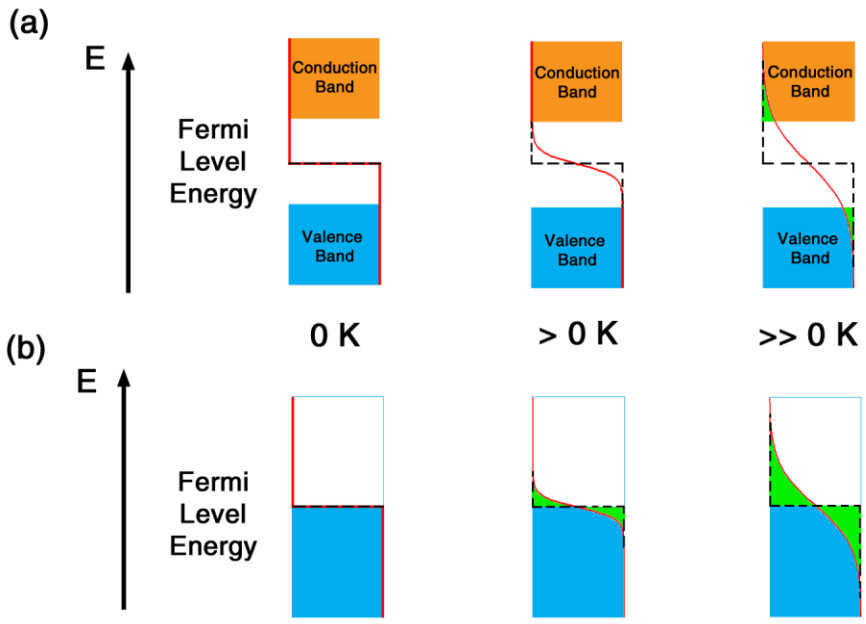

Figure 1.1: Simplified representation of band diagrams for a generic semiconductor (a) and metal (b) at absolute zero (left), a temperature greater than zero (center), and a temperature much greater than zero (right). The red line is representative of the Fermi-Dirac distribution, where the right side of the band denotes fully occupied and the left side denotes fully unoccupied, with the green highlighting changes that occur to the value of the Fermi-Dirac distribution with temperature. Adapted from Nave.[13]

Temperature is not the only way to provide more accessible states in a semiconductor. If an initially highly pure semiconducting material (known as an intrinsic semiconductor) has impurities introduced, the material can become a doped, or extrinsic, semiconductor. The dopant's energy levels being different from the rest of the host semiconductor material, depending on whether the dopant is an electron donor or an

acceptor, the Fermi level energy (that is the chemical potential) adjusts accordingly thus decreasing or increasing, respectively, the distance between the conduction band and the Fermi level energy. This change in Fermi level energy, and therefore in work function, is one of the observables in ultraviolet photoelectron spectroscopy (UPS). Figure 1.2 demonstrates the changes that occur when a semiconductor is doped with either a donor (n-type) or an acceptor (p-type). Doping in general enhances conductivity of a material since it can create free carriers (electrons or holes) in either the conduction band or valence band.

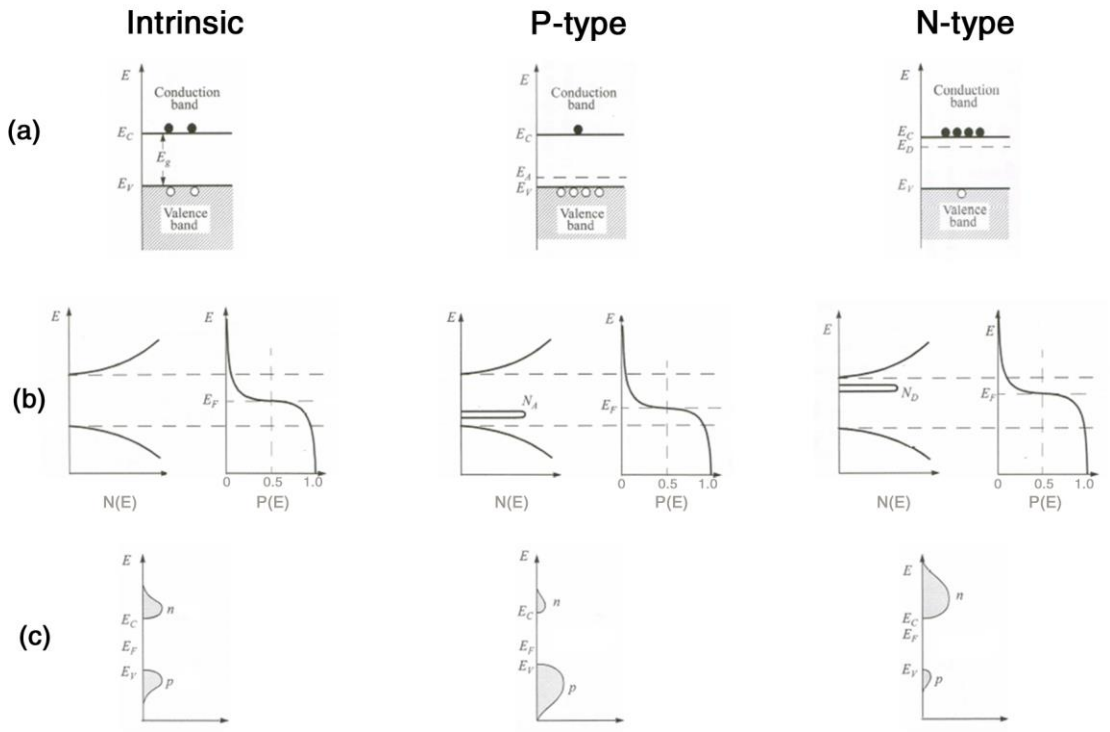

Figure 1.2: Schematic band diagrams (a), density of states (N(E)) and Fermi-Dirac distribution (P(E) as in Equation 1.1) (b) and carrier concentration of electrons (n) and holes (p) for intrinsic, p-type, and n-type semiconductors at thermal equilibrium. E_F is the Fermi level energy, E_g is the band gap of the intrinsic semiconductor, E_A is the energy of the acceptor, which is present at concentration N_A, and E_D is the energy of the donor, which is present at concentration N_D. Adapted from Sze and Ng.[14]

1.2.3 Techniques for Obtaining Work Functions

Work functions may be obtained through experimental methods as well as through calculations. This section will briefly introduce the methodologies and include a description of the results that can be obtained from the technique we present.

1.2.3.1 Experimental Techniques to Obtain Work Functions

There are two commonly used techniques to obtain the work function of a surface, UPS and Kelvin probe (KP). These techniques both give work functions of surfaces, but the Kelvin probe can be performed in air or in vacuum and gives a work function difference with respect to a known standard, whereas ultraviolet photoelectron spectroscopy is generally performed in vacuum and spectra are shifted to match the Fermi edge of a metal surface.[15] A brief overview of each technique will be given below.

1.2.3.1.1 Ultraviolet Photoelectron Spectroscopy

The aim of UPS experiments is to obtain information pertaining to the distribution of electrons in the outermost valence band region of the material. These electrons are responsible for the chemical, magnetic, optical, and mechanical properties of the material.[16] In order to probe these electrons, the sample is illuminated under vacuum with a monochromatic beam of ultraviolet light, usually He I radiation at 21.2 eV[16] or He II radiation at 40.8 eV. The energy available from these photons can only overcome the binding energies of electrons in valence levels of the sample. The emitted electrons are then collected and analyzed, which makes UPS an electron spectroscopy.[17] Commonly, a UPS instrument is combined with an X-ray photoelectron spectroscopy (XPS) instrument,

with the light source changing for the respective techniques. XPS uses a monochromatic Al or Mg Kα light source with energies of 1486.6 and 1253.6 eV, respectively.[17] A general schematic of the UPS/XPS instrument components can be found in Figure 1.3.

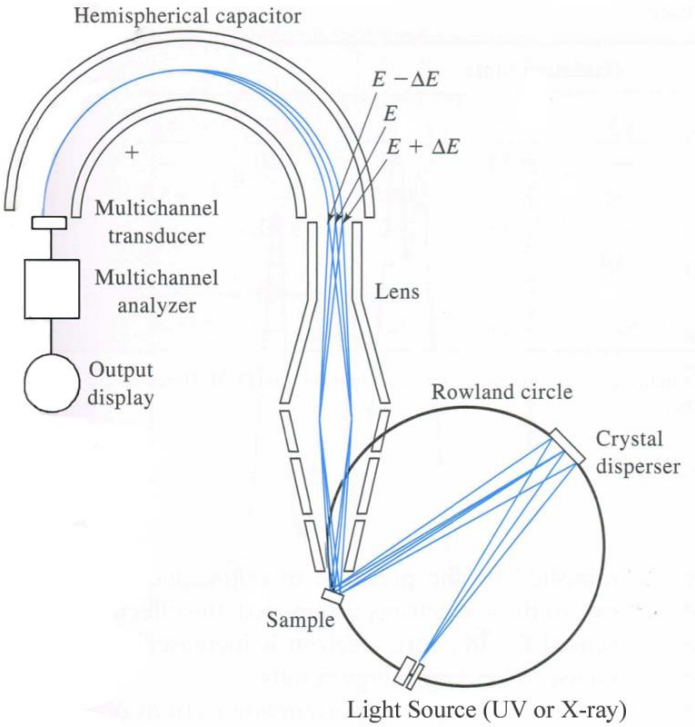

Figure 1.3: General schematic of a UPS or XPS when inside a combined UPS/XPS instrument. Adapted from Skoog, Holler and Crouch.[17]

The spectra obtained from UPS measurements are usually displayed as intensity versus binding energy of the electron, which allows for the identification and quantification of the valence band maximum and the work function of the surface, as shown in Figure 1.4. The WF can be obtained from the following equation:

$$\Phi = \mathrm{E}_{\mathrm{source}} - \mathrm{E}_{\mathrm{S.E.E}} \tag{1.3}$$

where E_{source} is the energy of the radiation source being used (either 21.2 eV for a He I source or 40.8 eV for a He II source) and $E_{S.E.E.}$ is the energy of the secondary electron edge. Secondary electrons are either ejected electrons that have lost energy through inelastic collisions or have gained enough energy to escape following a collision. These secondary electrons make up a largely featureless peak in UPS spectra, with a shape that resembles a Maxwellian distribution,[16] denoted as "Inelastically Scattered Electrons" on the left side of the spectrum in Figure 1.4. The secondary electron edge denotes the energy of electrons that had just enough energy to overcome the work function when they reached the surface.[15] The UPS data presented in this Thesis has been performed by Dr. Anthony Giordano and Hye Kyung Kim, both from the Marder group at Georgia Tech.

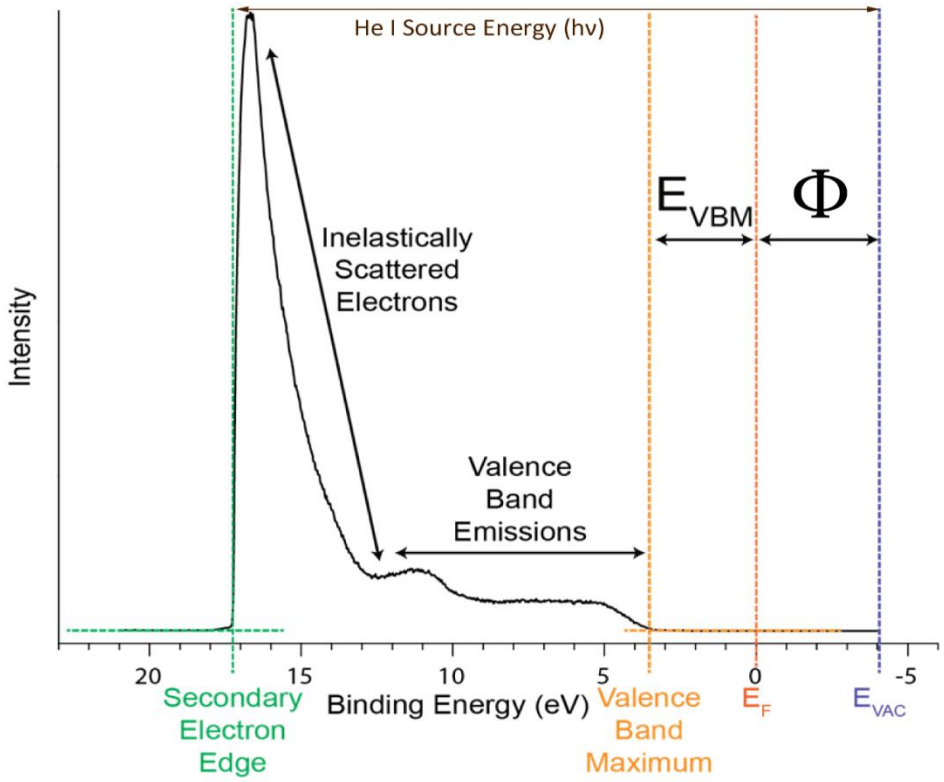

Figure 1.4: Example UPS spectrum of bare zinc oxide (ZnO) with important features denoted. The work function (Φ) and energy of valence band maximum (E_{VBM}) can be directly determined from this spectrum. Spectrum adapted from Giordano.[18]

1.2.3.1.2 Kelvin Probe

Kelvin probe (KP) is another technique used to measure work function by determining the contact potential difference (CPD) between two different materials. The premise of the KP technique relies on the fact that when two materials are brought into contact with each other, the Fermi level energies of the materials will align with each other. This alignment leads to a potential between the two materials, in this case the sample and the probe. The measured quantity is actually the amount of potential required to counteract or nullify the CPD between the sample and the probe.[19] This is shown in Figure 1.5. The measured CPD of the sample is then compared to a surface with a known work function.

Since KP can be performed in air, it has become very popular in recent times. KP thus also requires a surface that has a stable work function in air as the reference. Highly oriented pyrolytic graphite (HOPG) has been used as the reference for KP measurements, as it can be easily prepared by the scotch tape method, and it has a steady work function in air of 4.475 ± 0.005 eV.[19] The KP data presented in Chapter 4 of this Thesis were obtained by Hye Kyung Kim of the Marder group together with Felipe Larrain and Canek Fuentes-Hernandez of the Kippelen group at Georgia Tech.

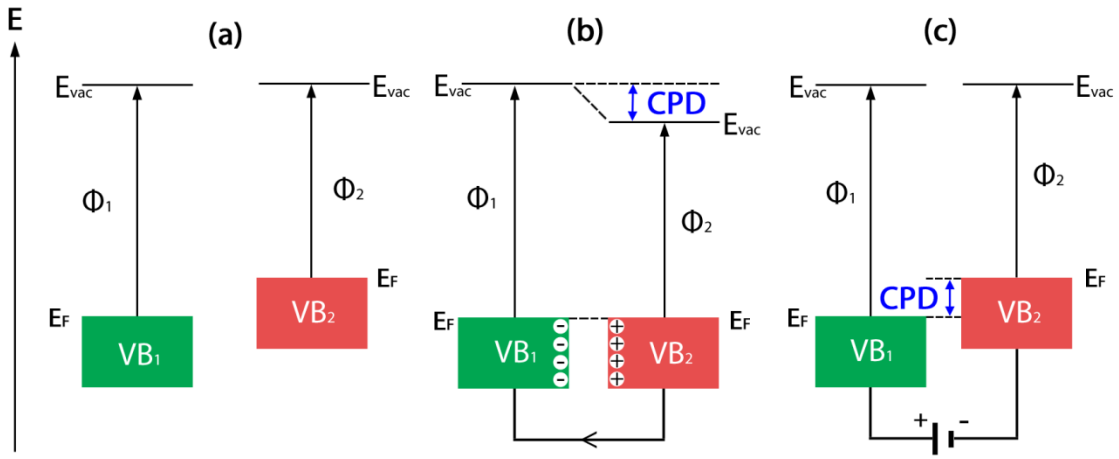

Figure 1.5: Cartoon showing the working principle behind the Kelvin probe. When two metals with different work functions (Φ_1 and Φ_2, respectively) (a) are brought into contact with one another (b), the metals' Fermi level energies align. Electrons flow from the metal with the smaller WF (Φ_2 in this case) to the metal with the larger WF, until an electric field is built up that counteracts the difference in WF. The potential associated with the electric field is known as the contact potential difference (CPD) between the metals. An external potential is applied to the system (c) and at the charge-free point, as determined by an electrometer, the external potential is exactly opposite the CPD between the two metals. Adapted from Schlaf.[20]

1.2.3.2 Computational Methodology to Obtain Work Functions

The method to calculate the work function of a system, either a bare substrate or one that has been surface modified, can be summarized in Equation 1.2, where E_{vac} is the vacuum energy and E_F is the Fermi level energy, defined by Equation 1.1. The Fermi level energy of the system is determined from the occupation of the energy bands and is an important output of the calculation. The vacuum energy is obtained from a plot of the electrostatic potential energy of the system (averaged over the plane of the surface, usually denoted as the xy-plane) versus the axis perpendicular to the surface, usually denoted as the z-axis. The potential along the z-axis will vary throughout the system, due to the atoms in the bulk, at the surface, and from any surface modifiers; above the surface, it eventually reaches a constant value, where the electron is only interacting with vacuum, corresponding to the energy of the vacuum level. The Fermi level energy and the electrostatic potential energy above the surface are combined in Equation 1.2 to obtain the work function.

Once the work functions are computed for the bare surface and a modified surface, the change in work function ($\Delta\Phi$) due to the modification can be compared to the experimental results. It is useful to compare work function changes from both experiments and calculations, because this takes into account any systematic errors in the techniques and any discrepancies in the specific WF values between the methods. For example, in the phosphonic acid (PA) work presented in Chapter 5 in this Thesis, the UPS-measured WF of indium tin oxide (ITO) is 4.6 eV, whereas from the calculations, the ITO WF is 3.2 eV (given the specific model surface used in the calculations), but the trends of the WF modification due to the fluorinated benzylphosphonic acid (BPA) modifiers are similar for both the experimental and calculated results.

When calculations are performed on a system with a surface modifier, such as a self-assembled monolayer or molecular dopant, there are different aspects which can cause changes in work function, such as how the surface atoms react to the modifier or how the modifier can alter the effective vacuum level on top of the system. These different components can be separated and quantified by using a work function modification breakdown scheme[21-26] which will be described in more detail below.

1.2.3.2.1 Work Function Modification Breakdown

The work function modification breakdown scheme, [24-25] as used in this Thesis, has three separate components that can each contribute to the work function of the system when a surface modifier is present. These include: (i) the change in WF due to geometric (and thus electronic) reorganization of the surface after interacting with the modifier, denoted as $\Delta V_{geom.}$; (ii) the effect of the molecular dipole moment of the modifier (component normal to the surface) after interaction, denoted as $\Delta V_{mol.}$; (iii) and the effect of the charge redistribution at the very interface due to the interaction of the surface with the modifier, known as the interface dipole, denoted as $\Delta V_{int.\ dip.}$. The sum of these components:

$$\Delta\Phi_{breakdown} = \Delta V_{int.\ dip.} + \Delta V_{geom.} + \Delta V_{mol.} \quad (1.4)$$

is usually very close to the $\Delta\Phi$ obtained directly from the difference in work functions between the pristine surface and the modified surface. Literature shows that different surface modifiers can have different ratios of these three components while still showing similar changes in work function. The simple aliphatic amine, polyethylenimine (ethoxylated), PEI(E), was shown to decrease the work function of many different surfaces by 0.7-1.8 eV using both KP and UPS.[26] Calculations of this system showed that the

interface dipole and the molecular dipole moment had contributions of the same order of magnitude (-0.8 eV and -0.5 eV, respectively, on the Au(111) surface). Fluorinated benzyl phosphonic acids (PA) on zinc oxide (ZnO)[25] were shown to have interface dipoles and molecular dipoles that, depending on the binding mode and the composition of the PA modifier, varied from approximately equal in magnitude but opposite in sign, to having the interface dipole component four times as large as the molecular dipole component, with both having the same sign. The work function decreases observed in these calculations were -0.24 eV to -1.38 eV, as a function of the exact nature of the PA. These benzyl PA systems also had a large contribution from the rearrangement of the surface (at least -0.8 eV), which was not seen in the PEI(E) work.

1.2.4 Examples of Work Function Modification

There has been much effort to tune the effective work function of materials to allow for better energy level alignment between electrode materials and organic electronic active layers. Tuning the work functions of the electrode materials can allow for better charge collection or injection depending on the device (OPVs and OLEDs, respectively) and this can reduce potential recombination from occurring at the interface with the electrode material and reduce the over-potential required to operate the device. Depending on the desired application, the work function of the electrode must either be increased or decreased and some examples of each will be briefly discussed below.

1.2.4.1 Increasing the Work Function

Many of the active layers in organic electronic devices, particularly OLEDs, have materials with active (occupied) energy levels on the order of 5 - 6.5 eV.[27] The ideal anode material would have a work function close to this energy level to prevent losses or chances for recombination due to inefficient hole extraction. In order to tune the work function to match the desired energy levels, different surface preparation schemes can be undertaken or surface modifiers may be employed. These modifiers can be broadly divided into chemisorbed, or chemically bound, and physisorbed, or bound through non-covalent interactions to the surface.

1.2.4.1.1 Surface Treatments for Increasing Work Function

There are a few processes that can be applied directly to the surface that will increase the work function. One of the most common processes is plasma treatment. Treatments with oxygen plasma or UV-ozone plasma can increase the work function of ITO by 100-300 meV.[28] Chlorination of ITO has been used to raise the work function from 4.7 eV to around 6.1 eV.[27] The chlorine atoms have been shown to be bound to the indium atoms, replacing oxygen atoms in the surface layer, thus creating dipoles at the surface, which increases the work function.[27]

1.2.4.1.2 Chemisorbed Work Function Modifiers for Increasing Work Function

Self-assembled monolayers, or SAMs, have been used to modify the properties of surfaces for many years now. Thiol SAMs on noble and coinage metals have been extensively researched and a review by Love *et al.* goes through most of the early work.[29]

Metal oxides have different chemistry for binding SAMs and thus require different docking groups. The surface modifications of ITO by chemisorbed phosphonic acid SAMs have been used [23-24, 30-39] to realize relatively large changes in Φ, of up to 1 eV.[30] ZnO[25] and gallium doped zinc oxide[40] (GZO) have also been modified with PA SAMs. Both the magnitude and direction of the modification can be controlled by varying the concentration of the modifier as well as the molecular docking and head groups. In the case of PA SAMs, the positioning of electron donating/withdrawing groups around an aromatic or aliphatic core can systematically vary the molecular dipole moment, which results in a change of the effective vacuum level of the modified system and thus the work function.

1.2.4.1.3 Physisorbed Work Function Modifiers for Increasing Work Function

There has been a lot of research on chemisorbed modifiers, but there has also been interest in using physisorbed molecules to increase the work function of surfaces. The molecule 2,3,5,6-tetrafluoro-7,7,8,8-tetracyanoquinodimethane (F_4-TCNQ) has been used to increase the work function of gold, silver, and copper surfaces by as much as 0.85 eV.[41-44] Octafluoroanthraquinone (FAQ) has also been shown to both decrease and increase the work function of Ag(111) surfaces with changes in the thickness of the FAQ layer.[45] Molecular oxygen has been shown to increase the work function of Cu(110) at low exposures.[46] A highly fluorinated co-polymer, poly(vinylidene fluoride-co-hexafluoro-propylene) (PVDF-HFP), has also been shown to increase the work function of metals and metal oxides by as much as 0.95 eV.[47]

1.2.4.2 Decreasing the Work Function

One part of the processing of organic optoelectronic devices, such as OPVs and OLEDs, which is still inhibiting low cost production, is the fabrication of a low work function electrode for electron injection or collection from the electron transport levels of organic semiconductors. Traditionally, low-Φ metals, e.g. Ca or Mg, are deposited on top of the organic semiconductor layer under inert atmosphere conditions,[26] because these materials are highly reactive and are easily oxidized in ambient conditions. In order for the device to operate in these conditions, encapsulation or protection of this electrode is usually required, adding additional production steps and cost to the device. Thus, alternative methods for producing low-Φ electrodes are desirable.

1.2.4.2.1 Surface Treatments to Decrease Work Function

There are a few surface treatments that can be performed, besides specifically applying a molecule, to decrease the work function of surfaces. Mechanical cleaning, such as rubbing the surface with ethanol-impregnated paper or ethanol-impregnated Teflon, were each shown to decrease the work function of ITO by 0.3 eV.[48] Ultrasonic cleaning of ITO in acetone followed by soaking in iso-propanol decreased the work function by 0.15 eV.[48-49] Sputtering of Ar^+ ions caused a decrease of the work function of ITO of around 0.4 eV, due to the removal of oxygen from the surface.[49] ZnO treated with hydrogen plasma had its work function decreased by over 1 eV, by increasing the charge carrier density, leading to n-doping and a lifting of the Fermi level energy.[50]

1.2.4.2.2 Chemisorbed Work Function Modifiers for Decreasing Work Function

As mentioned above in Section 1.2.4.1.2, there has been success in using self-assembled monolayers to increase the work function of optoelectronic materials such as ITO and ZnO. Recently there has been work to use SAMs and lower the work function of gold, silver, and ITO surfaces. On gold, n,n-dialkyl dithiocarbamates (DTCs) have been used to reduce the work function from 5.2 eV to 3.2 ± 0.1 eV, attributable to a combination of the bond (interface) dipole and the intrinsic molecular dipole.[51] DTCs with differing R-groups were used to obtain gold and silver surfaces with work functions that are tunable over a range of 1.6 eV and reach as low as 3.1 eV.[52-53] Again on both gold and silver surfaces, two carboranethiol isomers were used to raise and lower the work functions of the metals by 0.4 eV each, depending on the mixture of the isomers applied to the surfaces.[54] Since their first use by Nuzzo *et al.*,[55] thiolates have become the most widely used components for SAMs on gold; alkanethiolate monolayers typically reduce the WF of gold to ca. 4 eV, with the exact value depending on the alkyl chain and the measurement technique.[56-58] A very low WF of 1.6 eV has recently been determined using the field-emission properties of Au-coated nanowires with a [121]tetramantane-2-thiolate SAM; however, this value is attributable to formation of the radical cation of the modifier at the tip of the nanowires, and a typical alkylthiolate SAM WF value of ca. 4 eV was found by UPS.[58] In a bio-inspired work, the amino acids L-arginine and L-lysine were applied to an ITO surface and bound through the carboxylic acid. The work function decreased from around 4.7 eV to 2.5 eV for lysine and 3.0 eV for arginine.[59] Acridine orange base (AOB) modified with a propyltrimethoxysilane binding group has been shown to decrease the work function of ITO by as much as 0.8 eV.[60]

1.2.4.2.3 Physisorbed Work Function Modifiers for Decreasing Work Function

One of the most successful strategies for decreasing the work function is the deposition of a thin layer of a polymer containing simple aliphatic amine groups onto the conductor surface. Zhou *et al.* introduced a "universal" method for decreasing the Φ of different conducting electrodes using commercially available polymers of aliphatic amine groups, denoted as PEI(E).[26] For a large variety of conducting surfaces, including metals, metal oxides, polymers, and graphene, it was found that the PEI(E) was physisorbed and could reduce the work function of different surfaces by as much as 1.8 eV. Such a large work function decrease has been analyzed by density functional theory (DFT) calculations for zinc oxide and gold surfaces and can be generalized to other conducting surfaces, where the total work function decrease was shown as the contribution of interface and molecular dipoles aligned in a cooperative fashion.[26]

Another approach, based on a redox-active material, was taken by Osikowicz *et al*. Tetrakis-(dimethylamino)ethylene (TDAE) was deposited on ITO and led to a Φ decrease of 0.9 eV, attributed to a double electron transfer to the ITO surface.[61] TDAE was also used to decrease the Φ of gold by 1.3 eV, originating from a single electron transfer from TDAE to the gold surface.[62] Bröker *et al.* reported a reduction of the Φ of gold by 2.2 eV by an air stable molecular donor layer composed of neutral methyl viologen (MV0), which underwent electron transfer with the gold surface.[63] Hofmann *et al.* employed viologen and tetrathiafulvalene (TTF) to reduce Φ of gold, silver, and copper by as much as 1.2 eV.[64] Bröker *et al.* reported reduction of the Φ of Au(111), Ag(111), and Cu(111) by as much as 1.4 eV with a molecular donor layer composed of 9,9'-ethane-1,2-diylidene-bis(N-methyl-9,10-dihydroacridine) (NMA).[65] Li *et al.* utilized acridine orange base (AOB) as an n-type

dopant to reduce the Φ of gold by 1.9 eV;[66] this Φ reduction is accredited to the formation of an interface dipole, caused by a single electron transfer from the AOB to the gold substrate.

Redox-active, organometallic sandwich complexes have been investigated more recently and can be stronger reductants than TDAE, MV0, or AOB.[67-74] The major advantage of such compounds is that they can be applied as air- (and solution) stable dimers, and can be solution deposited. Upon reaction with an appropriate acceptor, two different mechanisms may occur: (i) either cleavage of the dimer followed by electron transfer from monomer to acceptor; or (ii) electron-transfer reaction between the dimer and the acceptor followed by dissociation of the dimer cation.[67-69] The redox activity of these compounds originates from the conversion of a ligand-centered radical with η^4-Cp (η^5-Cp*)/η^5-Cp (η^4-Cp*) coordination to a metal-centered radical with η^5-Cp (η^5-Cp*) coordination. With a Group-8 central atom, the metallocene complex formally carries 19 electrons, and consequently has a low ionization potential. These sandwich compounds have been used to reduce the Φ of ITO,[71-72, 74] ZnO,[71-72] gold,[71, 74] and graphene[70] by as much as ca. 1.9 eV.

Recently, there have been many reports of additional molecules used in order to lower the work function of electrode materials. Donor-acceptor small molecules have been shown to reduce the work function of gold by 0.1 to 0.3 eV.[75] N,N-dimethyl-N-octadecyl(3-aminopropyl)trimethoxysilyl chloride silane (DMOAP) doped [6,6]-phenyl-C_{61}-butyric acid methyl ester ($PC_{61}BM$) was used to lower the work function of silver from 4.64 eV to 3.87 eV for better electron extraction from an undoped $PC_{61}BM$ electron accepting layer in perovskite solar cells.[76] A review of fullerene derivatives as acceptor

molecules and cathode buffer layers in organic and perovskite solar cells shows that many of these molecules can lower the work functions of metals and metal oxides.[77] Also a DFT study has shown that the WF of Au(111) modified with an N-heterocyclic carbene, namely 4-(adamantan-1-yl)-1,3-dihydro-2*H*-imidazol-2-ylidene or its *N,N'*-diisopropyl analogue, could be reduced from 5.25 eV down to ca. 3.8 eV.[78]

1.3 Additional Experimental Methods for Studying Surfaces

While the work function is an important experimental observable for surfaces, there are other aspects that may be experimentally probed that can help give a greater understanding of the chemistry and physics of the surface, as well as insight into interactions that may occur between the substrate and surface modifiers. Two techniques in particular have been used in the work presented in this Thesis and will briefly be introduced. These include X-ray photoelectron spectroscopy (XPS), as mentioned briefly in Section 1.2.3.1.1, for surface composition and characterization, and near-edge X-ray absorption fine structure spectroscopy (NEXAFS), for modifier orientation on the surface.

1.3.1 X-ray Photoelectron Spectroscopy

X-ray photoelectron spectroscopy is a technique in which a sample is irradiated with high-energy X-ray radiation, higher in energy than the binding energy of core-level electrons of the atoms present in the sample[16]. Since the positions of core levels are unique to each element, the energies at which the electrons are released are characteristic of the types, and even the electronic shells, of the elements, from which the electrons originated in the sample. These electronic binding energies can be compared to standard binding

energies of pure elements to determine the presence of an element in the sample. The ratios of peaks in the XPS spectra can be used to determine the relative abundances of different elements in the sample.[71, 79] The basic set up for an XPS measurement is very similar to the set up for a UPS measurement, as shown in Figure 1.3 with the appropriate X-ray light source for this technique, such as a monochromatic Al or Mg Kα sources.[17]

Irradiation with X-rays can cause two different emission processes to occur simultaneously, emission of photoelectrons and emission of Auger electrons. Photoelectrons are primary electrons that are removed due to the absorption of energy from the X-ray irradiation which is greater than the binding energy of the electron, while Auger electrons are secondary electrons that are emitted in a two-electron process that occurs during the reorganization of electrons following the removal of a core electron. In order to fill the hole left by the emission of a core level electron, a higher-lying electron falls into the hole, releasing energy. This energy is usually released in the form of a photon, but sometimes it can be absorbed by another electron in the same atom. If this energy is greater than the binding energy of the second electron, then that second electron is emitted, which is known as an Auger electron. The two processes are shown below in Figure 1.6. The energy of Auger electrons are independent of the energy of the photon or electron that created the original vacancy in a deeper energy level.[17] While both photoelectrons and Auger electrons are emitted and this can complicate the interpretation of spectra, Auger electrons lines can help to identify different species of the same atom type present in the sample.[16]

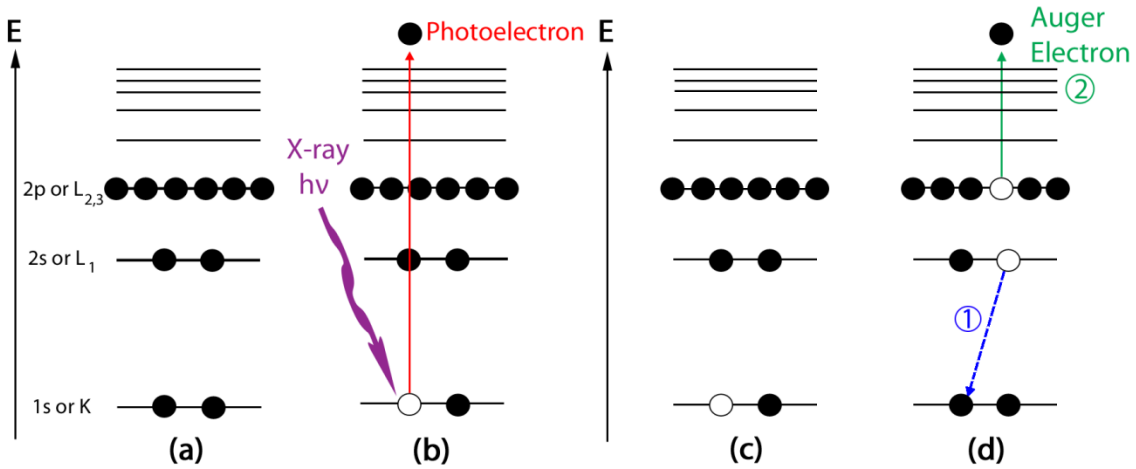

Figure 1.6: Cartoon describing the difference between the emission of a photoelectron (a, b) and emission of an Auger electron (c, d). In the ground state (a), all of the core electrons are present. Upon radiation with X-rays (b), a core electron (a 1s electron in this case) can absorb enough energy to overcome the binding energy and is emitted from the atom, leaving a hole behind in its place. Auger electrons occur when the electrons reorganize to fill the hole from the photoelectron (c). A higher energy electron will fall into the photoelectron hole and will give off energy. The energy is released in the form of a photon, equal to the difference in energy levels, but sometimes it is absorbed by another electron in the same atom, causing the second electron to overcome its binding energy and be emitted as an Auger electron (d). Adapted from O'Connor *et al.*[16] and Skoog *et al.*[17]

Once the identity of the atoms in a sample is confirmed by XPS, the relative compositions and even the molecular coverage of adlayers can be obtained from the XPS spectral lines of selected elements. The calculation of relative compositions is obtained by simply taking a ratio of the area under the spectral line(s) for the desired elements, assuming that both elements have known X-ray absorption cross sections. The composition of the interfacial region can be elucidated through the use of angular variations of the XPS measurements, sometimes denoted in literature as angle-resolved XPS or ARXPS. When signal detection is close to the plane of the surface, the signal will be more representative of the surface than the bulk. Systematically changing the angle of irradiation and detection can create a composition depth profile of the sample.

The calculation of molecular coverage requires more information than just the ratio of spectral peak areas. This technique works especially well if an element in the adlayer is not present in nor a common contaminant for the surface under study. The aforementioned ratio of spectral peak areas is used in conjunction with knowledge of the area of the sample that is being irradiated (such as through a surface structural model), the inelastic mean free path, λ_m, of the electrons coming from the sample (usually around 0.5 – 2.0 nm for X-rays in the energy range of 100-1200 eV)[16], as well as a model of the surface. The number of a certain atom type (usually an atom only found in the surface) within the volume than can be accessed by the X-ray beam can be compared to the ratio of spectral peak areas, along with the surface structural model, to give an idea of the relative quantity of atoms probed of the second type of element (usually found only in the adlayer). The volume of the X-ray beam can be calculated as the area of irradiation × escape depth, λ (where $\lambda = \lambda_m \cos\theta$ and θ is the angle of emission with respect to the surface normal)[16]. Fluorine atoms show up very intensely in XPS and are not commonly found as a contaminant on surfaces, which makes them a good choice to compare against the spectral peak area(s) of a surface element.

In addition to the coverage determination and relative composition, XPS is useful in distinguishing the same element in different chemical environments, in different oxidation states, or in different lattice sites.[16] This is due to the changes in binding energy of the core electrons that accompany changes in the environment of the element. These changes in binding energies are known as chemical shifts,[16] or core-level shifts. Core-level binding energies can be calculated; however, in a number of instances the calculated *absolute* binding energy values have no physical meaning,[80] because –for instance, in the implementation in VASP– other core electrons are not allowed to relax. Differences in

binding energies are compared versus the experimentally observed core-level shifts from XPS. The XPS measurements presented in this Thesis were performed by Dr. Anthony Giordano and Hye Kyung Kim, both from the Marder group at Georgia Tech.

1.3.2 Near-Edge X-ray Absorption Fine Structure Spectroscopy

Near-edge X-ray absorption fine structure spectroscopy, or NEXAFS, along with extended X-ray absorption fine structure spectroscopy (EXAFS) make up the broader term of X-ray absorption fine structure spectroscopy (XAFS). NEXAFS is sometimes referred to as X-ray absorption near edge spectroscopy, or XANES.[16] NEXAFS typically describes soft X-ray absorption spectra while XANES is associated with hard X-ray spectra.[81] NEXAFS focuses on the energy range from close to the absorption edge to about 50 eV above this edge, while EXAFS examines the region above 50 eV. The NEXAFS energy region is usually dominated by transitions to unfilled molecular orbitals and multiple scatterings.[16] By varying the angle of the irradiation on a sample with an adlayer, the intensity of these transitions will change and this angular dependence can be used to calculate the orientation of the adlayer.

NEXAFS measurements have to be performed at a synchrotron beamline. The synchrotron beamline is polarized, which means that only the molecular orbitals that are in-plane with the polarized light will be excited. In practice, the sample is placed on an adjustable platform in order to obtain different angles of incidence relative to the beamline. Once the sample is in place, the X-ray energy is scanned while the intensity of the absorbed X-rays is recorded.[81] There are a few methods of measuring the X-ray absorption in NEXAFS experiments, including transmission and electron yield, often called total

electron yield (TEY). Transmission experiments require that the sample be a thin foil, whereas TEY experiments can be performed with thicker samples. When performing TEY experiments, the X-ray absorption is measured indirectly through the photoelectrons produced. There is a measurement that comprises a subset of the TEY experiment, denoted Auger electron yield (AEY), because a different type of electron dominates the measurement. As mentioned above in Section 1.3.1, X-rays are absorbed by core electrons and if there is a particular rearrangement of electrons and absorption of energy, an Auger electron can be formed which is then emitted from the sample. Auger electron decay is dominant over X-ray fluorescence in the soft X-ray region.[81] The intensity of emitted Auger electrons is directly related to the X-ray absorption process.[81] As Auger electrons leave the sample, they can cause scattered secondary electrons to be emitted, which dominate the TEY intensity. The electrons that are measured in the TEY come from several scattering events, which result in electrons that have enough energy to overcome the particular electron's binding energy. These electrons generally come from a depth of around a few nanometers, because deeper electrons lose too much energy to escape. AEY electrons generally come from the top nanometer of the sample making these measurements highly surface sensitive, similar to XPS.

Once the measurements of AEY and TEY are performed at various angles of incidence, the angle of the transition dipole moment with respect to the normal to the surface (φ) can be calculated using the peak areas ($I_V(\varphi)$) at the measured angles of incidence (α) [82-83] and the beamline linear polarization (β):

$$I_V(\varphi) \propto \frac{\beta}{3}\left(1 + 0.5(3\cos^2(\varphi) - 1)(3\cos^2(\alpha) - 1)\right) + \frac{(1-\beta)}{2}\sin^2(\alpha) \qquad (1.5)$$

This equation assumes that there is no preferred orientation of the monolayer within the plane and is an average over the azimuthal orientation.[83] Since there will most likely be local variations of the tilt angle of the molecules with respect to the surface normal, due to surface roughness or changes in binding configuration, the calculated angle, φ, is actually a convolution of the distribution of angles, specifically the expectation value of $\cos^2(\alpha)$.[82] The expectation value also means that if there is no order to the system, or if there are only random orientations of the molecules in the monolayer, the calculated angle will be 54.7°, denoted as the magic angle. Results in this Thesis were performed by Dr. Matthew Gliboff of the Ginger group at the University of Washington and are presented as the average and the uncertainty due to systematic errors in background subtraction and uncertainty of beam polarization.[84] In general, the farther away that the measured angle is from the magic angle, the more the calculated orientation can be trusted as the representation of the distribution of tilt angles for a well-ordered system. A well-ordered system should also show strong angular dependence in the measured peak areas, as shown below in Figure 1.7a. Figure 1.7b shows fits of Equation 1.6 with different angles, α, in order to determine the orientation of the F_{13}OPA modifier, which is shown in Figure 1.7a. The difference in orientations from fitting Equation 1.6 to AEY and TEY data is included in the uncertainty of the measurement.

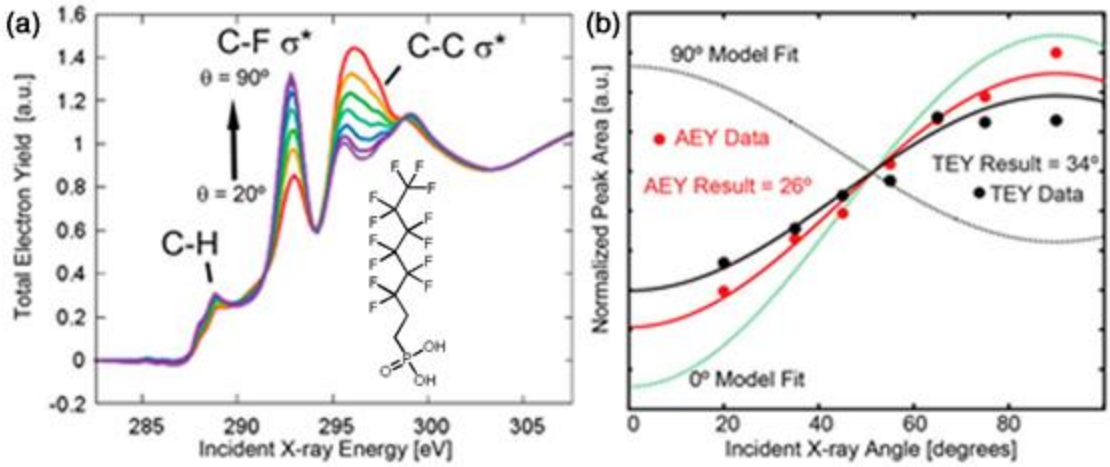

Figure 1.7: NEXAFS TEY spectra of F_{13}OPA on ITO at incident angles of θ = 20°, 35°, 45°, 55°, 65°, 75°, and 90°. The angular dependence of the C−F σ* feature is highlighted. (a) The angular dependence of the peak area normalized by the edge step under the C−F σ* feature is highlighted. (a) The angular dependence of the peak area normalized by the edge step under the C−F σ* feature for both TEY (black) and AEY (red) data. The model fits for α = 0° (dotted green line) and 90° (dotted black line) as well as the best fit of the model to the data (solid lines) are included. (b) Adapted from Gliboff *et al.*[82]

1.4 Thesis Outline and General Overview

This general introduction to work function, including analytical techniques and examples of work function modification, serves as the gateway to the later Chapters. The basic concepts discussed within this Chapter underpin the concepts and studies that will be explored in greater detail throughout the subsequent Chapters. Our goal of this Thesis is to highlight and understand the impact of charge transfer in modifying the work function of electrode materials. While each of the projects found in Chapters 3 – 5 use different molecules and even for different purposes, they each are based on systems where charge transfer between the molecule and the surface influences how the work function is modified in these systems.

In Chapter 2, a brief background to the computational methods used to complete the work in this Thesis will be given. We begin with the Schrödinger equation and a few

of the approximations that are generally made in solving it, the Hartree-Fock equations, and then move on to density functional theory (DFT). As the work presented in this Thesis uses periodic systems, an introduction to plane wave DFT will be given, including pseudopotentials, symmetry in the periodic systems, smearing methods, and plane waves, in general.

Chapter 3 highlights research that was a collaboration between members of the Marder and Brédas groups at Georgia Tech. The purpose of this chapter is to examine the nature and mechanism of work function modification of an organometallic sandwich complex, namely pentamethyliridocene (IrCpCp*), on indium tin oxide and gold surfaces. Organometallic sandwich complexes have been shown to be stronger reducing agents than other molecules used in literature. The effects of the monomer, dimer and hydrogen abstraction monomers on the work function and the methodology of the change in work function will be discussed.

In Chapter 4, another collaboration between the Marder, Kippelen, Sadighi, and Brédas groups sought to understand the mechanism of work function modification for *N*-heterocyclic carbenes (NHC) with varying substituent groups and the effect of differing heterocycle structures on gold surfaces. The ability of NHC modified electrodes to behave as electron-injecting contacts in diode devices will also be examined.

Chapter 5 presents research to determine the effects of the strength of electron-withdrawing groups on phosphonic acids, on the work function modification of indium tin oxide surfaces. The effect of charge transfer in the system can be seen when comparing the dipole moment of the modifiers with work function increases, compared to literature trends.

Lastly, Chapter 6 discusses future works and the broader impacts of the results presented in this Thesis.

1.5 References

1. Tang, C. W. "Two-layer organic photovoltaic cell." *Appl. Phys. Lett.* **1986,** *48*, 183-185.

2. Tang, C. W.; VanSlyke, S. A. "Organic electroluminescent diodes." *Appl. Phys. Lett.* **1987,** *51* (12), 913-915.

3. NREL Best Research-Cell Efficiencies Graph. http://www.nrel.gov/ncpv/images/efficiency_chart.jpg (accessed October 11, 2016).

4. Heliatek "Heliatek consolidates its technology leadership by establishing a new world record for organic solar technology with a cell efficiency of 12%." http://www.heliatek.com/en/press/press-releases/details/heliatek-consolidates-its-technology-leadership-by-establishing-a-new-world-record-for-organic-solar-technology-with-a-cell-effi January 16, 2013.

5. Takeya, J.; Yamagishi, M.; Tominari, Y.; Hirahara, R.; Nakazawa, Y.; T.;, N.; Kawese, T.; Shimoda, T.; Ogawa, S. "Very high-mobility organic single-crystal transistors with in-crystal conduction channels." *Appl. Phys. Lett.* **2007,** *90* (10), 102120(1-3).

6. Khan, S.; Lorenzelli, L.; Dahiya, R. "Technologies for Printing Sensors and Electronics over Large Flexible Substrates: A Review." *IEEE Sens. J.* **2015,** *15* (6), 3164-3185.

7. Méndez, H.; Thurzo, I.; Zahn, D. R. T. "Experimental study of charge transport mechanisms in a hybrid metal/organic/inorganic device." *Phys. Rev. B* **2007,** *75*, 045321(1-14).

8. Brédas, J.-L.; Norton, J. E.; Cornil, J.; Coropceanu, V. "Molecular Understanding of Organic Solar Cells: The Challenges." *Acc. Chem. Res.* **2009,** *42* (11), 1691-1699.

9. Fall, C. J.; Binggeli, N.; Baldereschi, A. "Work Functions at Facet Edges." *Phys. Rev. Lett.* **2002,** *88* (15), 156802 (1-4).

10. Yamamoto, Y.; Miyokawa, T. "Emission characteristics of a conical field emission gun." *J. Vac. Sci. Technol. B* **1998,** *16* (5), 2871-2875.

11. Fraser, D. A., *The physics of semiconductor devices*. 2nd ed.; Oxford University Press: Oxford, United Kingdom, 1979.

12. Kittel, C., *Introduction to Solid State Physics*. 8th ed.; Wiley: Hoboken, NJ, 2005.

13. Nave, C. R. Fermi Level and Fermi Function. http://hyperphysics.phy-astr.gsu.edu/hbase/solids/Fermi.html (accessed October 30, 2016).

14. Sze, S. M.; Ng, K. K., *Physics of Semiconductor Devices*. 3rd ed.; Wiley-Interscience: Hoboken, NJ, 2007.

15. Schlaf, R. Calibration of Photoemission Spectra and Work Function Determination. http://rsl.eng.usf.edu/Documents/Tutorials/PEScalibration.pdf (accessed October 30, 2016).

16. *Surface Analysis Methods in Materials Science*. 2nd ed.; O'Connor, D. J.; Sexton, B. A.; Smart, R. S. C., Eds.; Springer-Verlag: Berlin, 2003.

17. Skoog, R. A.; Holler, F. J.; Crouch, S. R., *Principles of Instrumental Analysis*. 6th ed.; Thomson Brooks/Cole: Belmont, CA, 2007.

18. Giordano, A. J. "Altering the Work Function of Surfaces: The Influential Role of Surface Modifiers for Tuning Properties of Metals and Transparent Conducting Oxides." Ph.D. Dissertation, Georgia Institute of Technology, 2014.

19. Hansen, W. N.; Hansen, G. J. "Standard reference surfaces for work function measurements in air." *Surf. Sci.* **2001,** *481*, 172-184.

20. Schlaf, R. Tutorial on Kelvin Probe Measurements. http://rsl.eng.usf.edu/Documents/Tutorials/TutorialsKelvinProbe.pdf (accessed October 11, 2016).

21. Heimel, G.; Romaner, L.; Zojer, E.; Brédas, J.-L. "Toward Control of the Metal-Organic Interfacial Electronic Structure in Molecular Electronics: A First-Principles Study on Self-Assembled Monolayers of Pi-Conjugated Molecules on Noble Metals." *Nano Lett.* **2007,** *7* (4), 932-940.

22. Heimel, G.; Romaner, L.; Zojer, E.; Brédas, J.-L. "The Interface Energetics of Self-Assembled Monolayers on Metals." *Acc. Chem. Res.* **2008,** *41* (6), 721-729.

23. Li, H.; Duan, Y.; Paramonov, P. B.; Coropceanu, V.; Brédas, J.-L. "Electronic structure of self-assembled (fluoro)methylthiol monolayers on the Au(111) surface: Impact of fluorination and coverage density." *J. Electron Spectrosc. Relat. Phenom.* **2009,** *174*, 70-77.

24. Li, H.; Paramonov, P. B.; Brédas, J.-L. "Theoretical study of the surface modification of indium tin oxide with trifluorophenyl phosphonic acid molecules: impact of coverage density and binding geometry." *J. Mater. Chem.* **2010,** *20*, 2630-2637.

25. Wood, C.; Li, H.; Winget, P.; Brédas, J.-L. "Binding Modes of Fluorinated Benzylphosphonic Acids on the Polar ZnO Surface and Impact on Work Function." *J. Phys. Chem. C* **2012,** *116*, 19125-19133.

26. Zhou, Y.; Fuentes-Hernandez, C.; Shim, J.; Meyer, J.; Giordano, A. J.; Li, H.; Winget, P.; Papadopoulos, T.; Cheun, H.; Kim, J.; Fenoll, M.; Dindar, A.; Haske, W.; Najafabadi, E.; Khan, T. M.; Sojoudi, H.; Barlow, S.; Graham, S.; Brédas, J.-L.; Marder, S. R.; Kahn, A.; Kippelen, B. "A Universal Method to Produce Low-Work Function Electrodes for Organic Electronics." *Science* **2012,** *336*, 327-332.

27. Helander, M. G.; Wang, Z. B.; Qiu, J.; Greiner, M. T.; Puzzo, D. P.; Liu, Z. W.; Lu, Z. H. "Chlorinated Indium Tin Oxide Electrodes with High Work Function for Organic Device Compatibility." *Science* **2011,** *332*, 944-947.

28. Wu, C. C.; Wu, C. I.; Sturm, J. C.; Kahn, A. "Surface modification of indium tin oxide by plasma treatment: An effective method to improve the efficiency, brightness, and reliability of organic light emitting devices." *Appl. Phys. Lett.* **1997,** *70* (11), 1348-1350.

29. Love, J. C.; Estroff, L. A.; Kriebel, J. K.; Nuzzo, R. G.; Whitesides, G. M. "Self-Assembled Monolayers of Thiolates on Metals as a Form of Nanotechnology." *Chem. Rev.* **2005,** *105*, 1103-1169.

30. Hotchkiss, P. J.; Li, H.; Paramonov, P. B.; Paniagua, S. A.; Jones, S. C.; Armstrong, N. R.; Brédas, J.-L.; Marder, S. R. "Modification of the Surface Properties of Indium Tin Oxide with Benzylphosphonic Acids: A Joint Experimental and Theoretical Study." *Adv. Mater.* **2009,** *21*, 4496-4501.

31. Li, H.; Winget, P.; Brédas, J.-L. "Surface Modification of Indium-Tin-Oxide Via Self-Assembly of a Donor-Acceptor Complex: A Density Functional Theory Study." *Adv. Mater.* **2012,** *24*, 687-693.

32. Paniagua, S. A.; Hotchkiss, P. J.; Jones, S. C.; Marder, S. R.; Mudalige, A.; Marrikar, F. S.; Pemberton, J. E.; Armstrong, N. R. "Phosphonic Acid Modification of Indium-Tin Oxide Electrodes: Combined XPS/UPS/Contact Angle Studies." *J. Phys. Chem. C* **2008,** *112*, 7809-7817.

33. Sharma, A.; Haldi, A.; Potscavage Jr., W. J.; Hotchkiss, P. J.; Marder, S. R.; Kippelen, B. "Effects of surface modification of indium tin oxide electrodes on the performance of molecular multilayer organic photovoltaic devices." *J. Mater. Chem.* **2009,** *19*, 5298-5302.

34. Sharma, A.; Hotchkiss, P. J.; Marder, S. R.; Kippelen, B. "Tailoring the work function of indium tin oxide electrodes in electrophosphorescent organic light-emitting diodes." *J. Appl. Phys.* **2009,** *105*, 084507(1-6).

35. Sharma, A.; Haldi, A.; Hotchkiss, P. J.; Marder, S. R.; Kippelen, B. "Effect of phosphonic acid surface modifiers on the work function of indium tin oxide and on the charge injection barrier into organic single-layer diodes." *J. Appl. Phys.* **2009,** *105*, 074511(1-6).

36. Sharma, A.; Kippelen, B.; Hotchkiss, P. J.; Marder, S. R. "Stabilization of the work function of indium tin oxide using organic surface modifiers in organic light-emitting diodes." *Appl. Phys. Lett.* **2008,** *93*, 163308(1-3).

37. Jiang, Y.; Oh, N.; Shim, M. "Double-Heterojunction Nanorod Light-Emitting Diodes with High Efficiencies at High Brightness Using Self-Assembled Monolayers." *ACS Photonics* **2016**.

38. Kajii, H.; Sato, Y.; Morimune, T.; Ohmori, Y. "Improved Sensitivity and Durability of Poly(3-Hexylthiophene)-Based Polymeric Photodetectors Using Indium Tin Oxide Modified by Phosphonic Acid–Based Self-Assembled Monolayer Treatment." *Electron. Comm. Jpn.* **2016,** *99* (7), 48-54.

39. Paniagua, S. A.; Giordano, A. J.; Smith, O. N. L.; Barlow, S.; Li, H.; Armstrong, N. R.; Pemberton, J. E.; Brédas, J.-L.; Ginger, D.; Marder, S. R. "Phosphonic Acids for Interfacial Engineering of Transparent Conductive Oxides." *Chem. Rev.* **2016,** *116* (12), 7117-7158.

40. Li, H.; Ratcliff, E. L.; Sigdel, A. K.; Giordano, A. J.; Marder, S. R.; Berry, J. J.; Brédas, J.-L. "Modification of the Gallium-Doped Zinc Oxide Surface with Self-Assembled Monolayers of Phosphonic Acids:A Joint Theoretical and Experimental Study." *Adv. Funct. Mater.* **2014,** *24*, 3593-3603.

41. Koch, N.; Duhm, S.; Rabe, J. P.; Vollmer, A.; Johnson, R. L. "Optimized Hole Injection with Strong Electron Acceptors at Organic-Metal Interfaces." *Phys. Rev. Lett.* **2005,** *95* (23), 237601(1-4).

42. Duhm, S.; Glowatzki, H.; Rabe, J. P.; Koch, N.; Johnson, R. L. "Spontaneous charge transfer at organic-organic homointerfaces to establish thermodynamic equilibrium." *Appl. Phys. Lett.* **2007,** *90* (12), 122113 (1-3).

43. Romaner, L.; Heimel, G.; Brédas, J.-L.; Gerlach, A.; Schreiber, F.; Johnson, R. L.; Zegenhagen, J.; Duhm, S.; Koch, N.; Zojer, E. "Impact of Bidirectional Charge Transfer and Molecular Distortions on the Electronic Structure of a Metal-Organic Interface." *Phys. Rev. Lett.* **2007,** *99* (25), 256801(1-4).

44. Rangger, G. M.; Hofmann, O. T.; Romaner, L.; Heimel, G.; Bröker, B.; Blum, R.-P.; Johnson, R. L.; Koch, N.; Zojer, E. "F4TCNQ on Cu, Ag, and Au as prototypical example for a strong organic acceptor on coinage metals." *Phys. Rev. B* **2009,** *79*, 165306 (1-12).

45. Duhm, S.; Glowatzki, H.; Cimpeanu, V.; Klankermayer, J.; Rabe, J. P.; Johnson, R. L.; Koch, N. "Weak Charge Transfer between Acceptor Molecule and Metal Surfaces Enabling Organic/Metal Energy Level Tuning." *J. Phys. Chem. B* **2006,** *110* (42), 21069-21072.

46. Habraken, F. H. P. M.; Bootsma, G. A.; Hofmann, P.; Hahicha, S.; Bradshaw, A. M. "The Adsorption and Incorporation of Oxygen on Cu(110) and its Reaction with Carbon Monoxide." *Surf. Sci.* **1979,** *88* (2-3), 285-298.

47. Hinckley, A. C.; Wang, C.; Pfattner, R.; Kong, D.; Zhou, Y.; Ecker, B.; Gao, Y.; Bao, Z. "Investigation of a Solution-Processable, Nonspecific Surface Modifier for Low Cost, High Work Function Electrodes." *ACS Appl. Mater. Interfaces* **2016,** *8*, 19658-19664.

48. Kim, J. S.; Granström, M.; Friend, R. H.; Johansson, N.; Salaneck, W. R.; Daik, R.; Feast, W. J.; Cacialli, F. "Indium-tin oxide treatments for single- and double-layer polymeric light-emitting diodes: The relation between the anode physical, chemical, and morphological properties and the device performance." *J. Appl. Phys.* **1998,** *84* (12), 6859-6870.

49. Sugiyama, K.; Ishii, H.; Ouchi, Y.; Seki, K. "Dependence of indium-tin-oxide work function on surface cleaning method as studied by ultraviolet and x-ray photoemission spectroscopies." *J. Appl. Phys.* **2000,** *87* (1), 295-298.

50. You, J. B.; Zhang, X. W.; Cai, P. F.; Dong, J. J.; Gao, Y.; Yin, Z. G.; Chen, N. F.; Wang, R. Z.; Yan, H. "Enhancement of field emission of the ZnO film by the reduced work function and the increased conductivity via hydrogen plasma treatment." *Appl. Phys. Lett.* **2009,** *94* (26), 262105 (1-3).

51. Schulz, P.; Schäfer, T.; Zangmeister, C. D.; Effertz, C.; Meyer, D.; Mokros, D.; van Zee, R. D.; Mazzarello, R.; Wuttig, M. "A New Route to Low Resistance Contacts for Performance-Enhanced Organic Electronic Devices." *Adv. Mater. Interfaces* **2014,** *1* (5), 1300130 (1-8).

52. Ford, W. E.; Gao, D.; Knorr, N.; Wirtz, R.; Scholz, F.; Karipidou, Z.; Ogasawara, K.; Rosselli, S.; Rodin, V.; Nelles, G.; von Wrochem, F. "Organic Dipole Layers for Ultralow Work Function Electrodes." *ACS Nano* **2014,** *8* (9), 9173-9180.

53. Meyer, D.; Schäfer, T.; Schulz, P.; Jung, S.; Rittich, J.; Mokros, D.; Segger, I.; Maercks, F.; Effertz, C.; Mazzarello, R.; Wuttig, M. "Dithiocarbamate Self-Assembled Monolayers as Efficient Surface Modifiers for Low Work Function Noble Metals." *Langmuir* **2016,** *32*, 8812-8817.

54. Kim, J.; Rim, Y. S.; Liu, Y.; Serino, A. C.; Thomas, J. C.; Chen, H.; Yang, Y.; Weiss, P. S. "Interface Control in Organic Electronics Using Mixed Monolayers of Carboranethiol Isomers." *Nano Lett.* **2014,** *14*, 2946-2951.

55. Nuzzo, R. G.; Allara, D. L. "Adsorption of Bifunctional Organic Disulfides on Gold Surfaces." *J. Am. Chem. Soc.* **1983,** *105* (13), 4481-4483.

56. de Boer, B.; Hadipour, A.; Mandoc, M. M.; van Woudenbergh, T.; Blom, P. W. M. "Tuning of Metal Work Functions with Self-Assembled Monolayers." *Adv. Mater.* **2005,** *17* (5), 621-625.

57. Alloway, D. M.; Hofmann, M.; Smith, D. L.; Gruhn, N. E.; Graham, A. L.; Colorado, J., Ramon; ; Wysocki, V. H.; Lee, T. R.; Lee, P. A.; Armstrong, N. R. "Interface Dipoles Arising from Self-Assembled Monolayers on Gold: UV-Photoemission Studies of Alkanethiols and Partialy Fluorinated Alkanethiols." *J. Phys. Chem. B* **2003,** *107*, 11690-11699.

58. Narasimha, K. T.; Ge, C.; Fabbri, J. D.; Clay, W.; Tkachenko, B. A.; Fokin, A. A.; Schreiner, P. R.; Dahl, J. E.; Carlson, R. M. K.; Shen, Z. X.; Melosh, N. A. "Ultralow effective work function surfaces using diamondoid monolayers." *Nat. Nanotechnol.* **2016,** *11* (3), 267-272.

59. Deng, X.; Nie, R.; Li, A.; Wei, H.; Zheng, S.; Huang, W.; Mo, Y.; Su, Y.; Wang, Q.; Li, Y.; Tang, J.; Xu, J.; Wong, K.-y. "Ultra-Low Work Function Transparent Electrodes Achieved by Naturally Occurring Biomaterials for Organic Optoelectronic Devices." *Adv. Mater. Interfaces* **2014,** *1*, 1400215 (1-6).

60. Liu, Y.; Aghdassi, N.; Wang, Q.; Duhm, S.; Zhou, Y.; Song, B. "Solvent-resistant ITO work function tuning by an acridine derivative enables high performance inverted polymer solar cells." *Org. Electron.* **2016,** *35*, 6-11.

61. Osikowicz, W.; Crispin, X.; Tengstedt, C.; Lindell, L.; Kugler, T.; Salaneck, W. R. "Transparent low-work function indium tin oxide electrode obtained by molecular scale interface engineering." *Appl. Phys. Lett.* **2004,** *85*, 1616-1618.

62. Lindell, L.; Unge, M.; Osikowicz, W.; Stafström, S.; Salaneck, W. R.; Crispin, X.; de Jong, M. P. "Integer charge transfer at the tetrakis(dimethylamino)ethylene/Au interface." *Appl. Phys. Lett.* **2008,** *92*, 163302(1-3).

63. Bröker, B.; Blum, R.-P.; Frisch, J.; Vollmer, A.; Hofmann, O. T.; Rieger, R.; Müllen, K.; Rabe, J. P.; Zojer, E.; Koch, N. "Gold work function reduction by 2.2 eV with an air-stable molecular donor layer " *Appl. Phys. Lett.* **2008,** *93*, 243303(1-3).

64. Hofmann, O. T.; Rangger, G. M.; Zojer, E. "Reducing the Metal Work Function beyond Pauli Pushback: A Computational Investigation of Tetrathiafulvalene and Viologen on Coinage Metal Surfaces." *J. Phys. Chem. C* **2008,** *112* (51), 20357-20365.

65. Bröker, B.; Blum, R.-P.; Beverina, L.; Hofmann, O. T.; Sassi, M.; Ruffo, R.; Pagani, G. A.; Heimel, G.; Vollmer, A.; Frisch, J.; Rabe, J. P.; Zojer, E.; Koch, N. "A High Molecular Weight Donor for Electron Injection Interlayers on Metal Electrodes." *ChemPhysChem* **2009,** *10* (17), 2947-2954.

66. Li, F.; Zhou, Y.; Zhang, F.; Liu, X.; Zhan, Y.; Fahlman, M. "Tuning Work Function of Noble Metals As Promising Cathodes in Organic Electronic Devices." *Chem. Mater.* **2009,** *21*, 2798-2802.

67. Guo, S.; Kim, S. B.; Mohapatra, S. K.; Qi, Y.; Sajoto, T.; Kahn, A.; Marder, S. R.; Barlow, S. "n-Doping of Organic Electronic Materials Using Air-Stable Organometallics." *Adv. Mater.* **2012,** *24*, 699-703.

68. Guo, S.; Mohapatra, S. K.; Romanov, A.; Timofeeva, T. V.; Hardcastle, K. I.; Yesudas, K.; Risko, C.; Brédas, J.-L.; Marder, S. R.; Barlow, S. "n-Doping of Organic Electronic Materials Using Air-Stable Organometallics: A Mechanistic Study of Reduction by Dimeric Sandwich Compounds." *Chem. - Eur. J.* **2012,** *18* (46), 14760-14772.

69. Mohapatra, S. K.; Fonari, A.; Risko, C.; Yesudas, K.; Moudgil, K.; Delcamp, J. H.; Timofeeva, T. V.; Brédas, J.-L.; Marder, S. R.; Barlow, S. "Dimers of Nineteen-Electron Sandwich Compounds: Crystal and Electronic Structures, and Comparison of Reducing Strengths." *Chem. - Eur. J.* **2014,** *20*, 15385-15394.

70. Paniagua, S. A.; Baltazar, J.; Sojoudi, H.; Mohapatra, S. K.; Zhang, S.; Henderson, C. L.; Graham, S.; Barlow, S.; Marder, S. R. "Production of heavily n- and p-doped CVD graphene with solution-processed redox-active metal–organic species." *Mater. Horiz.* **2014,** *1*, 111-115.

71. Giordano, A. J.; Pulvirenti, F.; Khan, T. M.; Fuentes-Hernandez, C.; Moudgil, K.; Delcamp, J. H.; Kippelen, B.; Barlow, S.; Marder, S. R. "Organometallic Dimers: Application to Work Function Reduction of Conducting Oxides." *ACS Appl. Mater. Interfaces* **2015,** *7* (7), 4320-4326.

72. Schlesinger, R.; Bianchi, F.; Blumstengel, S.; Christodoulou, C.; Ovsyannikov, R.; Kobin, B.; Moudgil, K.; Barlow, S.; Hecht, S.; Marder, S. R.; Henneberger, F.; Koch, N. "Efficient light emission from inorganic/organic semiconductor hybrid structures by energy level tuning." *Nat. Commun.* **2015,** *6*, 6754 (1-7).

73. Zhang, S.; Naab, B. D.; Jucov, E. V.; Parkin, S.; Evans, E. G. B.; Millhauser, G. L.; Timofeeva, T. V.; Risko, C.; Brédas, J.-L.; Bao, Z.; Barlow, S.; Marder, S. R. "n-Dopants Based on Dimers of Benzimidazoline Radicals: Structures and Mechanism of Redox Reactions." *Chem. - Eur. J.* **2015,** *21* (30), 10878-10885.

74. Akaike, K.; Nardi, M. V.; Oehzelt, M.; Frisch, J.; Opitz, A.; Christodoulou, C.; Ligorio, G.; Beyer, P.; Timpel, M.; Pis, I.; Bondino, F.; Moudgil, K.; Barlow, S.; Marder, S. R.; Koch, N. "Effective Work Function Reduction of Practical Electrodes Using an Organometallic Dimer." *Adv. Funct. Mater.* **2016,** *26* (15), 2493-2502.

75. Azum, N.; Taib, L. A.; Al Angari, Y. M.; Asiri, A. M.; Denti, M.; Usta, H.; Facchetti, A. "π-Conjugated donor-acceptor small molecule thin-films on gold electrodes for reducing the metal work-function." *Thin Solid Films* **2016,** *616*, 320-327.

76. Chang, C.-Y.; Huang, W.-K.; Chang, Y.-C. "Highly-Efficient and Long-Term Stable Perovskite Solar Cells Enabled by a Cross-Linkable n-Doped Hybrid Cathode Interfacial Layer." *Chem. Mater.* **2016,** *28* (17), 6305-6312.

77. Cui, C.; Li, Y.; Li, Y. "Fullerene Derivatives for the Applications as Acceptor and Cathode Buffer Layer Materials for Organic and Perovskite Solar Cells." *Adv. Energy Mater.* **2016**.

78. Adhikari, B.; Meng, S.; Fyta, M. "Carbene-mediated self-assembly of diamondoids on metal surfaces." *Nanoscale* **2016,** *8* (16), 8966-8975.

79. Paniagua, S. A.; Li, E. L.; Marder, S. R. "Adsorption studies of a phosphonic acid on ITO: film coverage, purity, and induced electronic structure changes." *Phys. Chem. Chem. Phys.* **2014,** *16* (7), 2874-2881.

80. Köhler, L.; Kresse, G. "Density functional study of CO on Rh(111)." *Phys. Rev. B* **2004,** *70*, 165405(1-9).

81. NEXAFS Spectroscopy. http://ssrl.slac.stanford.edu/stohr/nexafs.htm (accessed October 11, 2016).

82. Gliboff, M.; Li, H.; Knesting, K. M.; Giordano, A. J.; Nordlund, D.; Seidler, G. T.; Brédas, J.-L.; Marder, S. R.; Ginger, D. S. "Competing Effects of Fluorination on the Orientation of Aromatic and Aliphatic Phosphonic Acid Monolayers on Indium Tin Oxide." *J. Phys. Chem. C* **2013,** *117* (29), 15139-15147.

83. Gliboff, M.; Sang, L.; Knesting, K. M.; Schalnat, M. C.; Mudalige, A.; Ratcliff, E. L.; Li, H.; Sigdel, A. K.; Giordano, A. J.; Berry, J. J.; Nordlund, D.; Seidler, G. T.; Brédas, J.-L.; Marder, S. R.; Pemberton, J. E.; Ginger, D. S. "Orientation of Phenylphosphonic Acid Self-Assembled Monolayers on a Transparent Conductive Oxide: A Combined NEXAFS, PM-IRRAS, and DFT Study." *Langmuir* **2013,** *29*, 2166-2174.

84. Gliboff, M. "Molecular Level Understanding of Interfaces and Excited State Electronic Structure in Organic Solar Cells Using Soft X-ray Techniques." Ph.D. Dissertation, University of Washington, 2013.

CHAPTER 2

COMPUTATIONAL METHODOLOGY

In this Chapter, the quantum mechanical methods utilized in the determination of the work function of a surface are reviewed. We begin with the Schrödinger equation and then move to some of the approximate methods (i.e. Hartree-Fock Theory and Density Functional Theory) that are currently employed in electronic structure theory. Differences in the methodology for calculations on isolated molecules and periodic systems will be discussed. Molecular dynamics methods will also be described, with a particular emphasis on ab initio molecular dynamics.

2.1 Electronic-Structure Theories

2.1.1 Schrödinger Equation

The main equation in the field of electronic-structure theory is the time-independent, non-relativistic Schrödinger equation, shown in Equation 2.1,[1] which is widely used in the case of organic systems:

$$\hat{\mathcal{H}}\,|\Psi_i\rangle = \mathrm{E_i}\,|\Psi_i\rangle \tag{2.1}$$

Here, $\hat{\mathcal{H}}$ represents the Hamiltonian operator, $|\Psi_i\rangle$ represents the molecular wave function, and E_i represents the energy of the corresponding wave function. The Hamiltonian operator, in atomic units, for N electrons and M nuclei is defined as:

$$\hat{\mathcal{H}} = \underbrace{-\sum_{i=1}^{N}\frac{1}{2}\nabla_i^2}_{1} \underbrace{-\sum_{A=1}^{M}\frac{1}{2\,M_A}\nabla_A^2}_{2} \underbrace{-\sum_{i=1}^{N}\sum_{A=1}^{M}\frac{Z_A}{r_{iA}}}_{3} + \underbrace{\sum_{i=1}^{N}\sum_{j>i}^{N}\frac{1}{r_{ij}}}_{4} + \underbrace{\sum_{A=1}^{M}\sum_{B>A}^{M}\frac{Z_A Z_B}{R_{AB}}}_{5} \qquad (2.2)$$

where ∇_i^2 and ∇_A^2 are Laplacian operators that involve differentiation with respect to the coordinates of the *i*th electron and the *A*th nucleus, M_A is the ratio of the mass of the *A*th nucleus to the mass of an electron, Z_A is the atomic number of nucleus *A*, $r_{ij} = |\mathbf{r}_i - \mathbf{r}_j|$ is the distance between the *i*th and *j*th electrons, $r_{iA} = |\mathbf{r}_i - \mathbf{R}_A|$ is the distance between the *i*th electron and the *A*th nucleus, and $R_{AB} = |\mathbf{R}_A - \mathbf{R}_B|$ is the distance between the *A*th and *B*th nuclei. The first term in the Hamiltonian operator represents the electronic kinetic energy, while the second term represents the nuclear kinetic energy. The third term represents the Coulomb attraction between the electrons and the nuclei, while the fourth and fifth terms represent the repulsion among electrons and nuclei, respectively.

The Schrödinger equation cannot be solved exactly, except for simple, hydrogen-like systems. In order to solve this equation for more complex systems, different approximations are made. The first approximation, which was mentioned above in describing Equation 2.1, is the neglect of relativistic effects. These effects increase like Z^2 and tend to affect the d- and f-orbitals more than s- and p-orbitals. The s- and p-orbitals, which are the most common orbitals for atoms that compose organic molecules, will tend to contract due to the increased mass of the electron at speeds close to the speed of light $\left(m = \frac{m_0}{\sqrt{1-(v/c)}}\right)$ and will thus become more energetically stabilized. The electrons in the d- and f-orbitals, which have low probabilities of being near the nucleus, will be screened more by the contracted s- and p-orbitals, thus causing the orbitals to expand radially and increase in energy.[2]

The second approximation is known as the Born-Oppenheimer approximation. This arises from the difference in mass of the electrons and the nuclei. The electron, which is roughly 2000 times lighter than a proton or neutron, ($9.10938356(11)\times10^{-31}$ kg, $1.672621898(21)\times10^{-27}$ kg, and $1.674927471(21)\times10^{-27}$ kg for the electron, proton, and neutron, respectively) moves much more quickly than the nucleus; thus it can be considered that the electrons move in a field of fixed nuclei. This approximation allows the kinetic energy of the nuclei, the second term in Equation 2.1, to be neglected and the repulsion of the nuclei, the fifth term in Equation 2.1, to correspond to a constant. The remaining terms in Equation 2.1 are thus denoted as the electronic Hamiltonian, $\widehat{\mathcal{H}}_{elec}$, describing the motion of N electrons in a field of M point charges:

$$\widehat{\mathcal{H}}_{\mathrm{elec}} = -\sum_{\mathrm{i=1}}^{\mathrm{N}} \frac{1}{2}\nabla_{\mathrm{i}}^{2} - \sum_{\mathrm{i=1}}^{\mathrm{N}}\sum_{\mathrm{A=1}}^{\mathrm{M}} \frac{\mathrm{Z_A}}{\mathrm{r_{iA}}} + \sum_{\mathrm{i=1}}^{\mathrm{N}}\sum_{\mathrm{j>i}}^{\mathrm{N}} \frac{1}{\mathrm{r_{ij}}} \tag{2.3}$$

Equation 2.3 leads to the electronic Schrödinger equation:

$$\widehat{\mathcal{H}}_{\mathrm{elec}}\Psi_{\mathrm{elec}} = \mathrm{E_{elec}}\Psi_{\mathrm{elec}} \tag{2.4}$$

where the electronic wave function, Ψ_{elec}, depends on the coordinates of the electrons for a given configuration of nuclei. The total energy, E_{tot}, is then a sum of the electronic energy, E_{elec}, and the nuclear energy, E_{nuc}:

$$\mathrm{E_{tot}} = \mathrm{E_{elec}} - \sum_{\mathrm{A=1}}^{\mathrm{M}} \frac{1}{2\,\mathrm{M_A}}\nabla_{\mathrm{A}}^{2} + \sum_{\mathrm{A=1}}^{\mathrm{M}}\sum_{\mathrm{B>A}}^{\mathrm{M}} \frac{\mathrm{Z_A Z_B}}{\mathrm{R_{AB}}} = \mathrm{E_{elec}} + \mathrm{E_{nuc}} \tag{2.5}$$

The electronic Hamiltonian depends on the spatial and spin coordinates of the electrons (where $\mathbf{x}_i$ denotes the spatial and spin coordinates of electron i) , and the many-electron wave function must be anti-symmetric with respect to the interchange of any two electrons, in order to obey the Pauli exclusion (anti-symmetry) principle:

$$\Psi(\mathbf{x}_1, \ldots, \mathbf{x}_i, \mathbf{x}_j, \ldots, \mathbf{x}_N) = -\Psi(\mathbf{x}_1, \ldots, \mathbf{x}_j, \mathbf{x}_i, \ldots, \mathbf{x}_N) \tag{2.6}$$

Even though Equation 2.3 only depends on the electronic motions in a field of point charges, the electronic Schrödinger equation still remains difficult to solve. In order to increase the tractability, another approximation was made early on, the independent-particle approximation, which transforms the electronic Schrödinger equation from solving an N-electron Hamiltonian into N one-electron Hamiltonians. The wave function then becomes a product of spin orbital wave functions for each electron, known as the Hartree product:

$$\Psi^{\mathrm{HP}}(\mathbf{x}_1, \mathbf{x}_2, \ldots, \mathbf{x}_N) = \chi_i(\mathbf{x}_1)\chi_j(\mathbf{x}_2)\cdots\chi_k(\mathbf{x}_N) \tag{2.7}$$

where spin orbitals are defined as multiplying the spatial orbital (Ψ) by the spin function (either α(ω) or β(ω) for spin up and spin down, respectively):

$$\chi(\mathbf{x}) = \begin{cases} \psi(\mathbf{r})\alpha(\omega) \\ \text{or} \\ \psi(\mathbf{r})\beta(\omega) \end{cases} \tag{2.8}$$

Since the Hartree product does not guarantee that the anti-symmetry principle will be satisfied, the many-electron wave function may be presented as a single Slater determinant:

$$\Psi(\mathbf{x}_1, \mathbf{x}_2, \ldots, \mathbf{x}_N) = \frac{1}{\sqrt{N!}} \begin{vmatrix} \chi_i(\mathbf{x}_1) & \chi_j(\mathbf{x}_1) & \cdots & \chi_k(\mathbf{x}_1) \\ \chi_i(\mathbf{x}_2) & \chi_j(\mathbf{x}_2) & \cdots & \chi_k(\mathbf{x}_2) \\ \vdots & \vdots & \ddots & \vdots \\ \chi_i(\mathbf{x}_N) & \chi_j(\mathbf{x}_N) & \cdots & \chi_k(\mathbf{x}_N) \end{vmatrix} \tag{2.9}$$

where $\frac{1}{\sqrt{N!}}$ is a normalization factor and $\chi(\mathbf{x})$ are the one electron spin orbitals. By using a Slater determinant, the interchange of any two electrons, which corresponds to switching any two rows, guarantees that the wave functions will have opposite signs, thus the anti-symmetry principle is once again satisfied. Additionally, if there are two electrons in the

same spin orbital, corresponding to any two columns being equal, the determinant and corresponding wave function is zero.

In this Thesis, additional electronic-structure theories will be employed in order to model molecular systems. These include Hartree-Fock theory and Density Functional Theory, which will be briefly discussed in the following sections.

2.1.2 Hartree-Fock Theory

Even with the simplified electronic Hamiltonian (Equation 2.3), quantum chemists have to handle many-electron problems, except for the very simple cases, like H_2^+. In order to make these systems easier to solve, the Hartree-Fock approximation is made, which essentially replaces the complicated many-electron problem by a series of one-electron problems in which the electron-electron repulsion is treated in an average way. This arises from a single Slater determinant, which is the simplest anti-symmetric wave function describing the ground state of an N-electron system:

$$|\Psi_0\rangle = |\chi_1\chi_2 \cdots \chi_i\chi_j \ldots \chi_N\rangle \tag{2.10}$$

The variational principle states that best wave function will minimize the energy of the N-electron system:

$$E_0 = \langle\Psi_0|\hat{\mathcal{H}}_{elec}|\Psi_0\rangle \tag{2.11}$$

The variations can be made with the choice of spin-orbitals, χ. By minimizing E_0 with respect to the spin orbitals, the Hartree-Fock equation can be obtained, which determines the optimal spin orbitals:

$$f(i)\chi(\mathbf{x}_i) = E_{HF}\chi(\mathbf{x}_i) \tag{2.12}$$

where $f(i)$ is an effective one-electron operator, called the Fock operator, of the form:

$$f(i) = -\frac{1}{2}\nabla_i^2 - \sum_{A=1}^{M}\frac{Z_A}{r_{iA}} + v^{HF}(i) \tag{2.13}$$

and the Hartree-Fock energy is:

$$E_{HF} = \sum_{i}^{N}\langle i|h|i\rangle + \frac{1}{2}\sum_{ij}^{N}[ii|jj] - [ij|ji] \tag{2.14}$$

where:

$$\langle i|\hat{h}|i\rangle = \int d\mathbf{x}_1 \chi_i^*(\mathbf{x}_1)\left\{-\frac{1}{2}\nabla_i^2 - \sum_{A}^{M}\frac{Z_A}{r_{iA}}\right\}\chi_i(\mathbf{x}_1) \tag{2.15}$$

$$[ii|jj] = \int d\mathbf{x}_1 d\mathbf{x}_2 \chi_i^*(\mathbf{x}_1)\chi_i(\mathbf{x}_1)\frac{1}{r_{12}}\chi_j^*(\mathbf{x}_2)\chi_j(\mathbf{x}_2) \tag{2.16}$$

$$[ij|ji] = \int d\mathbf{x}_1 d\mathbf{x}_2 \chi_i^*(\mathbf{x}_1)\chi_j(\mathbf{x}_1)\frac{1}{r_{12}}\chi_j^*(\mathbf{x}_2)\chi_i(\mathbf{x}_2) \tag{2.17}$$

Equation 2.15 corresponds to the one-electron contribution to the kinetic energy and the electro-nuclear attraction. Equations 2.16 and 2.17 correspond to the two-electron Coulomb and exchange integrals, respectively. The Hartree-Fock potential, $v^{HF}(i)$, which is the "field" seen by the *i*th electron, depends on the spin orbitals of the other electrons. This dependence on the spin orbitals of other electrons makes the Hartree-Fock equation non-linear and it must be solved iteratively. The iterative procedure for solving the Hartree-Fock equation is known as the self-consistent field (SCF) method. This method starts with an initial guess of the spin orbitals, which allows for the calculation of the average field seen by each electron (v^{HF}), which is then used to solve Equation 2.12 for a new set of spin orbitals. The new spin orbitals go through the same procedure, producing fields and spin orbitals, until self-consistency is reached (i.e. until the fields no longer change and the spin orbitals used to create the Fock operator are the same as the orbitals from the previous

iteration). A further approximation is that the spin orbitals are typically defined as linear combinations of atomic orbitals in order to form molecular orbitals:

$$\chi_i = \sum_{\mu} C_{\mu}^{i} \phi_{\mu} \tag{2.18}$$

where C_{μ}^{i} are the expansion coefficients and ϕ_{μ} are the atomic orbitals constructed from Gaussian-type orbitals (GTO):

$$\phi_{\mu}^{GTO}(r) = N x^{l} y^{m} z^{n} e^{-\zeta r^2} \tag{2.19}$$

where N is a normalization constant, *l*, *m*, and *n* are integers used to describe the angular momentum of the orbitals, and ζ controls the diffusiveness of the orbital.

2.1.3 Density Functional Theory

Density functional theory (DFT) attempts to solve the electronic Schrödinger equation using the electronic density rather than the wave function. This was made possible by the seminal work of Hohenberg and Kohn[3], who related the ground-state energy to the ground-state electron density.

2.1.3.1 The Hohenberg-Kohn Theorems

The Hohenberg-Kohn theorems are the basis of density functional theory. They were developed in 1964 for a model of a homogeneous electron gas, with a non-degenerate ground state, under the influence of a given external potential, but they can be generalized to apply to any system of electrons moving under an external potential. The Hamiltonian of this system has the form:

$$\hat{H} = \hat{F} + \hat{V}_{ext} \tag{2.20}$$

where the external potential operator, $\hat{V}_{ext}$, is the Coulomb attraction between the nuclei and the electrons and the electron-only portions of the electronic Hamiltonian are defined as a new operator, $\hat{F}$:

$$\hat{\mathrm{V}}_{\mathrm{ext}} = -\sum_{\mathrm{i}=1}^{\mathrm{N}}\sum_{\mathrm{A}=1}^{\mathrm{M}}\frac{\mathrm{Z_A}}{\mathrm{r_{iA}}} \tag{2.21}$$

$$\hat{\mathrm{F}} = -\frac{1}{2}\sum_{\mathrm{i}=1}^{\mathrm{N}}\nabla_{\mathrm{i}}^{2} + \frac{1}{2}\sum_{\mathrm{i}=1}^{\mathrm{N}}\sum_{\mathrm{j}>\mathrm{i}}^{\mathrm{N}}\frac{1}{\mathrm{r_{ij}}} \tag{2.22}$$

Since $\hat{F}$ is the same for all N-electron systems, the Hamiltonian and thus the ground state wave function, $|\Psi_0\rangle$, are completely determined by the number of electrons, N, and the external potential, V_{ext}. The ground state electron density, ρ_0, can be obtained from $|\Psi_0\rangle$, making both functionals of N and V_{ext}. The electron density is defined as:

$$\rho[\mathbf{r}] = \mathrm{N}\int \mathrm{d}^3\mathbf{r}_2 \ldots \int \mathrm{d}^3\mathbf{r}_{\mathrm{N}}|\Psi(\mathbf{r}_1, \mathbf{r}_2, \ldots, \mathbf{r}_{\mathrm{N}})|^2 \tag{2.23}$$

The first theorem states that the external potential is a unique functional of the electron density, apart from a constant. This means that knowing the electron density allows for the calculation of the external potential and all properties of the system can be determined. The second theorem defines an energy functional, which through the variational principle, is minimized by the exact ground state electron density. The energy may be defined as:

$$\begin{aligned}\mathrm{E}[\rho(\mathbf{r})] = \left\langle\Psi\middle|\hat{\mathrm{H}}\middle|\Psi\right\rangle &= \mathrm{F}[\rho] + \mathrm{V_{ext}}[\rho] = \mathrm{T}[\rho] + \mathrm{E_{ee}}[\rho] + \mathrm{E_{Ne}}[\rho] \\ &= \mathrm{T}[\rho] + \mathrm{J}[\rho] + \mathrm{E_{NCC}}[\rho] + \mathrm{E_{Ne}}[\rho]\end{aligned} \tag{2.24}$$

where the Hamiltonian is composed of a kinetic energy component, *T*, an electron-electron repulsion component, E_{ee} and a nuclear-electron attraction component, E_{Ne}. $F[\rho]$ is sometimes denoted in the literature as the universal functional. The electron-electron repulsion term can be represented by the Coulomb functional, *J*, and a non-classical

correlation functional, E_{NCC}, which incorporates the effects of self-interaction, exchange, and electron correlation.

2.1.3.2 Kohn-Sham Theory

In 1965, Kohn and Sham[4] set out to extend the Hohenberg-Kohn theorems to real systems where the electronic density is non-uniform. They introduced a formalism where a system of interacting electrons in an external potential is reduced to a system of *non-interacting* electrons in an effective potential. This reduced system can be represented by a set of Kohn-Sham (KS) orbitals, ϕ_i, that constitute a Slater determinant, representing the ground state wave function, for which the kinetic energy is known exactly:

$$\mathrm{T_s} = -\frac{1}{2}\sum_{\mathrm{i=1}}^{\mathrm{N}} \langle \phi_\mathrm{i} | \nabla^2 | \phi_\mathrm{i} \rangle \tag{2.25}$$

There is a small difference between the kinetic energies of the interacting electron system, T, and the non-interacting electron system, $\mathrm{T_s}$, but this is then accounted for by other functionals, namely the exchange-correlation functional. After the formalism is applied, the universal functional, $F[\rho]$, becomes:

$$\mathrm{F[\rho] = T_s[\rho] + J[\rho] + E_{XC}[\rho]} \tag{2.26}$$

where $\mathrm{E_{XC}[\rho]}$ is the exchange-correlation functional which contains the correction of the kinetic energy and the contribution of the non-classical electron correlation and exchange:

$$\mathrm{E_{XC}[\rho] = (T[\rho] - T_s[\rho]) + (E_{ee}[\rho] - J[\rho]) = T_C[\rho] + E_{NCC}[\rho]} \tag{2.27}$$

By separating the universal functional $F[\rho]$ into these three terms in Equation 2.26, the first two can be solved simply, while the third part, which contains the effects of complex

behaviors, becomes an even smaller portion of the total energy. Applying this updated version of the universal functional F[ρ] to Equation 2.24, the KS energy, E^{KS}, becomes:

$$E^{KS}[\rho] = T_s[\rho] + E_{Ne}[\rho] + J[\rho] + E_{XC}[\rho] \tag{2.28}$$

The Schrödinger equation becomes:

$$\left[-\frac{1}{2}\nabla^2 - \sum_{A=1}^{M}\frac{Z_A}{r_{iA}} + \int\frac{\rho(\mathbf{r}_2)}{r_{12}} + V_{XC}(\mathbf{r}_1)\right]\phi_i = E_i^{KS}\phi_i \tag{2.29}$$

where V_{XC} is the exchange-correlation functional derivative, which can be described as the one-electron operator for which the expectation value of the KS Slater determinant is E_{XC}:[5]

$$V_{XC} = \frac{\delta E_{XC}}{\delta\rho} \tag{2.30}$$

"For an arbitrary $n(\mathbf{r})$ [$\rho(\mathbf{r})$ in this Thesis], of course, one can give no simple exact expression for $E_{XC}[n]$." [4] This implies that approximations have to be made in order to solve the Schrödinger equation using KS orbitals.

2.1.3.3 Approximate Exchange-Correlation Functionals

Since the exact exchange-correlation functional is unknown, different approximations to the functional are used. Three of the most common approximations are the local density approximation (LDA), the generalized gradient approximation (GGA), and hybrid functionals. Each will be covered briefly in the following sections.

2.1.3.3.1 Local Density Approximation

The local density approximation (LDA) is the simplest and is the base upon which the other approximations are made. In this approximation, the exchange-correlation functional only depends on the local electron density:

$$E_{XC}^{LDA}[\rho] = \int \rho(\mathbf{r})\varepsilon_{XC}^{LDA}[\rho(\mathbf{r})]d\mathbf{r} \quad (2.31)$$

where ε_{XC}^{LDA} is the exchange-correlation energy per particle, also known as an "energy density",[5] and the electron density, ρ, is assumed to be slowly varying. The exchange-correlation functional, E_{XC}^{LDA}, can be separated into exchange, E_X^{LDA}, and correlation, E_C^{LDA}, such that:

$$E_{XC}^{LDA} = E_X^{LDA} + E_C^{LDA} \quad (2.32)$$

where the exchange, defined as:

$$E_X^{LDA}[\rho] = -\frac{3}{4}\left(\frac{3}{\pi}\right)^{1/3} \int \rho(\mathbf{r})^{4/3} d\mathbf{r} \quad (2.33)$$

and the correlation contribution is not known analytically, except at the limits of high and low density.[5] For intermediate densities, Ceperley and Alder[6] used quantum Monte Carlo simulations of uniform electron gases with varying densities to calculate the total energies of the systems. Then by subtracting the analytical exchange energy from the total energy, the correlation energy for each system could be determined. If the spin state is also accounted for in the calculation, the method is denoted as local spin density approximation (LSDA). L(S)DA is surprisingly good for describing atoms and molecules.[7] Popular L(S)DA exchange-correlation functionals include those developed by Vosko, Wilk, and Nusair (VWN),[8] Perdew and Zunger (PZ),[9] and Perdew and Wang (PW).[10]

L(S)DA functionals have difficulties in describing systems which have partially filled valence d- or f- electron shells. One way to better describe these systems is to use a method that combines the DFT-L(S)DA and the spin unrestricted Hartree-Fock (UHF) method, denoted as L(S)DA+U. This is sometimes denoted as L(S)DA with a characteristic Hubbard parameter U. The method of Dudarev *et al.*[11] has been used in some of the work

presented in this Thesis. The total energy in this method adds a term to the L(S)DA energies that involves two variables, $\bar{U}$ and $\bar{J}$, while only the difference $(\bar{U} - \bar{J})$ is important:

$$E_{L(S)DA+U} = E_{L(S)DA} + \frac{(\bar{U} - \bar{J})}{2} \sum_{\sigma} \left(n_{m,\sigma} - n_{m,\sigma}^2 \right) \tag{2.34}$$

where $n_{m,\sigma}$ is the occupation number of the *m*th d-state and the total number of electrons, N_σ, can be expressed as $N_\sigma = \sum_m n_{m,\sigma}$. The difference $(\bar{U} - \bar{J})$ is usually reported as the effective U parameter and this value will vary with the nature of the system.

2.1.3.3.2 Generalized Gradient Approximation

Since the electron density of molecules is not uniform throughout, the local value alone might not be the best way to determine the exchange-correlation functional. The next step would be to include the local value as well as the way in which the density is changing, also known as the gradient into the functional. Exchange-correlation functionals that include the local value and the gradient of the electron density are part of the generalized gradient approximation (GGA). The exchange-correlation energy may be represented by:

$$E_{XC}^{GGA}[\rho] = \int \rho(\mathbf{r}) \varepsilon_{XC}^{GGA}\left(\rho_\alpha, \rho_\beta, \nabla\rho_\alpha, \nabla\rho_\beta\right) d\mathbf{r} \tag{2.35}$$

where the energy density ε_{XC}^{GGA} accounts for potentially different spin up and spin down electron densities. GGA functional can also add the unrestricted Hartree-Fock method, similar to L(S)DA+U, in order to create the GGA+U method. Popular GGA functionals include the PBE functional developed by Perdew, Burke and Ernzerhof,[12-13] and a combination of the GGA exchange functional developed by Becke (B88)[14] with the GGA correlation functional developed by Lee, Yang and Parr (LYP)[15], known as BLYP.

2.1.3.3.2.1 GGA functional of Perdew, Burke, and Ernzerhof

The GGA functional developed by Perdew, Burke, and Ernzerhof (PBE) [12-13] is used throughout the research completed and presented in this Thesis. This functional was designed to be a first-principles numerical GGA where all parameters, except the parameters in the energy density of a uniform gas, $\varepsilon_{\mathrm{XC}}^{unif}(\rho_\alpha, \rho_\beta)$, are fundamental constants.[12] The derivations of the exchange and correlation functionals are dependent upon describing systems at limiting cases. The PBE functional retains correct features of the local spin density approximation while adding the energetically important features of gradient-corrected nonlocality. The correlation functional has the form:

$$\mathrm{E_C^{PBE}} = \int \mathrm{d^3r}\, \rho\left[\varepsilon_{\mathrm{C}}^{\mathrm{unif}}(\mathrm{r_s}, \zeta) + \mathrm{H}(\mathrm{r_s}, \zeta, \mathrm{t})\right] \tag{2.36}$$

where r_s is the local Seitz radius ($\rho = 3/4\pi \mathrm{r_s^3} = \mathrm{k_F^3}/3\pi^2$), $\zeta = \left(\rho_\alpha - \rho_\beta\right)/\rho$ is the relative spin polarization, $\mathrm{t} = |\nabla\rho|/2\phi \mathrm{k_s}\rho$ is a dimensionless gradient, $\phi(\zeta) = \left[(1+\zeta)^{2/3} + (1-\zeta)^{2/3}\right]/2$ is a spin-scaling factor, $\mathrm{k_s} = \sqrt{4\mathrm{k_F}/\pi \mathrm{a_0}}$ is the Thomas-Fermi screening wave number, $\mathrm{a_0} = \hbar^2/\mathrm{me}^2$, $\mathrm{H} = (\mathrm{e}^2/\mathrm{a_0})\gamma\phi^3 \ln\left\{1 + \frac{\beta}{\gamma}\mathrm{t}^2\left[\frac{1+\mathrm{At}^2}{1+\mathrm{At}^2+\mathrm{A}^2\mathrm{t}^4}\right]\right\}$, $\beta \approx 0.066725$, $\gamma = (1-\ln 2)/\pi^2 \approx 0.031091$, and $\mathrm{A} = \frac{\beta}{\gamma}\left[\exp\left\{-\varepsilon_{\mathrm{C}}^{\mathrm{unif}}/(\gamma\phi^3\mathrm{e}^2/\mathrm{a_0})\right\} - 1\right]^{-1}$. The exchange functional has the form:

$$\mathrm{E_X^{PBE}} = \int \mathrm{d^3r}\, \rho\varepsilon_{\mathrm{X}}^{\mathrm{unif}}(\rho)\mathrm{F_X(s)} \tag{2.37}$$

where $\varepsilon_{\mathrm{X}}^{\mathrm{unif}} = -3\mathrm{e}^2\mathrm{k_F}/4\pi$, $\mathrm{F_X(s)} = 1 + \kappa - \kappa/(1 + \mu\mathrm{s}^2/\kappa)$, $\kappa = 0.804$, $\mathrm{s} = |\nabla\rho|/2\mathrm{k_F}\rho = (\mathrm{r_s}/\mathrm{a_0})^{1/2}\phi\,\mathrm{t}/\mathrm{c}$ is another dimensionless density gradient, and $\mathrm{c} = (3\pi^2/16)^{1/3} \approx 1.2277$.

2.1.3.3.3 Hybrid Functionals

Since the exchange functional dominates the exchange-correlation functional, [7] it would be natural to improve the exchange expression in order to have an overall improvement of the entire exchange-correlation functional. GGAs tend to overbind, because the exchange-correlation hole is always inherently localized.[7] The only way to introduce delocalization of the exchange-correlation hole at zero interaction strength is by replacing a small amount of DFT exchange with exact exchange from Hartree-Fock theory.[7] Incorporating exact exchange to the DFT exchange-correlation functional leads to the so-called hybrid functionals, which have an exchange-correlation functional of the form:

$$\mathrm{E_{XC}^{Hybrid}} = \mathrm{aE_X^{HF}} + (1-\mathrm{a})\mathrm{E_X^{DFT}} + \mathrm{E_C^{DFT}} \tag{2.38}$$

where *a* may vary between 0 and 1, with *a* = 0 corresponding to the pure DFT treatment of the exchange and correlation, while *a* = 1 corresponds to pure Hartree-Fock treatment of the exchange with DFT treatment of the correlation. Becke[16] was the first to include exact exchange in the development of a 3-parameter functional expression, also using the correlation functional of Perdew and Wang (PW91),[17] to create the functional B3PW91:

$$\mathrm{E_{XC}^{B3PW91}} = \mathrm{E_{XC}^{LSDA}} + \mathrm{a}\left(\mathrm{E_X^{exact}} - \mathrm{E_X^{LSDA}}\right) + \mathrm{b}\Delta\mathrm{E_X^{B88}} + \mathrm{c}\Delta\mathrm{E_C^{PW91}} \tag{2.39}$$

where a = 0.20, b = 0.72, c = 0.81, $\Delta\mathrm{E_X^{B88}}$ is Becke's 1988 gradient correction to the LSDA exchange,[14] and ΔE_C^{PW91} is the 1991 gradient correction for the correlation of Perdew and Wang. The next year, Stephens *et al.* modified the B3PW91 functional to use the correlation functional of Lee, Yang and Parr (LYP) instead of the PW91 correlation functional.[18] This new functional was called B3LYP and it has the form:

$$\mathrm{E_{XC}^{B3LYP}} = (1-\mathrm{a})\mathrm{E_X^{LSDA}} + \mathrm{aE_X^{HF}} + \mathrm{b}\Delta\mathrm{E_X^{B88}} + \mathrm{cE_C^{LYP}} + (1-\mathrm{c})\mathrm{E_C^{VWN}} \tag{2.40}$$

where a, b, and c have the same values as in B3PW91. B3LYP has become the most popular and wide-spread functional to date. There are also one parameter and "parameter-free" hybrid functionals, such as PBE0, which includes 25% Hartree-Fock.[19] PBE0 uses perturbation theory to choose the amount of exact exchange, as opposed to empirically optimizing the parameters, meaning there are "zero" parameters.

2.1.3.4 Plane-wave Density Functional Theory

In order to perform a calculation on a chemical system, after choosing an appropriate method, one needs to select a basis set to use with the desired method. There are many different types of atomic basis sets used by chemists, including minimal basis sets (e.g. STO-3G),[20] Pople basis sets (e.g. 6-31G [21] and variants), or Dunning basis sets [22-23] (e.g. cc-pVDZ and variants), while physicists tend to use a plane-wave basis set. The plane-wave basis has its roots in solid-state theory. Solid crystals are made up of "building blocks" that are continuously repeated in all directions.[24] This "building block" is known as a unit cell. In order to have no breaks or changes in the structure where one block ends and the next one begins, the unit cell must have periodic boundary conditions. The periodicity produces a periodic potential, which imposes a periodicity on the density.[25] Plane-waves can be used as the generic basis set to expand the periodic part of the orbitals and have the form:

$$\phi_j(\mathbf{r},\mathbf{k}) = \sum_{\mathbf{G}} c_j(\mathbf{G},\mathbf{k}) \frac{1}{\sqrt{\Omega}} e^{i(\mathbf{G}+\mathbf{k})\cdot\mathbf{r}} \tag{2.41}$$

where $c_j(\mathbf{G},\mathbf{k})$ are the complex coefficients of the wave functions, $\frac{1}{\sqrt{\Omega}} e^{i(\mathbf{G}+\mathbf{k})\cdot\mathbf{r}}$ are the plane-waves, Ω is the volume of the unit cell, **G** is a vector in reciprocal space, and **k** is the

quantum number associated with the crystal momentum. The charge density can be expanded into a plane wave basis:

$$\rho(\mathbf{r}) = \frac{1}{\Omega}\sum_{j}\int f_j(\mathbf{k}) \sum_{\mathbf{G},\mathbf{G}'} c_j^*(\mathbf{G}',\mathbf{k}) c_j(\mathbf{G},\mathbf{k}) e^{i(\mathbf{G}+\mathbf{k})\cdot\mathbf{r}} d\mathbf{k} = \sum_{\mathbf{G}} \rho(\mathbf{G}) e^{i\mathbf{G}\cdot\mathbf{r}} \qquad (2.42)$$

where the sum over **G** vectors extends over twice the range of the sum in Equation 2.41. The total electronic energy and the gradient have particularly simple forms when expressed in plane-waves.[25] Plane-waves do not depend on the positions of the nuclei, which implies that the Pulay forces[26] vanish exactly within a finite basis. This means that the plane-waves are an unbiased basis set, in that they are "delocalized" in space and do not "favor" certain atoms or regions over others. Plane-waves are also attractive because derivatives in real space are simply multiplications in reciprocal space, and both spaces are easily accessible through fast Fourier transforms.

In real calculations, the sum over **G** in Equation 2.41 is truncated to a finite sum over a set of **k**-points, each with a respective weight, or contribution to the sum. This truncates the plane-wave basis set and is possible because the Kohn-Sham potential converges rapidly with increasing **G**. The number of **k**-points in each unit cell direction (a, b and c) should be increased until convergence of properties is reached with the next most dense grid of **k**-points. These **k**-point grids, or meshes, are usually expressed as (number of **k**-points in the a-direction × number of **k**-points in the b-direction × number of **k**-points in the c-direction), or 2 × 2 × 1, for example with 2 points in each of the a- and b-directions and only 1 in the c-direction. At each **k**-point, only **G** vectors with a kinetic energy lower than a given maximum cutoff are included in the basis.

$$\frac{1}{2}|\mathbf{k}+\mathbf{G}|^2 \leq E_{cut} \qquad (2.43)$$

The only way to improve the quality of the basis set is to increase the energy cutoff, E_{cut}. The number of plane waves at a given cutoff depends on the unit cell and the **k**-points. At the center of the Brillouin zone, the number of plane waves, N_{PW}, can be estimated as:

$$N_{PW} = \frac{1}{2\pi^2}\Omega E_{cut}^{3/2} \tag{2.44}$$

where E_{cut} and Ω are given in atomic units, i.e. Hartree and (Bohr)^3.

2.1.3.4.1 Brillouin Zone

The Brillouin zone (BZ) is the reciprocal space version of the unit cell. In a one dimensional system, the unit cell can be described by the length of the cell, **a**. The wave vector, **k**, can be described as the length of the unit cell in reciprocal space, and is related to **a**, such that $\mathbf{k} = \frac{2\pi}{\mathbf{a}}$. This can be extrapolated to higher dimensional systems. The first Brillouin zone for a one dimensional system is bounded by **k** values of $\pm \frac{\pi}{\mathbf{a}}$. A more formal definition is that the first Brillouin zone is the reciprocal space volume encompassed around a lattice point without crossing any Bragg planes. Generally, the first Brillouin zone is used to display energy bands and at special symmetry points in the Brillouin zone, the wave function and properties of the system are calculated. An image of high symmetry points found in an orthorhombic unit cell[27] is shown in Figure 2.1. The **k**-point meshes used in the calculations of the data in this Thesis consist of only the Γ-point, the center of the Brillouin zone, or are centered around the Γ-point, sometimes denoted as a Γ-centered Monkhorst-Pack grid in the literature and in computational program manuals.

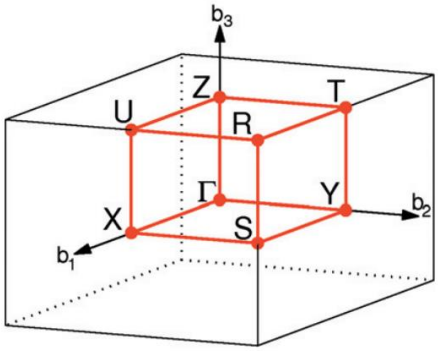

Figure 2.1: Cartoon of high symmetry positions in reciprocal space found in an orthorhombic unit cell ($\alpha = \beta = \gamma = 90°$, a1 ≠ a2 ≠ a3). Adapted from Setyawan and Curtarolo.[27]

2.1.3.4.2 Pseudopotentials

Plane-waves are always accompanied by pseudopotentials. The plane-waves describe the valence electrons, while the core electrons are described by a smooth, nodeless potential, known as a pseudopotential. For practical reasons, pseudopotentials should be additive and transferrable. Additivity can be easily achieved by building the pseudopotentials for atoms in reference states. Transferability means that the same pseudopotential should be adequate for an atom in all possible chemical environments. There are a few different types of pseudopotentials, including norm-conserving,[28] ultrasoft (Vanderbilt),[29] and projector-augmented wave (PAW) method.[30] In this Thesis, the PAW pseudopotentials will be used exclusively.

2.1.3.4.2.1 Norm-conserving pseudopotentials

Norm-conserving pseudopotentials only treat the chemically active, valence electrons explicitly. By applying the frozen core approximation, the inert, core electrons are considered, together with the nuclei, as rigid, non-polarizable ion cores. The

electrostatic and interactions of the valence electrons with the ion cores, such as the nuclear Coulomb attraction screened by the core electrons, Pauli repulsion, and exchange and correlation between core and valence electrons, are accounted for by angular momentum-dependent pseudopotentials. These pseudopotentials should reproduce the true potential and valence orbitals outside a chosen core region, but remain much weaker and smoother inside. The valence electrons are then described by smooth pseudo orbitals which play the same role as the true orbitals, while avoiding the nodal structure near the nuclei that keeps the core and valence states orthogonal in an all-electron framework. The "pseudization" of the valence wave functions, along with the removal of the core states, drastically simplifies a numerically accurate solution of the Kohn-Sham equations.[25]

2.1.3.4.2.2 Ultrasoft (Vanderbilt) Pseudopotentials

The norm conserving pseudopotentials have problems with elements that have strongly localized orbitals, which require large plane wave basis sets. In order to avoid these large basis sets, compromises were made, usually by increasing the core region, affecting the transferability of the pseudopotential, or reducing the plane wave energy cutoff, which sacrifices the accuracy and reliability of the calculation. Vanderbilt[29] decided to relax the constraint of norm conservation in the core region and introduced localized atom-centered augmentation charges, to make up for the charge deficit. The augmentation charges are defined as the charge difference between the all-electron and pseudo wave functions, but they are usually pseudized, in order to allow an efficient treatment on a regular grid. The core radius can now be chosen close to the nearest neighbor distance. The

augmentation charges must be calculated in a small cutoff radius in order to return the moments and the charge distribution of the all-electron wave function. [25]

2.1.3.4.2.3 Projector Augmented-Wave Method

The PAW[30] method is based on a formal division of the whole space Ω into distinct regions[25]: a collection of non-overlapping spherical regions around each atom Ω_a and the remaining, interstitial region, Ω_I:

$$\Omega = \Omega_I + \bigcup_a \Omega_a \tag{2.45}$$

The plane wave basis is the ideal choice for the interstitial region, but is difficult to use in order to describe the wave functions in the atomic sphere regions. This problem is addressed by introducing auxiliary wave functions which satisfy the following requirements. First, the auxiliary wave functions $\tilde{\phi}_i(\mathbf{r})$ can be obtained from the all-electron wave function $\phi_i(\mathbf{r})$ via an invertible linear transformation, T:

$$|\tilde{\phi}_i\rangle = T|\phi_i\rangle \tag{2.46}$$

$$|\phi_i\rangle = T^{-1}|\tilde{\phi}_i\rangle \tag{2.47}$$

Second, $\tilde{\phi}_i(\mathbf{r})$ is smooth, which implies that it can be represented by a plane wave basis set of a practical size everywhere, including the atomic sphere regions. The first requirement ensures that the Kohn-Sham equations can be reformulated equivalently in terms of $\tilde{\phi}_i(\mathbf{r})$, while the second requirement allows the entire process to be performed using the plane wave basis set.

In order to construct $\tilde{\phi}_i(\mathbf{r})$, the all-electron wave function must be defined first. For each atom, a set of local basis functions $\{\chi_\alpha^a\}$ is defined that is expected to accurately

describe the oscillating behavior of the relevant all-electron wave function, $\phi_i(\mathbf{r})$ within the corresponding atomic sphere. Projector functions $\{p_\alpha^a\}$ are also introduced such that:

$$\langle p_\beta^a | \chi_\alpha^a \rangle = \delta_{\alpha\beta} \tag{2.48}$$

$$p_\alpha^a(\mathbf{r}) = 0, \forall \mathbf{r} \subset \Omega_I \tag{2.49}$$

Using $\{\chi_\alpha^a\}$ and $\{p_\alpha^a\}$, the wave function $\phi_i(\mathbf{r})$ in the atomic sphere region can be represented by:

$$\phi_i(\mathbf{r}) = \sum_\alpha c_{i,\alpha}^a \chi_{i,\alpha}^a(\mathbf{r}) + \Delta_i^a(\mathbf{r}) \ , \forall \mathbf{r} \subset \Omega_a \tag{2.50}$$

where the coefficients $c_{i,\alpha}^a$ in the expansion are given by:

$$c_{i,\alpha}^a = \langle p_\alpha^a | \phi_i \rangle \tag{2.51}$$

The correction

$$|\Delta_i^a\rangle = \left(1 - \sum_\alpha |\chi_\alpha^a\rangle\langle p_\alpha^a|\right)|\phi_i\rangle \tag{2.52}$$

reflects the incompleteness of the set $\{\chi_\alpha^a\}$. As the size of the basis set gets larger, the local basis representation of $\phi_i(\mathbf{r})$ becomes more accurate and $\Delta_i^a(\mathbf{r})$ goes to zero.

The auxiliary wave functions, $\tilde{\phi}_i(\mathbf{r})$, can be constructed in a similar way, with an auxiliary smooth basis set $\{\tilde{\chi}_\alpha^a\}$, which is subject to the following conditions. First, the basis functions $\tilde{\chi}_\alpha^a(\mathbf{r})$ are smooth and can be expanded in terms of the plane wave basis set using a practical plane wave cutoff everywhere, particularly in the atomic sphere regions. Second, $\tilde{\chi}_\alpha^a(\mathbf{r})$ merges differentiably into $\chi_\alpha^a(\mathbf{r})$ outside the atomic spheres. Third, both $\tilde{\chi}_\alpha^a(\mathbf{r})$ and differences $\tilde{\chi}_\alpha^a(\mathbf{r}) - \chi_\alpha^a(\mathbf{r})$ form linearly independent sets. Given these properties, a smooth wave function $\tilde{\phi}_i(\mathbf{r})$ can be obtained, similar to $\phi_i(\mathbf{r})$ inside the atomic spheres:

$$\widetilde{\phi}_i(\mathbf{r}) = \sum_\alpha c_{i,\alpha}^a \tilde{\chi}_{i,\alpha}^a(\mathbf{r}) + \Delta_i^a(\mathbf{r}) \ , \forall \mathbf{r} \subset \Omega_a \tag{2.53}$$

where $\widetilde{\phi}_i(\mathbf{r})$ simply coincides with the all-electron wave function in the interstitial region. The transformation and inverse respectively can be expressed as:

$$T = 1 + \sum_a \sum_\alpha (|\tilde{\chi}_\alpha^a\rangle - |\chi_\alpha^a\rangle)\langle p_\alpha^a| \tag{2.54}$$

$$T^{-1} = 1 + \sum_a \sum_\alpha (|\chi_\alpha^a\rangle - |\tilde{\chi}_\alpha^a\rangle)\langle \tilde{p}_\alpha^a| \tag{2.55}$$

where a set of smooth projector functions $\{\tilde{p}_\alpha^a\}$ is defined as:

$$\langle \tilde{p}_\alpha^a| = \sum_\beta (p^a|\tilde{\chi}^a\rangle)_{\alpha\beta}^{-1}\langle p_\beta^a| \tag{2.56}$$

This relationship between $\{p_\alpha^a\}$ and $\{\tilde{p}_\alpha^a\}$ shows that the local basis expansion coefficients and the remainder can be represented alternatively as:

$$c_{i,\alpha}^a = \langle \tilde{p}_\alpha^a | \widetilde{\phi}_i \rangle \tag{2.57}$$

$$|\Delta_i^a\rangle = \left(1 - \sum_\alpha |\tilde{\chi}_\alpha^a\rangle\langle \tilde{p}_\alpha^a|\right)|\widetilde{\phi}_i\rangle \tag{2.58}$$

Equations 2.56 and 2.57 show that if the basis $\{\chi_\alpha^a\}$ provides an accurate local representation for $\phi_i(\mathbf{r})$, then the smooth basis $\{\tilde{\chi}_\alpha^a\}$ provides an accurate local representation for $\widetilde{\phi}_i(\mathbf{r})$ and vice versa. This is an important observation, since the objective of the transformation, T, is to completely eliminate $\phi_i(\mathbf{r})$ and search for $\widetilde{\phi}_i(\mathbf{r})$ directly.[25]

2.1.3.4.3 Smearing Methods

As mentioned above, in real calculations, the sum over **G** in Equation 2.40 is truncated to a finite sum over a set of **k**-points. These **k**-points are used as special points in the unit cell at which the energy and occupations of electronic bands are calculated. Smearing will broaden the bands in order to attempt to recreate the shape of the bands throughout the entire unit cell. There are different smearing methods available, but three in particular have been used in the research that is presented in this Thesis, the Gaussian-smearing method, the tetrahedron method with Blöchl corrections, and the first-order method of Methfessel and Paxton.

2.1.3.4.3.1 Gaussian-Smearing Method

The Gaussian-smearing method was developed by Fu and Ho as a way to weight the states near the Fermi level energy, in order to accelerate convergence of total energies with respect to the number of **k**-points sampled.[31] Due to the partial occupancy of bands near the Fermi level energy in metals, a large number of **k**-points must be chosen, in order to account for the Fermi surface. In this method, the energy of each calculated state is broadened by a Gaussian whose width is roughly equal to the dispersion of the energy bands between neighboring grid points near the Fermi surface. The Fermi level energy is determined from the Gaussian-modified density of states. The weight of each state is determined by the portion of the Gaussian distribution which lies under the Fermi level energy. This smearing method is good for calculating the total energy of semiconductors and metals, but it is not the most convenient for either. It is generally used when the desired

semiconductor unit cell size is large and only one or two **k**-points can be used, whereas the tetrahedron method with Blöchl corrections requires four or more **k**-points.

2.1.3.4.3.2 Tetrahedron Method with Blöchl Corrections

The tetrahedron method with Blöchl corrections[32] was developed in 1994 to address issues with the tetrahedron method[33-34], such as the cumbersome task of dividing the irreducible part of the first Brillouin zone for each symmetry group into tetrahedra and requiring a large number of matrix elements at the same time for Brillouin-zone integration, which was a challenging task for plane-wave-based electronic-structure programs. The traditional tetrahedron method determined the irreducible part of the Brillouin zone and divided it into tetrahedra. Eigenvalues and matrix elements were obtained for the **k**-points at the corners of the tetrahedra. Then, the integration for each tetrahedron was performed analytically, after linearly interpolating eigenvalues and matrix elements inside the tetrahedron. Analysis of the convergence behavior with increasing number of **k**-points shows that the integration error, $\delta\langle X\rangle$, decreases as $\delta\langle X\rangle \propto \Delta^2$, where Δ is a characteristic spacing between **k**-points. The number of **k**-points that have to be considered is proportional to $1/\Delta^3$. $\delta\langle X\rangle$ can be decomposed into two terms. One is due to the piecewise linear interpolation within the polyhedron that replaces the Fermi surface, while the other is the integral between the true Fermi surface and the polyhedron approximating it. For the sum of one-electron energies and the total energy, the errors due to the integral between the Fermi surface and the polyhedron are two orders of magnitude smaller than the integrals within the polyhedron. Therefore the dominant error in total energy calculations is due to integral within the polyhedron. The correction formula evaluates the difference $\delta\langle X\rangle =$

$\langle X\rangle - \langle\bar{X}\rangle$ between the integral of the true function $X(\mathbf{k})$ and the integral of its linearized version $\bar{X}(\mathbf{k})$ to leading order. It is given by:

$$\delta\langle X\rangle = \sum_{T} \frac{D_T(E_F)}{40} \sum_{ij} \left(\varepsilon_i X_j - \delta_{ij} \sum_{m} \varepsilon_m X_m \right) \tag{2.59}$$

The outermost sum is a sum over all tetrahedra, $D_T(E_F)$ is the contribution of one tetrahedron to the density of states at the Fermi level energy, ε_i are the one-particle energies, and X_i are the matrix elements at the four corners of the tetrahedron. An arrangement of tetrahedra has been shown to avoid mis-weighting the **k**-points as shown below in Figure 2.2.[35-36] With this method, the integration error decays exponentially with Δ, versus the conventional choice of tetrahedral decaying proportionally to Δ^2. This method is generally used in calculations of semiconductors, due to the speed of convergence and gives a good description of the electronic density of states.

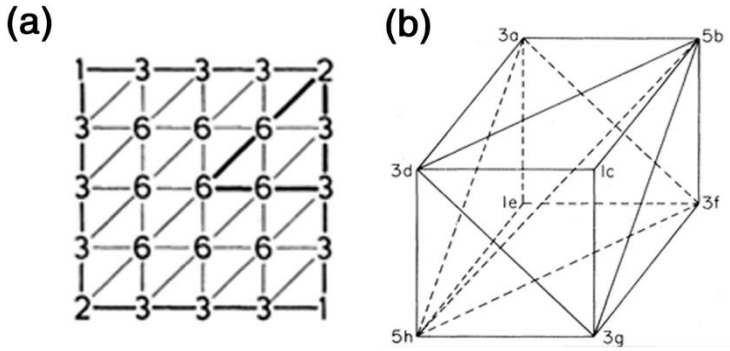

Figure 2.2: A way of dividing a two-dimensional square lattice into triangular regions so that there is no mis-weighting of k-points (a). The primitive cell is bounded by lines of medium thickness; an irreducible zone is bounded by heavy lines, and the triangles are bounded by weak lines. The numerals at the mesh points are the weight factors. For any point, this weight factor equals the number of triangles sharing that point. Adapted from Jepsen.[35] Division of a cube into six equal volume tetrahedra (b). The cube is first divided into two wedges by the plane (*dbfh*). The front wedge is then sliced by the plane (*dgb*) creating the tetrahedron (*dgbc*). The remaining piece is then sliced by the plane (*hbg*) creating tetrahedra (*hbfg*) and (*hbdg*). Similarly, the back wedge is sliced

into tetrahedra (*ahfe*), (*hbad*), and (*hbaf*). The number at each corner of the cube represents the number of tetrahedral vertices at the corner. Adapted from Kleinman.[36]

2.1.3.4.3.3 First-Order Method of Methfessel and Paxton

The smearing method of Methfessel and Paxton was developed in 1989 to improve the convergence of performing integrals of discontinuous periodic functions, due to the partial filling of energy bands in metals.[37] The method is based on making a hierarchy of smooth approximations to the step and δ functions, which are applied to integrals in the Brillouin zone (BZ). The goal is to evaluate:

$$\mathrm{I} = \int_{\mathrm{BZ}} \mathrm{S}(\mathrm{E}(\mathbf{k}) - \mathrm{E_F})\mathrm{f}(\mathbf{k})\mathrm{d}\mathbf{k} = \int_{-\infty}^{\infty} \mathrm{S}(\varepsilon - \mathrm{E_F})\mathrm{F}(\varepsilon)\mathrm{d}\varepsilon \tag{2.60}$$

where

$$\mathrm{F}(\varepsilon) = \int_{\mathrm{BZ}} \mathrm{f}(\mathbf{k})\delta\big(\varepsilon - \mathrm{E}(\mathbf{k})\big)\mathrm{d}\mathbf{k} \tag{2.61}$$

$E(\mathbf{k})$ represents an energy band as a function of wave vector and $\mathrm{E_F}$ is the Fermi level energy. The function to be integrated, f, is multiplied by the Fermi cutoff or step function: $S(x) = 1 - \Theta(x) = 1$ for $x \leq 0$ and 0 otherwise. $\mathrm{F}(\varepsilon)$ can change depending on the desired *I*. If *I* is supposed to be the total charge within the Fermi surface or the band energy, then $\mathrm{F}(\varepsilon)$ would be the density of states, $\mathrm{g}(\varepsilon)$, and $\mathrm{g}(\varepsilon)\varepsilon$, respectively. The method searches for successive smooth approximants to the step function, S_N, which have an error of zero if $\mathrm{F}(\varepsilon)$ is a polynomial of some order within the energy range determined by the choice of broadening. A characteristic broadening W can be used to create a dimensionless energy variable, $\mathrm{x} = (\varepsilon - \mathrm{E_F})/\mathrm{W}$, which will be used to look for a function $\mathrm{S_N(x)}$ to approximate

S(x). The first step is to find a suitable representation of the δ function δ(x), which will be integrated to obtain successive approximations to S(x). One expansion of δ(x) in a complete set of functions is:

$$\delta(x) = \sum_{n=0}^{\infty} A_n H_{2n}(x) e^{-x^2} \tag{2.62}$$

where H_n is the Hermite polynomial of degree *n*, and A_n are coefficients obtained using the orthogonality of the Hermite polynomials with respect to Gaussian weights $\int_{-\infty}^{\infty} H_n(x) H_m(x) e^{-x^2} dx = n!\, 2^n \sqrt{\pi} \delta_{nm}$:

$$A_n = \frac{H_{2n}(0)}{(2n)!\, 4^n \sqrt{\pi}} = \frac{(-1)^n}{n!\, 4^n \sqrt{\pi}} \tag{2.63}$$

Now the finite sum:

$$D_N(x) = \sum_{n\,=\,0}^{N} A_n H_{2n}(x) e^{-x^2} \tag{2.64}$$

is an approximation to the δ function. The step function may be approximated by integrating D_N:

$$S_N(x) = 1 - \int_{-\infty}^{x} D_N(t) dt \tag{2.65}$$

and making use of the identity $(d/dx)\left[H_n(x) e^{-x^2}\right] = -H_{n+1}(x) e^{-x^2}$ and the definition of the error function, we obtain:

$$S_0(x) = \frac{1}{2}\left(1 - \mathrm{erf}(x)\right) \tag{2.66}$$

$$S_N(x) = S_0(x) + \sum_{n=1}^{N} A_n H_{2n-1}(x) e^{-x^2} \tag{2.67}$$

in which the zero-order approximation S_0 corresponds to simple Fermi-Dirac smearing, and higher-order terms serve to correct the errors inherent in this procedure. $S_N(x)$ can be substituted for $S(x)$ in the integral $\int S(x)F(x)dx$ without experiencing significant error if $F(x)$ can be represented as a polynomial of degree 2N or less in the range where $S_N(x) - S(x)$ is appreciably nonzero; whereas S_0 will serve only in cases where $F(x)$ is constant in this interval. The method of Methfessel and Paxton is generally used in calculations of metals because it is variational with respect to partial occupancies, which gives an accurate description of the total energy for metals.

2.2 Programs Used

All quantum mechanics calculations in the subsequent Chapters have been performed as implemented in the following software suites: Vienna Ab Initio Simulation Package[38-39] (VASP) versions 5.2.12, 5.3.2, and 5.3.5 and Gaussian 09[40] (revisions A.02 and B.01). Custom Python scripts were created for some data analysis while Matlab and Perl scripts from Drs. Hong Li and Paul Winget were also used for data analysis. Scripts available for free on the internet from the Henkelman group at the University of Texas at Austin were used for evaluation of Bader charge analysis.[41] Visualization of system geometries and data was accomplished with the Visualization for Electronic and Structural Analysis (VESTA) program versions 2.1.5 and 3.1.6.[42]

2.3 References

1. Szabo, A.; Ostlund, N. S., *Modern Quantum Chemistry: Introduction to Advanced Electronic Structure Theory*. Dover: Mineola, NY, 1996.

2. Pyykkö, P. "Relativistic Effects in Structural Chemistry." *Chem. Rev.* **1988,** *88*, 563-594.

3. Hohenberg, P.; Kohn, W. "Inhomogeneous Electron Gas." *Phys. Rev.* **1964,** *136* (3B), B864-B871.

4. Kohn, W.; Sham, L. J. "Self-Consistent Equations Including Exchange and Correlation Effects." *Phys. Rev.* **1965,** *140* (4A), A1133-A1138.

5. Cramer, C. J., *Essentials of Computational Chemistry: Theories and Models*. 2nd ed.; Wiley: West Sussex, England, 2004.

6. Ceperley, D. M.; Alder, B. J. "Ground State of the Electron Gas by a Stochastic Method." *Phys. Rev. Lett.* **1980,** *45*, 566-569.

7. Becke, A. D. "Perspective: Fifty years of density-functional theory in chemical physics." *J. Chem. Phys.* **2014,** *140*, 18A301(1-18).

8. Vosko, S. H.; Wilk, L.; Nusair, M. "Accurate spin-dependent electron liquid correlation energies for local spin density calculations: a critical analysis." *Can. J. Phys.* **1980,** *58* (8), 1200-1211.

9. Perdew, J. P.; Zunger, A. "Self-interaction correction to density-functional approximations for many-electron systems." *Phys. Rev. B* **1981,** *23* (10), 5048-5079.

10. Perdew, J. P.; Wang, Y. "Accurate and simple analytic representation of the electron-gas correlation energy." *Phys. Rev. B* **1992,** *45* (23), 13244-13249.

11. Dudarev, S. L.; Botton, G. A.; Savrasov, S. Y.; Humphreys, C. J.; Sutton, A. P. "Energy-loss spectra and the stability of nickel oxide: An LSDA+U study." *Phys. Rev. B* **1998,** *57* (3), 1505-1509.

12. Perdew, J. P.; Burke, K.; Ernzerhof, M. "Generalized Gradient Approximation Made Simple." *Phys. Rev. Lett.* **1996,** *77* (18), 3865-3868.

13. Perdew, J. P.; Burke, K.; Ernzerhof, M. "Generalized Gradient Approximation Made Simple [Phys. Rev. Lett. 77, 3865 (1996)] Errata." *Phys. Rev. Lett.* **1997,** *78* (7), 1396.

14. Becke, A. D. "Density-functional exchange-energy approximation with correct asymptotic behavior." *Phys. Rev. A* **1988,** *38* (6), 3098-3100.

15. Lee, C.; Yang, W.; Parr, R. G. "Development of the Colle-Salvetti correlation-energy formula into a functional of the electron density." *Phys. Rev. B* **1988,** *37* (2), 785-789.

16. Becke, A. D. "Density-functional thermochemistry. III. The role of exact exchange." *Journal of Chemical Physics* **1993,** *98*, 5648-5652.

17. Perdew, J. P.; Chevary, J. A.; Vosko, S. H.; Jackson, K. A.; Pederson, M. R.; Singh, D. J.; Fiolhais, C. "Atoms, molecules, solids and surfaces: Applications of the generalized gradient approximation for exchange and correlation." *Phys. Rev. B* **1992,** *46* (11), 6671-6687.

18. Stephens, P. J.; Devlin, F. J.; Chabalowski, C. F.; Frisch, M. J. "Ab Initio Calculation of Vibrational Absorption and Circular Dichroism Spectra Using Density Functional Force Fields." *J. Phys. Chem.* **1994,** *98* (45), 11623-11627.

19. Adamo, C.; Barone, V. "Toward reliable density functional methods without adjustable parameters: The PBE0 model." *J. Chem. Phys.* **1999,** *110* (13), 6158-6170.

20. Hehre, W. J.; Stewart, R. F.; Pople, J. A. "Self-Consistent Molecular-Orbital Methods. I. Use of Gaussian Expansions of Slater-Type Atomic Orbitals." *J. Chem. Phys.* **1969,** *51* (6), 2657-2664.

21. Hehre, W. J.; Ditchfield, R.; Pople, J. A. "Self-Consistent Molecular Orbital Methods. XII. Further Extensions of Gaussian-Type Basis Sets for Use in Molecular Orbital Studies of Organic Molecules." *J. Chem. Phys.* **1972,** *56* (5), 2257-2261.

22. Dunning, T. H. "Gaussian basis sets for use in correlated molecular calculations. I. The atoms boron through neon and hydrogen." *J. Chem. Phys.* **1989,** *90*, 1007-1023.

23. Kendall, R. A.; Dunning, T. A.; Harrison, R. J. "Electron affinities of the first-row atoms revisited. Systematic basis sets and wave functions." *J. Chem. Phys.* **1992,** *96*, 6796-6806.

24. Smart, L. E.; Moore, E. A., *Solid State Chemistry: An Introduction*. Third ed.; CRC Press: Boca Raton, FL, 2005.

25. Marx, D.; Hutter, J., *Ab Initio Molecular Dynamics: Basic Theory and Advanced Methods*. Cambridge University Press: New York, 2009.

26. Pulay, P. "Ab initio calculation of force constants and equilibrium geometries in polyatomic molecules." *Mol. Phys.* **1969,** *17* (2), 197-204.

27. Setyawan, W.; Curtarolo, S. "High-throughput electronic band structure calculations: Challenges and tools." *Comput. Mater. Sci.* **2010,** *49* (2), 299-312.

28. Hamann, D. R.; Schlüter, M.; Chiang, C. "Norm-Conserving Pseudopotentials." *Phys. Rev. Lett.* **1979,** *43* (20), 1494-1497.

29. Vanderbilt, D. "Soft self-consistent pseudopotentials in a generalized eigenvalue formalism." *Phys. Rev. B* **1990,** *41* (11), 7892-7895.

30. Blöchl, P. E. "Projector augmented-wave method." *Phys. Rev. B* **1994,** *50* (24), 17953-17979.

31. Fu, C.-L.; Ho, K.-M. "First-principles calculation of the equilibrium ground-state properties of transition metals: Applications to Nb and Mo." *Phys. Rev. B* **1983,** *28* (10), 5480-5486.

32. Blöchl, P. E.; Jepsen, O.; Andersen, O. K. "Improved tetrahedron method for Brillouin-zone integrations." *Phys. Rev. B* **1994,** *49* (23), 16223-16233.

33. Jepsen, O.; Andersen, O. K. "The electronic structure of h.c.p. Ytterbium." *Solid State Commun.* **1971,** *9* (20), 1763-1767.

34. Lehmann, G.; Taut, M. "On the Numerical Calculation of the Density of States and Related Properties." *Phys. Status Solidi B* **1972,** *54* (2), 469-477.

35. Jepsen, O.; Andersen, O. K. "No error in the tetrahedron integration scheme." *Phys. Rev. B* **1984,** *29* (10), 5965.

36. Kleinman, L. "Error in the tetrahedron integration scheme." *Phys. Rev. B* **1983,** *18* (2), 1139-1141.

37. Methfessel, M.; Paxton, A. T. "High-precision sampling for Brillouin-zone integration in metals." *Phys. Rev. B* **1989,** *40* (6), 3616-3621.

38. Kresse, G.; Furthmüller, J. "Efficiency of ab-inito total energy calculations for metals and semiconductors using a plane-wave basis set." *Comput. Mater. Sci.* **1996,** *6* (1), 15-50.

39. Kresse, G.; Furthmüller, J. "Efficient iterative schemes for ab initio total-energy calculations using a plane-wave basis set." *Phys. Rev. B* **1996,** *54* (16), 11169-11186.

40. Frisch, M. J.; Trucks, G. W.; Schlegel, H. B.; Scuseria, G. E.; Robb, M. A.; Cheeseman, J. R.; Scalmani, G.; Barone, V.; Mennucci, B.; Petersson, G. A.; Nakatsuji, H.; Caricato, M.; Li, X.; Hratchian, H. P.; Izmaylov, A. F.; Bloino, J.; Zheng, G.; Sonnenberg, J. L.; Hada, M.; Ehara, M.; Toyota, K.; Fukuda, R.; Hasegawa, J.; Ishida, M.; Nakajima, T.; Honda, Y.; Kitao, O.; Nakai, H.; Vreven, T.; Montgomery, J. A., Jr.; ; Peralta, J. E.; Ogliaro, F.; Bearpark, M.; Heyd, J. J.; Brothers, E.; Kudin, K. N.; Staroverov, V. N.; Kobayashi, R.; Normand, J.; Raghavachari, K.; Rendell, A.; Burant, J. C.; Iyengar, S. S.; Tomasi, J.; Cossi, M.; Rega, N.; Millam, J. M.; Klene, M.; Knox, J. E.; Cross, J. B.; Bakken, V.; Adamo, C.; Jaramillo, J.; Gomperts, R.; Stratmann, R. E.; Yazyev, O.; Austin, A. J.; Cammi, R.; Pomelli, C.; Ochterski, J. W.; Martin, R. L.; Morokuma, K.; Zakrzewski, V. G.; Voth, G. A.; Salvador, P.; Dannenberg, J. J.; Dapprich, S.; Daniels, A. D.; Farkas, Ö.; Foresman, J. B.; Ortiz, J. V.; Cioslowski, J.; Fox, D. J. *Gaussian 09*, Gaussian, Inc.: Wallingford, CT, 2009.

41. Tang, W.; Sanville, E.; Henkelman, G. "A grid-based Bader analysis algorithm without lattice bias." *J. Phys.: Condens. Matter* **2009,** *21*, 084204(1-7).

42. Momma, K.; Izumi, F. "VESTA 3 for three-dimensional visualization of crystal, volumetric and morphology data." *J. Appl. Crystallogr.* **2011,** *44* (6), 1272-1276.

CHAPTER 3

PENTAMETHYLIRIDOCENE FOR DECREASING THE WORK FUNCTION OF GOLD AND INDIUM TIN OXIDE

3.1 Introduction

Organic optoelectronic devices, such as OPVs or OLEDs, require a low work function (Φ) electrode for electron injection to (for OLEDs), or collection from (for OPVs) the electron transport levels of organic semiconductors. Traditional low-Φ metals, e.g. Ca or Mg, are highly reactive and have to be deposited on top of the organic semiconductor layer under inert atmosphere conditions.[1-2] Thus, alternative low-Φ electrodes are highly desirable.

Previous approaches for lowering the work function have been introduced in Section 1.2.4.2, including the physisorbed surface modifiers like PEI(E), redox-active materials, and organometallic sandwich complexes. Here, we investigate organometallic compounds at the DFT level to understand: (i) the mechanism of work function modification (ΔΦ); and (ii) the contributions from potential synthetic byproducts. We consider the interaction of a metal (Au) and a metal oxide (ITO) surface with pentamethyliridocene (IrCpCp*), a prototypical 19-electron sandwich complex, its dimer precursor, and potential byproducts. We have evaluated the electron donating ability of

both the dimer and monomer, in terms of the Φ reduction of Au(111) and ITO(222) surfaces. This work has been published in *Organic Electronics*, **2016**, *37*, 263-270.[3]

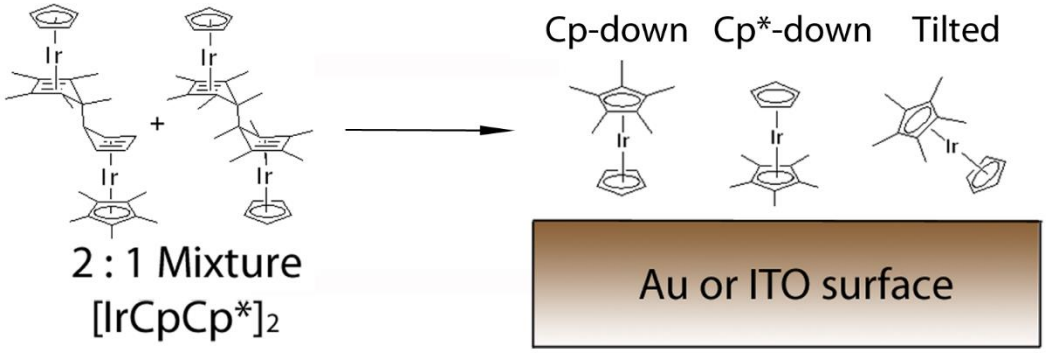

Figure 3.1: The IrCpCp* dimer and the possible orientations of the monomers and their abbreviations used throughout this work. Reprinted with permission from Elsevier.[3]

3.2 Computational Methodology

To describe the ITO(222) surface, we use the repeated-slab approach and a surface structural model proposed in our previous work,[4] which consists of 84 indium, 12 tin, 144 oxygen, and 24 hydrogen atoms in an orthogonal 24.79 × 14.32 $Å^2$ surface unit cell, where all of the oxygen atoms above the top layer of metal atoms are fully saturated by hydrogen atoms. The ITO slab consists of three In(Sn)-O layers. When a monomer is added to the ITO surface unit cell, the resulting molecular coverage is 2.82×10^{13} molecules cm^{-2}. This coverage is close to the experimentally evaluated coverage based on the Ir/In ratio obtained from the XPS experiments.[5] The atomic positions of the top layer, surface hydroxyls, and molecular adsorbate are allowed to relax over the course of geometry relaxations while the bottom two layers of the slab remain fixed.

The same repeated-slab approach is applied to the Au(111) surface. As the molecular coverage on gold is difficult to ascertain from experiments,[5] we used three coverages, realized by orthogonal unit cells with different sizes, to explore the effects of variations in molecular coverage. The lateral dimensions of the unit cells along the [11-2] and [1-10] directions are 8.63 × 9.97 $Å^2$, 17.27 × 9.97 $Å^2$, and 17.27 × 19.94 $Å^2$, and are taken from the experimental bulk lattice parameters.[1, 6] We note here that the lattice parameters optimized at the PBE-D2 level for bulk gold have been shown to be very close to the experimental values.[7] When one monomer or dimer is present in the unit cell, the molecular coverages are 1.16×10^{14} molecules cm^{-2}, 5.81×10^{13} molecules cm^{-2}, and 2.90×10^{13} molecules cm^{-2} for the smallest, second largest, and largest gold unit cells, respectively. When the monomer is in the smallest unit cell and when the dimer is in the second largest unit cell, the iridium to gold ratios are the same, and these cases will be denoted as high coverage (HC). If the monomer is in the second largest unit cell or the dimer is in the largest unit cell, the iridium to gold ratio is again the same, and these will be denoted as medium coverage (MC). The monomer in the largest unit cell will be denoted as low coverage (LC). The largest gold unit cell has approximately the same surface area as the ITO model. Each gold slab consists of five atomic layers with the bottom three layers frozen at the optimized crystal structure while the top two layers, and any molecular adsorbate, are allowed to relax over the course of geometry relaxations. In both the gold and ITO cases, the slabs are separated by a vacuum space larger than 20 Å.

All calculations were carried out using the Vienna Ab Initio Simulation Package (VASP).[8-9] The calculations were performed with plane-wave basis sets with an energy cut off of 400 eV and 300 eV for the gold and ITO calculations, respectively; the projector

augmented wave (PAW) method[10] was used to describe the valence-core electron interactions. We chose the generalized gradient approximation (GGA) exchange-correlation functional of Perdew, Burke, and Ernzerhof (PBE),[11-12] augmented by the empirical D2 dispersion correction of Grimme[13] in order to describe the non-specific interactions of pentamethyliridocene[5] with the metal or metal oxide surfaces. While PBE-D2 has deficiencies in the binding energies and geometries,[14] it can be expected to provide a semi-qualitative description, at a reasonable computational cost. As the monomer has an odd number of electrons, spin-polarized calculations were performed for both the isolated monomer and the monomer on the surface. The spin-polarized results for the monomer-on-substrate complex show little change in the Fermi level energy, magnetization, and density of states compared to those in the absence of spin-polarization (therefore, the results presented below are essentially from calculations without spin-polarization, with a detailed comparison given in Table 3.1). Despite the limitations of PBE, it has been used to describe charge transfer systems, such as perylene-3,4,9,10-tetracarboxylicdiimide (PTCDI),[15] perylene-3,4,9,10-tetracarboxylic dianhydride (PTCDA)[16] and C_{60} [17] on ZnO, as well as a donor-acceptor complex of tetrafluorotetracyanoquinodimethane (F_4-TCNQ) with t-butyl carbazole-phosphonic acid modified ITO.[18] In these earlier works, the work function change and charge-transfer characters have been calculated at the PBE level and good agreement with experiments has been reported.[15-17] In the gold calculations, a 2 × 2 × 1 Monkhorst-Pack k-point grid was used for geometry optimizations for all unit cells, while 6 × 6 × 1, 3 × 6 × 1, and 3 × 3 × 1 Monkhorst-Pack k-point grids were used for self-consistent total-energy calculations for the smallest, second largest, and the largest unit cells, respectively. In the ITO calculations, only the Γ-point was employed for geometry

optimizations, while a 2 × 2 × 1 Monkhorst-Pack k-point grid was considered for total-energy calculations. The Methfessel and Paxton[19] occupation scheme with a smearing of 0.1 eV was used for Brillouin-zone integrations in the calculations on both gold and ITO surfaces.

To calculate the electronic structures of the isolated monomers and dimers, a periodically repeated box of 40 × 40 × 40 $Å^3$ and 45 × 45 × 45 $Å^3$ was taken with the monomer or dimer, respectively, at the center of the boxes. For the isolated monomer (carrying an odd number of electrons), we compared the density of states (DOS) and Bader charges calculated[20] with and without spin polarizations. Although there is a half-occupied molecular orbital crossing the Fermi level energy in the DOS for the case without spin polarizations (compare the DOS in Figure 3.2 and Figure 3.3, calculated for an isolated monomer with and without spin-polarizations), the Bader charges for the monomer with and without spin-polarizations are remarkably similar, with differences on the order of 0.01 |e| (see Table 3.2; note that the Gaussian smearing method was used for the isolated systems and only the Γ-point was employed in such calculations). Bader charges are used here, and while it is difficult to assess the accuracy of atomic partial charges, these charges have an estimated error of less than 15%.[21]

Geometry optimizations were performed using a damped molecular dynamics scheme until the forces were <0.03 eV/Å for gold calculations[22] and <0.04 eV/Å for ITO calculations.[23] To compensate for possible dipole-dipole interactions between the asymmetric slabs, a dipole sheet is inserted into the vacuum gap.

Table 3.1: Comparison of the geometry optimizations of HC Cp*-down on Au(111) with respect to spin-polarization. All calculations have been performed at the PBE-D2 level.

HC Cp*-down geom. opt. (PBE/PW)	Total Energy (eV)	Fermi Level Energy (eV)	Magnetization
Without Spin-Polarization	-477.12147	-0.9407	----
Spin-Polarized	-477.12133	-0.9406	0.0000000
Spin-Polarized with Ir μ_B = 2	-477.12131	-0.9405	0.0000000

Table 3.2: Comparison of the Bader charges with respect to spin-polarization for the isolated Cp*-down configuration with Gaussian smearing. All calculations have been performed at the PBE-D2 level. All units in |e|.

Bader Charges	Without Spin-Polarization	With Spin-Polarization
Total	-0.0001	-0.0001
Cp ring	-0.2089	-0.2126
Cp* ring	-0.1223	-0.1250
Ir atom	0.3311	0.3375

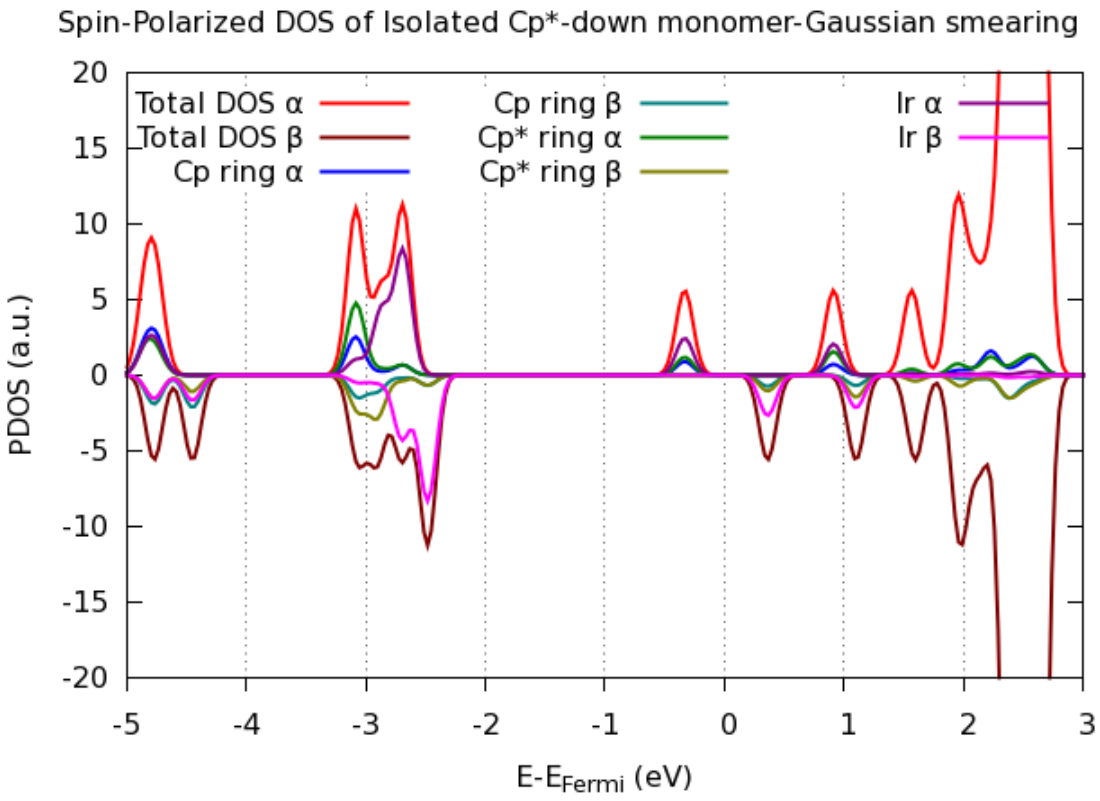

Figure 3.2: Spin-polarized density of states for the isolated Cp*-down monomer near the Fermi level energy, decomposed into the Cp ring, Cp* ring and Ir atom within the monomer. Reprinted with permission from Elsevier.[3]

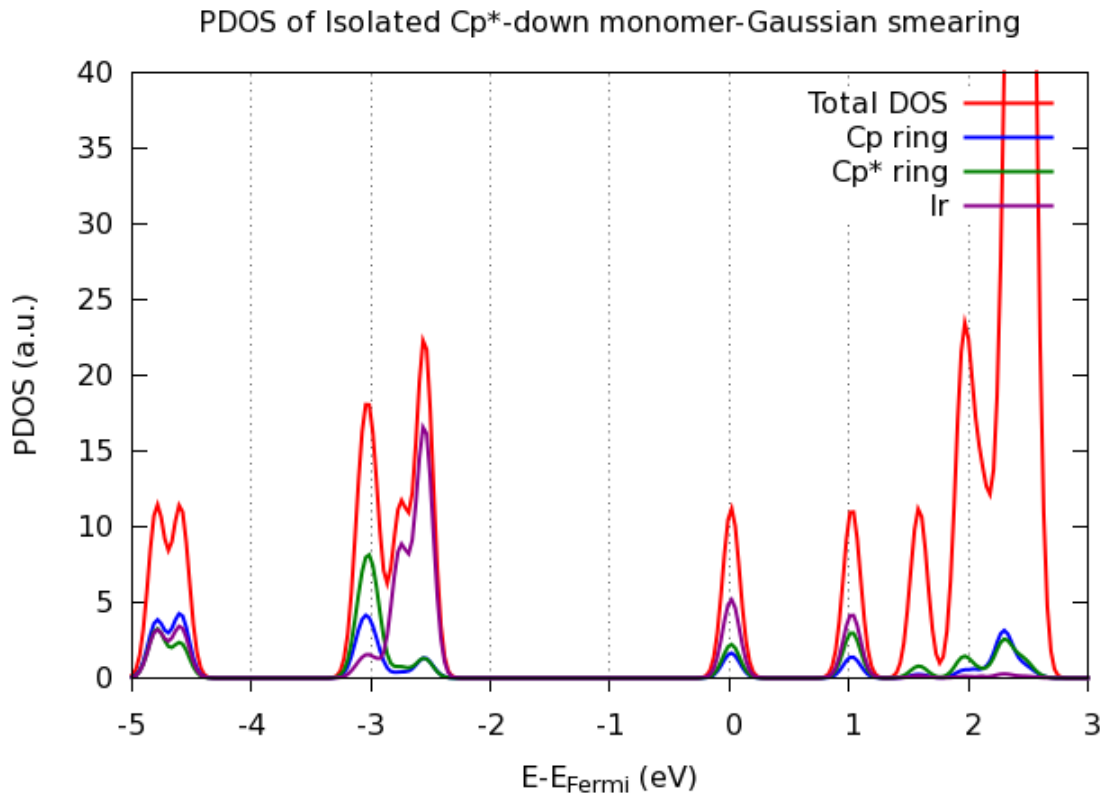

Figure 3.3: Projected density of states (PDOS) for the different components of the isolated Cp*-down monomer, namely the Cp ring, Cp* ring, and Ir atom, shown near the Fermi level energy. Reprinted with permission from Elsevier.[3]

3.3 Results and Discussion

3.3.1 Binding Configurations and Energies

Starting from optimized structures of the bare surfaces and monomers, each of the three possible monomer configurations, shown in Figure 3.4, were generated with an initial monomer-surface distance of approximately 2.5 Å. Two structures have the asymmetric ends of the sandwich complex facing the surface, with either the Cp or Cp* ring co-facial to the surface, denoted as “Cp-down” or “Cp*-down”. There occurs a third configuration in which the iridium interacts directly with the surface, denoted as “Tilted”. The Cp*-down

configuration is most stable for the monomer; we used this configuration as the starting point for the dimer optimization.

Experimentally, Au or ITO were treated in a nitrogen atmosphere with solutions of $(IrCpCp^*)_2$ in toluene. Physisorption of pentamethyliridocene is thought to be non-specific.[5] Since van der Waals interactions are not well described by standard density functionals, we have included a dispersion correction developed by Grimme.[13] Figure 3.4 shows the optimized structure and relative energies of the monomers on Au(111) for medium coverage (MC) (a-c) and on ITO(222) (e-g). The Cp*-down configuration is the global minimum for both surfaces, with the Cp-down and tilted configurations lying significantly higher in energy (by nearly 3 eV) upon complexation to the Au surface. For the high coverage (HC) gold surface, the global minimum is the tilted configuration (see Table 3.3). This is likely due to the increased intermolecular dispersion interactions at this coverage, rather than interactions with the surface.

Table 3.3: Relative energies of the iridium monomers on the Au(111) surface at high coverage with D2 dispersion correction. All values are in eV.

Relative Energy	**Cp-down**	**Cp*-down**	**Tilted**
PBE-D2	+1.24	+0.24	0.00

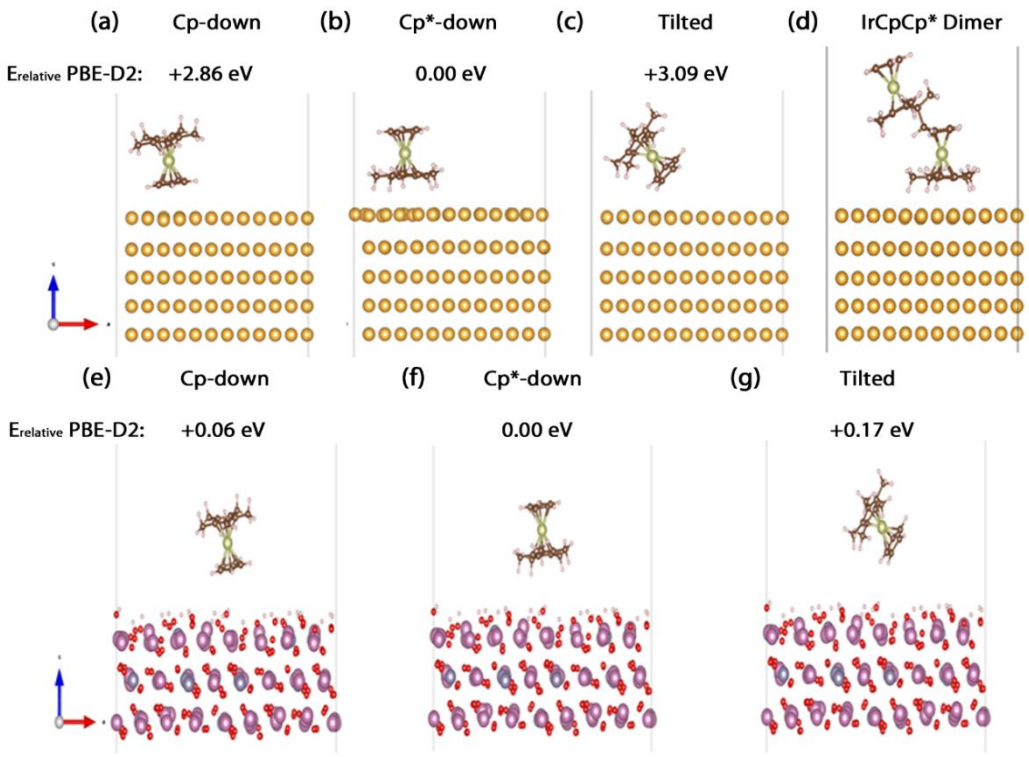

Figure 3.4: Optimized PBE-D2 geometries of the iridium monomers (a-c) and dimer (d) on the Au(111) surface at medium coverage and (e-g) monomers on the ITO(222) surface. The relative energies for the monomer complexes on the surfaces are also given. Reprinted with permission from Elsevier.[3]

The Cp-down configuration is consistently higher in energy than the Cp*-down configuration, although the 5-membered ring is closer to the gold and ITO surfaces in the former configuration. For instance, on the MC-gold surface, the center of the Cp ring is 2.88 Å from the surface, while the Cp* ring is 3.19 Å away (Ir atom: 4.69 and 5.00 Å away, respectively) from the surface. On ITO, passivation of the surface by hydroxylation prevents as close of an approach, with the Cp ring 3.27 Å from the surface, and the Cp* ring 4.09 Å away (Ir atom: 5.08 and 5.91 Å away, respectively). Such an energy stabilization over the Cp*-down configuration is due to the much stronger van der Waals interactions between the surfaces and the Cp*ring than the Cp ring.

The geometric structures of the isolated monomer, dimer, and associated cations have been calculated in an earlier work, using the M06 meta-GGA exchange-correlation functional and compared to available X-ray data.[24] Here we briefly describe the main geometric features obtained using a similar methodology as the surface calculations (with Gaussian smearing rather than the Methfessel and Paxton occupation scheme). The dimer contains two moieties, each of which being a η^4-Cp (η^5-Cp*) sandwich compound. The η^4-Cp ligand acts as a cyclopentadiene fragment, with the average Ir-C_{diene} atomic distance of 2.15 Å being smaller than the average Ir-C_{Cp*} distance of 2.27 Å. The uncoordinated sp^3 carbon atom lies out of plane of the butadiene fragment, with a long Ir-C bond with an average distance of 2.78 Å. The 19-electron monomer cation exists as a sandwich compound with a small bite angle and the Cp and Cp* atoms nearly equidistant, with average distances of 2.31 Å and 2.34 Å. A schematic of these distances are shown in Figure 3.5.

Upon monomer binding to the MC-Au(111) surface, there is a large change in the atomic distances. The Ir-C_{Cp*} distance becomes 2.19 Å, with the carbon atoms in the former η^4-cyclopentadiene ligand becoming planar, with an average C-Ir distance of 2.21 Å. The hapticity and bond distances are similar to those seen in the *cation* monomer structure. The dimer also undergoes geometrical changes upon interaction with gold, with the geometric change different in each monomer moiety. The monomer moiety closest to the surface experiences a similar evolution as the isolated monomer on the surface, with the C_{Cp*}-Ir distance contracting by 0.06 Å compared to the isolated dimer, to become 2.20 Å. The sp^3 carbon of the monomer moiety closest to the surface remains out of plane relative to the diene fragment, although the distance to the Ir atom becomes smaller, going from 2.77 to

2.63 Å. The monomer moieties farther from the surface have only small changes in the bond distances. The central C-C bond expands slightly from 1.58 to 1.59 Å. Details on the specific geometries of the complexes and changes after interaction with the surface are given in Table 3.4.

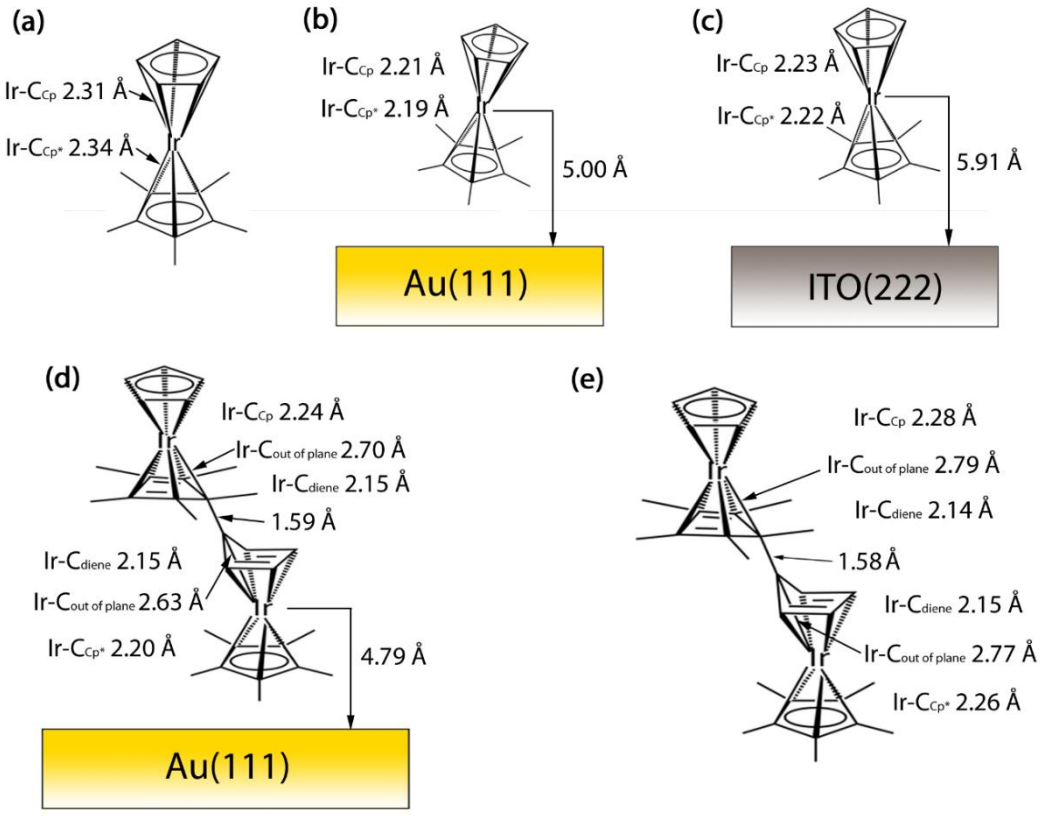

Figure 3.5: Average distances from the iridium to the carbon atoms of the Cp (Ir-C_{Cp}) and Cp* rings (Ir-C_{Cp*}) and distance to the surface (if present) in the isolated monomer (a), the MC Cp*-down monomer on gold (b), the Cp*-down monomer on ITO (c), the MC dimer on gold (d), and the isolated dimer (e). The dimer also has Ir-C_{diene} and Ir-$C_{out\ of\ plane}$ distances for the rings that bind the two monomer portions together. Reprinted with permission from Elsevier.[3]

Table 3.4: Distances between the center of the ring closest to the surface of the IrCpCp* complex and the top-most atom of the surface, between the iridium atom and the top-most atom of the surface, between the center of the Cp ring and the iridium atom, and between the center of the Cp* ring and the iridium atom from the optimized geometries. The numbers in parentheses are for the monomer portion farthest from the surface in the dimer cases. All calculations have been performed at the PBE-D2 level. All values are in Å.

System	Center of closest ring–top of surface D2	Ir of complex – top of surface D2	Cp ring to Ir	Cp* ring to Ir
IrCpCp* HC on Au [a]			1.84 ± 0.01	1.82 ± 0.01
Cp-down	2.85	4.67		
Cp*-down	3.33	5.14		
Tilted	3.55	4.66		
IrCpCp* MC on Au [b]			1.84 ± 0.005	1.82 ± 0.01
Cp-down	2.88	4.69		
Cp*-down	3.19	5.00		
Tilted	3.73	4.95		
IrCpCp*+H MC on Au [b]			1.89 ± 0.02	1.90 ± 0.03
Cp-down + H	2.78	4.64		
Cp*-down + H	5.24	4.65		
Tilted + H	3.77	5.10		
IrCpCp* LC Cp*-down on Au [c]	3.35	5.16	1.84	1.82
IrCpCp* HC dimer on Au [a]	3.40	5.47	1.93(1.89)	1.87(1.91)
IrCpCp* MC dimer on Au [b]	2.97	4.79	1.88(1.87)	1.82(1.90)
IrCpCp* on ITO			1.86 ± 0.0003	1.84 ± 0.002
Cp-down	3.27	5.08		
Cp*-down	4.09	5.91		
Tilted	4.57	5.71		
IrCpCp*+H on ITO			1.90 ± 0.02	1.89 ± 0.03
Cp-down + H	3.02	4.84		
Cp*-down + H	5.78	5.33		
Tilted + H	4.24	5.48		
Isolated IrCpCp* monomer			1.96	1.99
Isolated IrCpCp* dimer			1.92(1.93)	1.89(1.92)

[a] HC denotes high coverage, or a monomer in the smallest unit cell, or the dimer in the second largest unit cell. [b] MC denotes middle coverage, or a monomer in the second largest unit cell, or the dimer in the largest unit cell. [c] LC denotes low coverage, or a monomer in the largest unit cell.

3.3.2 Work Function Modification by Monomer

The work function (Φ) of a bare or modified surface is calculated using Equation 1.2, where $V_{vac.}$ is the plane averaged electrostatic potential energy of an electron in the vacuum region away from the slab, at a distance far enough away that the potential energy has reached its asymptotic value; E_F is the Fermi level energy of the system. For the

Au(111) MC surface, the calculated value is 5.14 eV, which compares very well to experimental data of 4.93 - 5.22 eV[5, 25-26] and previous calculations.[22, 26-28] The work function of the completely hydroxylated ITO surface considered here is 3.03 eV, which is substantially smaller than the experimental results that are in the range 4.0 – 6.1 eV. We note that the experimental value is sensitive to preparation conditions and nature of measurements;[5, 29-31] also, when the surface OH coverage is reduced to 1/6 of the current value (6.76×10^{14} /cm^2), the calculated work function of the model ITO surface reaches 4.24 eV.[32] We have shown earlier that, in spite of the low value of the calculated Φ for this ITO model surface, the work function modifications upon deposition of various monolayers on the surface, were reproduced accurately.[33]

The work function modification, $\Delta\Phi$, for all of the coverages of the three IrCpCp* monomers on HC and MC-gold and ITO and the Cp*-down monomer on LC-gold are presented in Table 3.5. The average modification for the Au(111) by MC-monolayer is -2.64 eV, with values ranging from -2.39 to -2.80 eV for the different configurations. The calculated $\Delta\Phi$ at this coverage is overestimated compared to the experimental value of -1.87 eV. It is important to note, however, that the calculated work function is strongly coverage dependent; for example, the Cp*-down configuration at LC is calculated to have a work function modification of -1.32 eV, while at MC and HC, the work function modifications are -2.39 eV and -3.44 eV, respectively. Since the coverage on the Au(111) has not been determined experimentally, the discrepancy can (at least partly) be attributed to variations in the coverages between theory and experiment. The modification due to a monolayer of the monomer on ITO of -1.23 eV is similar to the modification seen experimentally, -1.34 eV; in this case, the surface coverage considered in the calculations

is in fact close to the experimental coverage.[5] Comparison between the D2 dispersion correction[13] used here and the D3 correction[34] used in the work presented in Chapter 4 was performed on the most stable configuration at HC, Cp* down. The Φ and work function breakdown results are shown in Table 3.5. The D3 corrected ΔΦ results are slightly larger (-3.66 eV) than the D2 corrected (-3.44), mainly because the interface dipole contribution is larger by almost 0.3 eV and the geometry reorganization contribution is an order of magnitude larger as well (0.1 eV for D3 vs. 0.01 for D2). The molecular dipole contribution remained the same between the D2 and D3 dispersion corrections.

The terms from the work function modification breakdown scheme, discussed in Section 1.2.3.2.1, are collected in Table 3.5. The $\Delta V_{mol.}$ component, a function of the dipole moment of the molecular layer perpendicular to the surface,[35-36] is small in all cases as there is only a little non-zero dipole moment in pentamethyliridocene due to the slightly different electron affinities of the Cp and Cp* rings. Thus, the dipole moments of the Cp- and Cp*-down configurations at MC are opposite in sign and give rise to $\Delta V_{mol.}$ contributions of 0.1 eV in opposite directions (see Table 3.5). The $\Delta V_{mol.}$ contribution is reduced in the tilted configuration, as the dipole moment component perpendicular to the surface is small due to the molecular orientation. The work function change of the bare Au(111) surface due to geometric relaxations is limited, approximately +0.1 eV. In comparison to metal surfaces, metal oxide surfaces undergo a more significant relaxation of the surface geometry upon molecular sorption. For the monomers on ITO, there is a modification of +0.4 eV. This is consistent with previous results of chemisorbed modifiers, e.g. phosphonic acids on ITO[23] vs. thiols on gold.[28]

The largest component of the overall work function modification is the $\Delta V_{int.dip.}$ term, associated with charge transfer, the "cushion" effect, and/or redistribution at the interface. This contribution is illustrated in Figure 6 for the Cp*-down configuration at MC on the Au(111) surface. There is a large charge redistribution upon bonding, with electron transfer from the monolayer to the metal (see Figure 3.6b for electron density decrease at the monolayer located at ~20 Å from the bottom of the unit cell and electron density increase in the metal at <~18 Å). This is reflected in the sum of the Bader charges, for instance, for the Cp*-down complex when interacting with the MC-gold surface. In this case, 0.42 |e| is transferred from the Cp*-down complex to the surface (see Table 3.6). Interestingly, at this configuration, the Bader charge analysis shows that the electron-loss on the Cp*-ring near the surface is only 0.08|e|; this is only one third of the amount of electron-loss on the Cp-ring (0.21 |e|) that is farther away from the surface. A similar trend is observed for the Cp-down configuration at MC (see Table 3.6), where the electron-loss on the Cp-ring (which is closer to the surface than Cp*) is 0.1 |e| lower than on the Cp*-ring. Such a trend could potentially come from a back-donation of electrons from the gold surface to the monomer complex.

As for the work function modification, there exists a coverage dependence of the charge rearrangement, as the sum of the Bader charges shows that the Cp*-down configuration at HC has a charge transfer of 0.38 |e| and at LC, 0.52 |e|. When the sums of Bader charges are divided by the surface area of the respective unit cells, the Cp*-down configuration has charge transfer of 4.38×10^{-3} |e|/Å^2 at HC, 2.44×10^{-3} |e|/Å^2 at MC, and 1.51×10^{-3} |e|/Å^2 at LC. This shows that even though there is more charge being transferred

per monomer to the surface in the MC and LC cases, the total charge transferred decreases per unit area.

A comparison of the work function modification with respect to packing density reflects the significant depolarization effects that occur in these systems. For the Au(111)-LC Cp*-down system, the Φ decrease is -1.32 eV; in the MC system that has double the monomer density, Φ decreases by -2.52 eV, which is less than the -2.64 eV value expected with no depolarization. The HC-surface has even more depolarization (calculated as -3.44 eV versus -5.28 eV as expected if no depolarization), indicating that further increases in coverage would result in lesser changes to the work function.

For the monomer complex on ITO, an average charge of 0.55 ± 0.02 |e| is transferred. Similar to the MC Au(111) case shown in Figure 3.6b, the overall charge transfer on ITO (see Figure 3.7b) is comprised of a concerted loss of charge density in both Cp rings as well as on the central Ir atom, ultimately leading to a large decrease in the plane-averaged electrostatic potential energy above the modified surface, shown in Figure 3.7c. The conclusion that the interface dipole is the main component of the calculated work function modification is supported by UPS measurements.[5] There is only a small shift in the energy of the valence band maximum of UPS spectra observed after the monomer is added, implying that the bulk of the ΔΦ is caused by a large shift of the vacuum level, resulting from the interface dipole formed between the monomer and the substrate.[5]

Table 3.5: Experimental and calculated work function measurements and calculated work function modification breakdown for the monomers and dimer on gold and monomers on the ITO surface. All calculations have been performed at the PBE-D2 level, unless noted. Values are in eV.

System	Exp. Φ [a]	Calc. Φ	Calc. ΔΦ	$\Delta V_{int.\ dip.}$	$\Delta V_{geom.}$	$\Delta V_{mol.}$
Au(111) HC [b]	5.22 ± 0.03	5.21 / 5.15 [c]	----	----	----	----
Avg. Au(111)+IrCpCp* HC [b]	3.35 ± 0.03	1.49 ± 0.24	-3.72 ± 0.24	-3.66 ± 0.06	-0.05 ± 0.11	0.002 ± 0.19
Au(111) + Cp-down HC [b]		1.37	-3.84	-3.60	0.01	-0.19
Au(111) + Cp*-down HC [b]		1.77	-3.44	-3.68	0.01	0.20
Au(111) + Cp*-down HC [b, c]		1.48	-3.66	-3.96	0.10	0.20
Au(111) + tilted HC [b]		1.34	-3.87	-3.71	-0.17	-0.004
Au(111) MC [d]		5.14	----	----	----	----
Avg. Au(111)+IrCpCp* MC [d]	3.35 ± 0.03	2.62 ± 0.28	-2.52 ± 0.28	-2.55 ± 0.20	0.01 ± 0.10	-0.03 ± 0.12
Au(111) + Cp-down MC [d]		2.60	-2.54	-2.55	0.07	-0.12
Au(111) + Cp*-down MC [d]		2.91	-2.23	-2.36	-0.11	0.11
Au(111) + tilted MC [d]		2.35	-2.79	-2.75	0.07	-0.08
Au(111) LC [e]		5.15	----	----	----	----
Au(111) + Cp*-down LC [e]	3.35 ± 0.03	3.83	-1.32	-1.47	0.06	0.09
ITO(222)	4.63 ± 0.04	3.03	----	----	----	----
Avg. ITO(222)+IrCpCp*	3.29 ± 0.09	1.80 ± 0.08	-1.23 ± 0.08	-1.61 ± 0.05	0.42 ± 0.01	-0.02 ± 0.12
ITO(222) + Cp-down		1.76	-1.27	-1.56	0.42	-0.11
ITO(222) + Cp*-down		1.89	-1.14	-1.65	0.43	0.11
ITO(222) + tilted		1.75	-1.28	-1.62	0.41	-0.07

[a] Reference 5 [b] HC denotes high coverage, or a monomer in the smallest unit cell. [c] Calculations performed at the PBE-D3 level. [d] MC denotes medium coverage, or a monomer in the second largest unit cell [e] LC denotes low coverage, or a monomer in the largest unit cell.

Table 3.6: Bader charges for the components of the isolated monomer and dimer as well as the MC dimer, Cp*-down, Cp-down, and hydrogen abstraction modified Cp*-down configurations on gold. All values in |e|.

System	Total	Ir	Cp ring	Cp* ring
Isolated Cp*-down	0.00	0.34[a]	-0.21[a]	-0.13[a]
Isolated Dimer	0.00	0.39[b]	-0.16[b]	-0.19[b]
Au(111) Ir Cp*-down MC	0.42	0.47	-0.001	-0.05
Au(111) Ir H Abstraction Cp*-down MC	0.04	0.37	-0.22	-0.12
Au(111) Ir Dimer MC	0.19	0.43[c]	-0.09[c]	-0.11[c]
Au(111) Ir Cp-down MC	0.59	0.45	-0.01	0.15

[a] Results for the spin-polarized isolated Cp*-down monomer. [b] Results for the monomer portion with the Cp* ring unbound to the other monomer portion. [c] Results for the monomer portion closest to the gold surface.

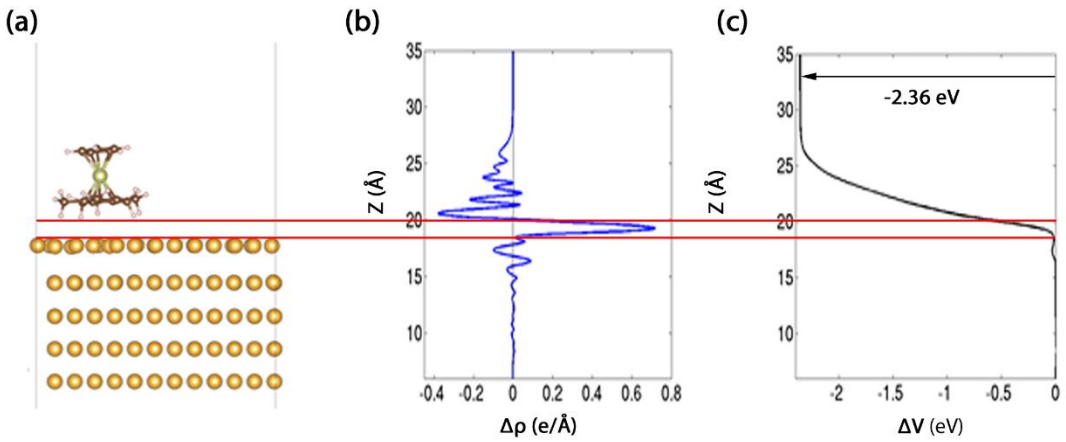

Figure 3.6: Representation of the Cp*-down monomer on the MC Au(111) surface calculated at the PBE-D2 level (a) along with graphs of charge density difference (Δρ) upon IrCpCp* adsorption (b) and the plane-averaged electrostatic potential energy (ΔV) (c). The red lines help to designate the vacuum gap between the top of the surface and the bottom of the monomer. Reprinted with permission from Elsevier.[3]

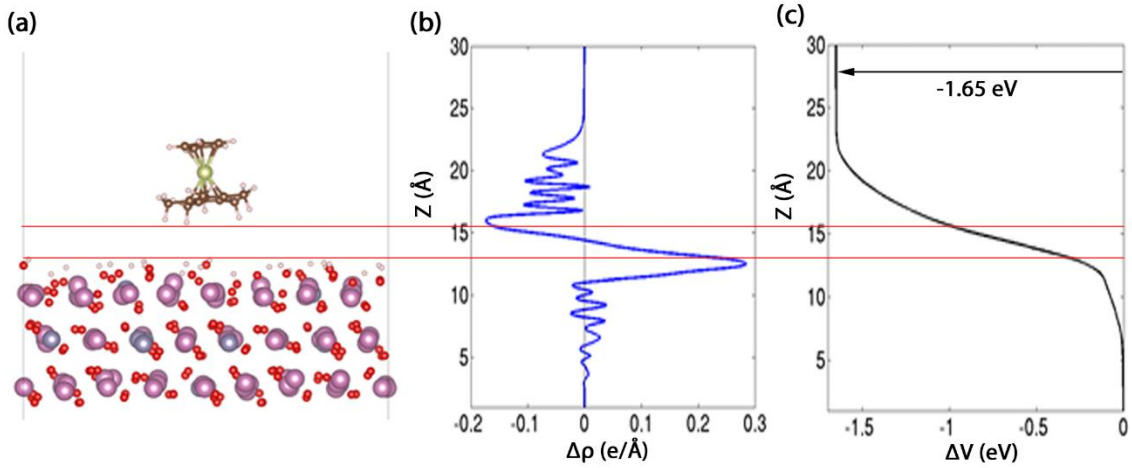

Figure 3.7: Representation of the Cp*-down monomer on the ITO(222) surface calculated at the PBE-D2 level (a) along with graphs of charge density difference (Δρ) upon IrCpCp* adsorption (b) and the plane-averaged electrostatic potential energy (ΔV) (c). The red lines help to designate the vacuum gap between the top of the surface and the bottom of the monomer. Reprinted with permission from Elsevier.[3]

3.3.3 Work Function Modification by Dimer

Table 3.5 demonstrates that the physisorption of monomers leads to large decreases in Φ on both gold and ITO substrates via electron transfer. We now turn to a discussion of changes in Φ that can be observed when the dimer is applied to the surface. There we considered the Au(111) surface. In these calculations, the dimer was placed in the largest gold unit cell (*i.e.*, with the same iridium-to-gold ratio as the monomers in the MC cases), and the configuration of the dimer was taken to be Cp*-down as this is the most stable configuration of the monomers at the MC density. Adsorption of the dimer leads to a ΔΦ of -1.19 eV, a value more than 1.4 eV smaller than if two monomers were deposited on the surface, but only slightly smaller than the value for a single monomer on the LC surface. The $\Delta V_{mol.}$ component, calculated to be 0.22 eV, is almost twice the value for the Cp*-down configuration of the monomer. This result can be rationalized when considering the optimized geometry of the dimer in Figure 3.4d; the two monomer-like components of the dimer are both Cp*-down, with only a slight tilt to the component that is farthest away from the surface, which means that the individual dipole moments are nearly additive. As in the monomer case, the major component to ΔΦ is the interface dipole. The modification of the work function due to this charge rearrangement is -1.44 eV, which is nearly identical to the low coverage monomer value of -1.47 eV. The fragment closest to the surface has a negative charge of 0.22 |e| while the fragment further from the surface remains neutral. Both the geometric features and the charge distribution describe the dimer on the Au surface as two nearly separate monomer moieties: the moiety closest to the surface has undergone a change in hapticity and substantial electron transfer while the second moiety is loosely bound to the cationic moieties on the surface.

3.3.4 Modification of the Monomers

Other molecular species are possible on the surface and can be formed when the central C-C bond in the dimer is cleaved and the 19-electron monomers can further react, for instance, via coupling with other radicals or via hydrogen- or halogen-atom abstraction.[37] Here, we consider a possible reaction where the monomer has abstracted a hydrogen atom from the solvent used during the application of the dopant. In the Cp*-down configuration, this hydrogen atom enforces a η^4-Cp (η^5-Cp*) coordination, with an 18-electron Ir(I) monomer-like structure. In order to determine if the presence of such an Ir(I) complex can alter the work function, we carried out calculations where the Cp or Cp* ring farthest from the surface is modified by adding an extra hydrogen atom. We note that this maintains the non-specific binding of the 19-electron monomer, but acts to prevent electron transfer. On both surfaces, Cp-down and Tilted binding configurations are maintained where the Cp*-down configurations are no longer stable; optimization of the systems from this latter starting point leads to a configuration that resembles the tilted configuration. A representative example of the geometry of a modified complex is illustrated in Figure 3.8 with all of the geometries of the modified complexes shown in Figure 3.9. The $\Delta\Phi$ and $\Delta\Phi$ breakdowns in terms of Equation 1.5 for these modified monomers are shown in Table 3.7. The work function is reduced by 0.95 eV on the Au(111) surface and by 0.03 eV on ITO. Compared with the modifications from the monomers in Table 3.5, these are significantly smaller values. The $\Delta\Phi$ breakdown again shows that for the modified monomers on gold, the majority of the modification continues to be due to the interface dipole, while there is almost no change in Φ from the ITO surface. For the modified monomer on gold, the interface dipole is approximately 0.5 eV smaller than the

corresponding value for the dimer on gold. The limited magnitude of the work function modification here underlines that the electron-transfer process is the defining feature of these dopants; the presence of such modified structures on the surface cannot account for the observed Φ modification.

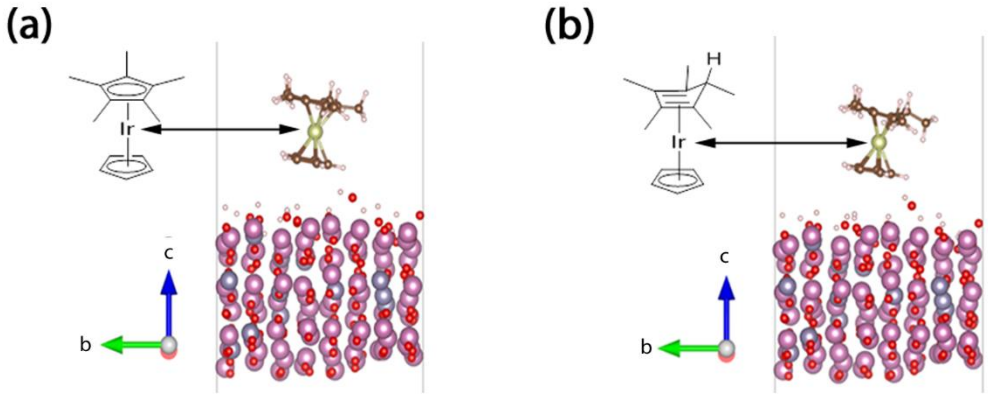

Figure 3.8: Comparison of the geometry of the unmodified Cp-down monomer (a) and the modified Cp-down monomer, with an extra hydrogen atom (b) on the ITO(222) surface. Reprinted with permission from Elsevier.[3]

Table 3.7: Comparison of the ΔΦ and ΔΦ breakdowns of the modified monomers to the unmodified monomers on the gold and ITO surfaces. The monomers on gold are at the medium coverage. All calculations have been performed at the PBE-D2 level. All values in eV.

System	Exp. Φ [a]	Calc. Φ	Calc. ΔΦ	$\Delta V_{int.\ dip.}$	$\Delta V_{geom.}$	$\Delta V_{mol.}$
Au(111)	5.22 ± 0.03	5.14	----	----	----	----
Au(111)+IrCpCp*	3.35 ± 0.03	2.62 ± 0.28	-2.52 ± 0.28	-2.55 ± 0.20	0.01 ± 0.10	-0.03 ± 0.12
Avg. Au(111)+IrCpCp* + H		4.19 ± 0.10	-0.95 ± 0.11	-0.92 ± 0.09	0.06 ± 0.006	-0.01 ± 0.04
Au(111) + Cp-down + H		4.13	-1.01	-1.00	0.05	0.01
Au(111) + Cp*-down + H		4.13	-1.01	-0.94	0.06	-0.06
Au(111) + tilted + H		4.32	-0.82	-0.83	0.06	0.02
ITO(222)	4.63 ± 0.04	3.03	----	----	----	----
ITO(222)+IrCpCp*	3.29 ± 0.09	1.80 ± 0.08	-1.23 ± 0.08	-1.61 ± 0.05	0.42 ± 0.01	-0.02 ± 0.12
Avg. ITO(222)+IrCpCp* + H		3.00 ± 0.03	-0.03 ± 0.03	0.01 ± 0.01	0.003 ± 0.01	-0.02 ± 0.03
ITO(222) + Cp-down + H		2.97	-0.06	0.02	0.01	-0.05
ITO(222) + Cp*-down + H		3.00	-0.03	0.01	-0.01	-0.01
ITO(222) + tilted + H		3.02	-0.01	0.01	0.01	0.01

[a] Reference 5

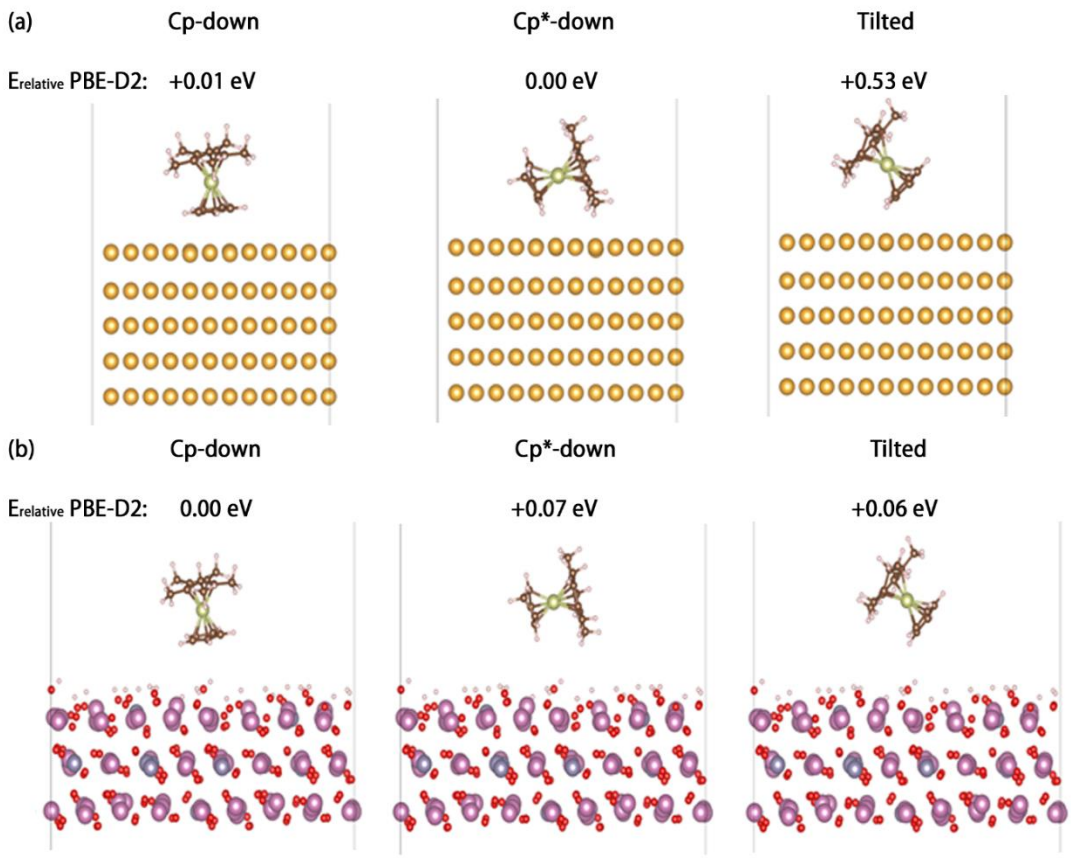

Figure 3.9: Optimized PBE-D2 geometries of the hydrogen-abstracted monomers (a) on the Au(111) surface at medium coverage and (b) on the ITO(222) surface. The relative energies of the hydrogen-abstraction monomer complexes on the surfaces are also given. Reprinted with permission from Elsevier.[3]

3.4 Conclusions

The major factors contributing to the large work function modifications due to IrCpCp* monomers on ITO and gold substrates have been examined using DFT. The calculated Φ reduction caused by deposition of the monomer is ~1.2 eV for the ITO(222) surface and ~1.3 eV for the Au(111) surface at low molecular coverage; it is mainly associated with the contribution of a large interface dipole. Our results are in agreement with the UPS measurements,[5] which has attributed such work function reductions to the

formation of interface dipoles. This interface dipole has a large contribution from charge transfer between the iridium complex and the surface, which only occurs when the central C-C bond of the dimer is cleaved to form the redox-active monomer species. While previous work had only hypothesized that such a charge transfer occurs, our work clearly highlights it on surfaces with different chemistries.

Calculations for the IrCpCp* dimer on the surface show smaller modifications of the surface work function as the C-C bond is only partially cleaved, which limits charge transfer to the surface. This partial cleavage shows that the C-C bond strength and cleavage mechanism are critical parameters determining the ability of the species to donate electrons to the surface. Adding a hydrogen atom to the Cp ring farther from the surface has been shown to reduce the amount of charge transfer, which leads to considerably smaller work function modifications than for the dimer or unmodified monomers.

Overall, the redox-active materials examined in this investigation represent an interesting class of surface modifiers in addition to covalently bound modifiers such as phosphonic acids, thiols, or carboxylic acids. Redox-active dopants are attractive from the standpoint of applications to a broad variety of substrates, compared to other modifiers which require specific chemical reactions to occur between the substrate surface and a binding group. The tradeoff may come in the overall stability of the surface after modification as covalently bound modifiers have been shown to be very stable on the surface.

3.5 References

1. Zhou, Y.; Fuentes-Hernandez, C.; Shim, J.; Meyer, J.; Giordano, A. J.; Li, H.; Winget, P.; Papadopoulos, T.; Cheun, H.; Kim, J.; Fenoll, M.; Dindar, A.; Haske, W.; Najafabadi, E.; Khan, T. M.; Sojoudi, H.; Barlow, S.; Graham, S.; Brédas, J.-L.; Marder, S. R.; Kahn, A.; Kippelen, B. "A Universal Method to Produce Low-Work Function Electrodes for Organic Electronics." *Science* **2012,** *336*, 327-332.

2. Jørgensen, M.; Norrman, K.; Krebs, F. C. "Stability/degradation of polymer solar cells." *Sol. Energy Mater. Sol. Cells* **2008,** *92* (7), 686-714.

3. Hyla, A. S.; Winget, P.; Li, H.; Risko, C.; Brédas, J.-L. "Work function reduction by a redox-active organometallic sandwich complex." *Org. Electron.* **2016,** *37*, 263-270.

4. Paramonov, P. B.; Paniagua, S. A.; Hotchkiss, P. J.; Jones, S. C.; Armstrong, N. R.; Marder, S. R.; Brédas, J.-L. "Theoretical Characterization of the Indium Tin Oxide Surface and of Its Binding Sites for Adsorption of Phosphonic Acid Monolayers." *Chem. Mater.* **2008,** *20*, 5131-5133.

5. Giordano, A. J.; Pulvirenti, F.; Khan, T. M.; Fuentes-Hernandez, C.; Moudgil, K.; Delcamp, J. H.; Kippelen, B.; Barlow, S.; Marder, S. R. "Organometallic Dimers: Application to Work Function Reduction of Conducting Oxides." *ACS Appl. Mater. Interfaces* **2015,** *7* (7), 4320-4326.

6. Owen, E. A.; Yates, E. L. "Precision measurements of crystal parameters." *Philos. Mag.* **1933,** *15* (98), 472-488.

7. Sławińska, J.; Dabrowski, P.; Zasada, I. "Doping of graphene by a Au(111) substrate: Calculation strategy within the local density approximation and a semiempirical van der Waals approach." *Phys. Rev. B* **2011,** *83*, 245429(1-8).

8. Kresse, G.; Furthmüller, J. "Efficiency of ab-inito total energy calculations for metals and semiconductors using a plane-wave basis set." *Comput. Mater. Sci.* **1996,** *6* (1), 15-50.

9. Kresse, G.; Furthmüller, J. "Efficient iterative schemes for ab initio total-energy calculations using a plane-wave basis set." *Phys. Rev. B* **1996,** *54* (16), 11169-11186.

10. Blöchl, P. E. "Projector augmented-wave method." *Phys. Rev. B* **1994,** *50* (24), 17953-17979.

11. Perdew, J. P.; Burke, K.; Ernzerhof, M. "Generalized Gradient Approximation Made Simple." *Phys. Rev. Lett.* **1996,** *77* (18), 3865-3868.

12. Perdew, J. P.; Burke, K.; Ernzerhof, M. "Generalized Gradient Approximation Made Simple [Phys. Rev. Lett. 77, 3865 (1996)] Errata." *Phys. Rev. Lett.* **1997,** *78* (7), 1396.

13. Grimme, S. "Semiempirical GGA-Type Density Functional Constructed with a Long-Range Dispersion Correction." *J. Comput. Chem.* **2006,** *27*, 1787-1799.

14. Ruiz, V. G.; Lu, W.; Zojer, E.; Scheffler, M.; Tkatchenko, A. "Density-Functional Theory with Screened van der Waals Interactions for the Modeling of Hybrid Inorganic-Organic Systems." *Phys. Rev. Lett.* **2012,** *108* (14), 146103(1-5).

15. Winget, P.; Schirra, L. K.; Cornil, D.; Li, H.; Coropceanu, V.; Ndione, P. F.; Sigdel, A. K.; Ginley, D. S.; Berry, J. J.; Shim, J.; Kim, H.; Kippelen, B.; Brédas, J.-L.; Monti, O. L. A. "Defect-Driven Interfacial Electronic Structures at an Organic/Metal-Oxide Semiconductor Heterojunction." *Adv. Mater.* **2014,** *26* (27), 4711-4716.

16. Gruenewald, M.; Schirra, L. K.; Winget, P.; Kozlik, M.; Ndione, P. F.; Sigdel, A. K.; Berry, J. J.; Forker, R.; Brédas, J.-L.; Fritz, T.; Monti, O. L. A. "Integer Charge Transfer and Hybridization at an Organic Semiconductor/Conductive Oxide Interface." *J. Phys. Chem. C* **2015,** *119* (9), 4865-4873.

17. Schulz, P.; Kelly, L. L.; Winget, P.; Li, H.; Kim, H.; Ndione, P. F.; Sigdel, A. K.; Berry, J. J.; Graham, S.; Brédas, J.-L.; Kahn, A.; Monti, O. L. A. "Tailoring Electron-Transfer Barriers for Zinc Oxide/C_{60} Fullerene Interfaces." *Adv. Funct. Mater.* **2014,** *24* (46), 7381-7389.

18. Li, H.; Winget, P.; Brédas, J.-L. "Surface Modification of Indium-Tin-Oxide Via Self-Assembly of a Donor-Acceptor Complex: A Density Functional Theory Study." *Adv. Mater.* **2012,** *24*, 687-693.

19. Methfessel, M.; Paxton, A. T. "High-precision sampling for Brillouin-zone integration in metals." *Phys. Rev. B* **1989,** *40* (6), 3616-3621.

20. Tang, W.; Sanville, E.; Henkelman, G. "A grid-based Bader analysis algorithm without lattice bias." *J. Phys.: Condens. Matter* **2009,** *21*, 084204(1-7).

21. Jacquemin, D.; Tanqui;, L. B.; Adamo, C.; Ciofini, I. "What is the "best" atomic charge model to describe through-space charge-transfer excitations?" *Phys. Chem. Chem. Phys.* **2012,** *14* (16), 5383-5388.

22. Li, H.; Duan, Y.; Coropceanu, V.; Brédas, J.-L. "Electronic structure of the pentacene-gold interface: A density-functional theory study." *Org. Electron.* **2009,** *10*, 1571-1578.

23. Li, H.; Paramonov, P. B.; Brédas, J.-L. "Theoretical study of the surface modification of indium tin oxide with trifluorophenyl phosphonic acid molecules: impact of coverage density and binding geometry." *J. Mater. Chem.* **2010,** *20*, 2630-2637.

24. Mohapatra, S. K.; Fonari, A.; Risko, C.; Yesudas, K.; Moudgil, K.; Delcamp, J. H.; Timofeeva, T. V.; Brédas, J.-L.; Marder, S. R.; Barlow, S. "Dimers of Nineteen-Electron Sandwich Compounds: Crystal and Electronic Structures, and Comparison of Reducing Strengths." *Chem. - Eur. J.* **2014,** *20*, 15385-15394.

25. Li, F.; Zhou, Y.; Zhang, F.; Liu, X.; Zhan, Y.; Fahlman, M. "Tuning Work Function of Noble Metals As Promising Cathodes in Organic Electronic Devices." *Chem. Mater.* **2009,** *21*, 2798-2802.

26. Fenwick, O.; Van Dyck, C.; Murugavel, K.; Cornil, D.; Reinders, F.; Haar, S.; Mayor, M.; Cornil, J.; Samorì, P. "Modulating the charge injection in organic field-effect transistors: fluorinated oligophenyl self-assembled monolayers for high work function electrodes." *J. Mater. Chem. C* **2015,** *3* (13), 3007-3015.

27. Li, H.; Duan, Y.; Paramonov, P. B.; Coropceanu, V.; Brédas, J.-L. "Electronic structure of self-assembled (fluoro)methylthiol monolayers on the Au(111) surface: Impact of fluorination and coverage density." *J. Electron Spectrosc. Relat. Phenom.* **2009,** *174*, 70-77.

28. Cornil, D.; Cornil, J. "Work-function modification of the (111) gold surface upon deposition of self-assembled monolayers based on alkanethiol derivatives." *J. Electron Spectrosc. Relat. Phenom.* **2013,** *189*, 32-38.

29. Zhou, Y.; Shim, J. W.; Fuentes-Hernandez, C.; Sharma, A.; Knauer, K. A.; Giordano, A. J.; Marder, S. R.; Kippelen, B. "Direct correlation between work function of indium-tin-oxide electrodes and solar cell performance influenced by ultraviolet irradiation and air exposure." *Phys. Chem. Chem. Phys.* **2012,** *14*, 12014-12021.

30. Sugiyama, K.; Ishii, H.; Ouchi, Y.; Seki, K. "Dependence of indium-tin-oxide work function on surface cleaning method as studied by ultraviolet and x-ray photoemission spectroscopies." *J. Appl. Phys.* **2000,** *87* (1), 295-298.

31. Helander, M. G.; Wang, Z. B.; Qiu, J.; Greiner, M. T.; Puzzo, D. P.; Liu, Z. W.; Lu, Z. H. "Chlorinated Indium Tin Oxide Electrodes with High Work Function for Organic Device Compatibility." *Science* **2011,** *332*, 944-947.

32. Li, H.; Winget, P.; Brédas, J.-L. "Transparent Conducting Oxides of Relevance to Organic Electronics: Electronic Structures of Their Interfaces with Organic Layers." *Chem. Mater.* **2014,** *26* (1), 631-646.

33. Hotchkiss, P. J.; Li, H.; Paramonov, P. B.; Paniagua, S. A.; Jones, S. C.; Armstrong, N. R.; Brédas, J.-L.; Marder, S. R. "Modification of the Surface Properties of Indium Tin Oxide with Benzylphosphonic Acids: A Joint Experimental and Theoretical Study." *Adv. Mater.* **2009,** *21*, 4496-4501.

34. Grimme, S.; Antony, J.; Ehrlich, S.; Krieg, H. "A consistent and accurate ab initio parametrization of density functional dispersion correction (DFT-D) for the 94 elements H-Pu." *J. Chem. Phys.* **2010,** *132*, 154104(1-19).

35. Heimel, G.; Romaner, L.; Zojer, E.; Brédas, J.-L. "Toward Control of the Metal-Organic Interfacial Electronic Structure in Molecular Electronics: A First-Principles Study on Self-Assembled Monolayers of Pi-Conjugated Molecules on Noble Metals." *Nano Lett.* **2007,** *7* (4), 932-940.

36. Heimel, G.; Romaner, L.; Zojer, E.; Brédas, J.-L. "The Interface Energetics of Self-Assembled Monolayers on Metals." *Acc. Chem. Res.* **2008,** *41* (6), 721-729.

37. Astruc, D. "Nineteen-Electron Complexes and Their Role in Organometallic Mechanisms " *Chem. Rev.* **1988,** *88*, 1189-1216.

CHAPTER 4

WORK-FUNCTION REDUCTION OF GOLD BY N-HETEROCYCLIC CARBENES

4.1 Introduction

We now turn to a different way to lower the work function of electrode materials, namely, employing N-heterocyclic carbenes with varying heterocyclic core and substituent structures. Gold has a high WF (ca. 5.2 eV for clean surfaces) and is widely used for electronics applications due to its conductivity and excellent stability in a variety of chemical environments. Its WF can be significantly lowered by the use of molecular reductants that, when deposited on gold from either solution or vacuum, give rise to a surface dipole through electron transfer to the gold, as mentioned in Section 1.2.4.2.3. Another method to significantly lower the WF of Au described in Section 1.2.4.2.3 is the use of polyethyleneimine (PEI) or its ethoxylated derivative (PEIE), which are only processable from solution; a WF of 3.4 eV was measured using UPS for PEIE-treated gold, whereas either polymer affords WFs of ca. 3.9 eV as measured by KP *in air*.[1] This WF reduction is thought to originate from both the dipole resulting from coordination of multiple amine groups in the polymer to the surface and the resulting alignment of the C—N bonds in the polymer and their dipoles. In contrast to most of the reductants and

reductant-treated gold surfaces mentioned above, both the polymers and the modified surfaces are stable in air; on the other hand, the exact composition on the surface is challenging to determine, layers are not necessarily of uniform thickness, and the water present in the commercially available reagents may adversely affect stability for some applications.

Self-assembled monolayers (SAMs) are yet another class of surface modifiers that can be used to lower WF, as mentioned in Section 1.2.4.2.2. Thiolate-based SAMs offer the possibility of combining WF reduction with other properties through synthetic thiol chemistry, but are thermally and oxidatively unstable.[2-3]

N-Heterocyclic carbenes (NHCs) have been widely used as ligands in transition-metal chemistry,[4-8] and have increasingly been used as ligands for gold nanoparticles.[9-11] In the past few years, they have been used as SAM-forming modifiers on planar surfaces of various metals,[9] including gold.[12-14] Many precursor salts and free NHCs are commercially available or can be obtained through fairly simple synthetic procedures.[15] The ligand characteristics of NHC can be altered through saturation/unsaturation and variation of ring size,[16] whereas additional characteristics can be imparted through derivatization of their backbones, for example, NHC SAMs on Au have been functionalized by "click" chemistry using azide functionalities,[12] and through initiation of ring-opening metathesis polymerization from pendant alkene moieties.[14] Crudden *et al.* demonstrated that NHCs on Au are more stable than thiolate-based SAMs; monolayers of dodecyl thiolate were partially displaced by **iPr$_2$bimy** (see Figure 4.1 below) through immersion in a solution of the latter, but dodecanethiol was unable to displace **iPr$_2$bimy**.[12] In addition, NHC SAMs are found to be resistant to boiling water, organic solvents, alkaline

and acidic environments, electrochemical oxidation and reduction, and 1% H_2O_2.[12] The increased stability was attributed to the greater binding energy of NHC-Au (ca. 150 kJ mol^{-1} according to DFT-PBEsol calculations for **iPr₂bimy**)[12] compared with thiolate-Au (ca. 125 kJ mol^{-1}).[17-18] Although these studies addressed the packing order, ability to graft polymers, and thermal and chemical stability of NHC SAMs on gold surfaces, the effect of NHCs on the WF of Au has not, to the best of our knowledge, been studied experimentally. A recent DFT study, however, has suggested the WF of Au modified with 4-(adamantan-1-yl)-1,3-dihydro-2*H*-imidazol-2-ylidene or its *N,N′*-diisopropyl analogue would be ca. 3.8 eV.[19]

Here, in conjunction with an experimental investigation of the effect of a series of NHCs (see Figure 4.1) on the WF of planar Au surfaces in which values as low as 3.3 eV are measured with UPS, DFT calculations are used to gain insight into the mechanism of the WF reduction. A specific objective is to understand the differences between NHCs with relatively small (isopropyl, iPr) and bulky (2,6-diisopropylphenyl, Dipp) *N,N′*-substituents. Experimental collaborators have also demonstrated that single-layer diodes with **SIDipp**-modified Au are more effective electron-injecting contacts towards C_{60} than bare gold. The work in this Chapter has been submitted for publication.

4.2 Experimental Section

4.2.1 NHC Synthesis

NHCs were synthesized by Chelsea Wyss and Abraham Jordan of the Sadighi group at Georgia Tech, and Hye Kyung Kim of the Marder Group at Georgia Tech. 1,3-Diisopropyl-1,3-dihydro-2*H*-benzo[*d*]imidazol-2-ylidene (**iPr₂bimy**),[12, 20] 1,3-

diisopropyl-1,3-dihydro-2*H*-imidazol-2-ylidene (**IiPr**),[21] and 1,3-bis(2,6-diisopropylphenyl)-1,3-dihydro-2*H*-imidazol-2-ylidene (**IDipp**)[22-23] were synthesized according to the literature. 1,3-Bis(2,6-diisopropylphenyl)imidazolidin-2-ylidene (**SIDipp**) was purchased from Sigma Aldrich. 1,3-Bis(2,6-diisopropylphenyl)tetrahydropyrimidin-2(1*H*)-ylidene (**6Dipp**) was synthesized according to adapted literature procedure, using NaHMDS instead of LiHMDS (HMDS = $(Me_3Si)_2N$).[24]

4.2.2 Surface Cleaning and Modification

All surface cleaning and modification was performed by Hye Kyung Kim of the Marder group at Georgia Tech. Commercially available Glass:Ti:Au slides (EMF Corporation, Ithaca, NY) were cut into 0.5" × 0.5" squares and sonicated in ethanol for 10 min, dried under a flow of nitrogen, and etched with oxygen plasma with a PE-50 XL Plasma System for 5 min prior to any additional surface treatment. Samples were transferred into a nitrogen-filled glove box for modification because both the free NHC and modified surfaces are air-sensitive. Surfaces were immersed in 2 mM solutions of the free NHCs in freeze−pump−thaw deoxygenated tetrahydrofuran (THF) for 24 h, then were rinsed with fresh THF (3 × 1 mL), and dried under a flow of nitrogen. Samples were immediately taken for XPS and UPS analysis using a Kratos air-sensitive transporter.

4.2.3 Surface Characterization

All UPS and XPS measurements were conducted by Hye Kyung Kim of the Marder group at Georgia Tech in a Kratos Axis Ultra spectrometer with an average base pressure

of 10^{-9} Torr. UPS spectra were collected prior to XPS spectra with a 21.2 eV He (I) excitation and a pass energy of 5 eV using a 27 μm spot size. XPS spectra were collected at a normal take off angle with a monochromatic Al Kα source using a 400 μm spot size and a pass energy of 160 eV for survey acquisition and 20 eV for high-resolution spectra. The binding energies of all XPS spectra were calibrated and normalized to the Au 4f line at 84.0 eV.

Kelvin-Probe WF data were obtained by Felipe Larrain and Canek Fuentes-Hernandez of the Kippelen group at Georgia Tech and Hye Kyung Kim of the Marder group at Georgia Tech, using a Besocke Delta Phi Kelvin Probe system in a nitrogen atmosphere. The measurements were calibrated to a freshly cleaved highly ordered pyrolytic graphite sample with a known work function of 4.50 eV.[25] All XPS, UPS, and KP data points represent multiple samples scanned on multiple spots.

4.2.4 Calculation Methodology

To describe the Au(111) surface, we used a repeated-slab approach, as described in Section 3.2. We note here that the lattice parameters optimized at the DFT level with the PBE-D3 functional for bulk gold are very close to the experimental values.[26] When one NHC molecule is in the unit cell, the molecular coverage is 5.81×10^{13} molecules cm^{-2}. The slabs are separated by a vacuum space larger than 20 Å.

As described in Section 3.2, all surface calculations were carried out using the Vienna Ab Initio Simulation Package (VASP).[27-28] We chose the generalized gradient approximation (GGA) exchange-correlation functional of Perdew, Burke, and Ernzerhof (PBE),[29-30] augmented by the empirical D3 dispersion correction of Grimme[31] in order to

describe the non-specific interactions of the NHCs with the metal surface. The D3 correction includes three-body non-additivity terms, dispersion parameters that are system independent, and provides similar or better accuracy for "light" molecules and a strongly improved description of metallic and "heavier" systems than the D2 correction.[31] As will be shown below, the difference in work function between the same bare gold surface calculated with PBE-D2 versus PBE-D3 is only 0.03 eV. While PBE-D3 has deficiencies in describing reaction energies and geometries relative to more computationally-intensive methods,[32] the PBE functional has been used to qualitatively describe charge-transfer systems, as described in Section 3.2. In order to examine the extent of charge transfer in these NHC systems, Bader charges were evaluated.[33] The k-point grid, occupation scheme, and smearing value are the same as the IrCpCp* work on MC gold presented in Section 3.2. Geometry optimizations and compensation for possible dipole-dipole interactions between the asymmetric slabs were the same as presented in Section 3.2. WFs (Φ) were calculated using Equation 1.2, where $V_{vac.}$ is the plane-averaged electrostatic potential energy of an electron in the vacuum region away from the slab, at a distance sufficiently far away that the potential energy has reached its asymptotic value, and where E_F denotes the Fermi level energy of the system.

Gas-phase calculations of the carbenes were performed in the Gaussian 09 program suite.[34] The carbene geometries were optimized and frequencies were calculated at the PBE/cc-pVTZ level.[35]

4.2.5 Electrical Measurements

Device preparation and electrical measurements were performed by Felipe Larrain and Canek Fuentes-Hernandez of the Kippelen group at Georgia Tech and Hye Kyung Kim of the Marder group at Georgia Tech. Glass substrates 1" × 1" were cleaned in sequential ultrasonic baths of deionized water, acetone, and isopropanol (each for 30 min at 30 °C). The Au bottom electrode (150 nm) was evaporated onto half of the glass substrates (with a mask) using a SPECTROS (Kurt J. Lesker) thermal evaporator with substrate rotation. For comparison, devices incorporating Au electrodes modified with PEIE were fabricated: PEIE solution (Sigma-Aldrich, 80% ethoxylated, Mw = 70 000 g mol^{-1}, 35−40 wt % in water) was diluted to a concentration of 0.4 wt % and stirred for 12 h prior to use. The solution was dispensed onto the patterned Au substrates through PTFE filters and then spin-coated at 5000 rpm for 60 s. The spin-coated samples were then annealed at 100°C for 10 min in air. NHC modifications were carried out in the glovebox and transferred to the vacuum thermal evaporation system. The vacuum chamber was pumped down to a base pressure of 8.0×10^{-8} Torr. C_{60} (100 nm), MoO_3 (10 nm), and Ag (150 nm) were deposited sequentially through two different shadow masks on the unmodified, PEIE-modified, or NHC-modified Au substrates, to complete the fabrication of organic diodes. The effective area of the diodes was 10.36 mm^2. Current density−voltage ($J-V$) curves were measured in a nitrogen-filled glovebox by using a Keithley 2400 source meter controlled by a LabVIEW program.

4.3 Results and Discussion

4.3.1 NHCs Examined

Figure 4.1 shows the NHCs considered in this study; all six compounds were studied computationally and all except SIiPr were examined experimentally. We were interested in the effect of: (i) the bulk of the *N*,*N*′-substituents, which might be expected to affect the ability of the carbene lone pair to interact with the Au surface; and (ii) the nature of the NHC backbone, which, for a given substituent, is expected to affect the N—C—N bond angle and, thus, the basicity of the NHC lone pair.[16] We note that **iPr$_2$bimy** and **IDipp** were among the examples used to modify Au by Crudden *et al.*.[12] In the figure, the NHCs used are arranged into columns according to the *N*,*N*′-substituents, and, within each column, are ordered according to expected N—C—N bond angle.

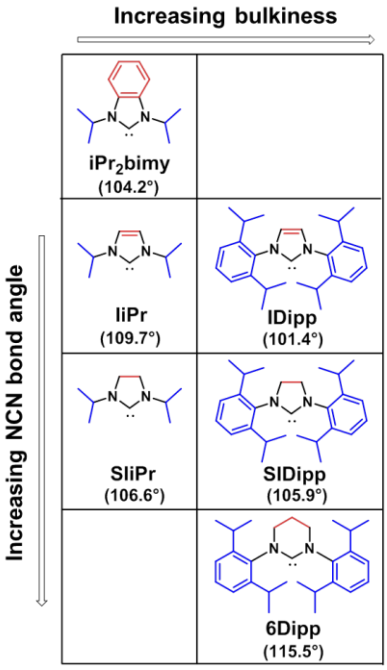

Figure 4.1: Chemical structures of NHCs used in this work to reduce the WF of Au surfaces; red (backbone) and blue (substituents) colored for emphasis. N—C—N bond angles are from gas-phase PBE/cc-pVTZ calculations. Note that the bond-angle difference between **IiPr** and **SIiPr** does not follow the expected trend. (See Table 4.1 for N—C—N bond angles for NHCs bound to gold).

Table 4.1: Calculated N-C-N Bond Angles (°) for Isolated NHCs Molecules[a] and After Interacting with Au(111).

NHC	Isolated Carbene	Carbene on Gold
iPr$_2$bimy	104.2	106.4
IiPr	109.7	104.5
SIiPr	106.6	108.8
IDipp	101.4	101.5
SIDipp	105.9	105.9
6Dipp	115.5	116.1

[a] The calculations for the isolated molecules were performed with Gaussian 09[34] at the PBE/cc-pVTZ level.

4.3.2 XPS Characterization and Molecular Coverage

Since the NHCs have substituents with varying degrees of steric bulk and orientation with respect to the surface, the absolute molecular coverage may vary among the different modified surfaces. Coverage has been shown to play a significant role in the WF modification ability of a surface modifier.[36-37] Plasma-treated Au surfaces were modified under inert atmosphere by dipping in 2 mM THF solutions of the NHC for 24 h and then the surface composition of the samples was investigated using XPS by Hye Kyung Kim of the Marder group at Georgia Tech. N 1s ionizations are observed for the modified surfaces at binding energies of ca. 400-402 eV, consistent with other reports of NHCs on planar gold,[9, 13-14] and with NHC adhering to the surface. Moreover, the intensity of the N 1s signal (and the N 1s / Au 4f intensity ratio) indicates that the smaller NHCs (a-b) more densely cover the surface than the larger ones (c-e) (see Figure 4.2).

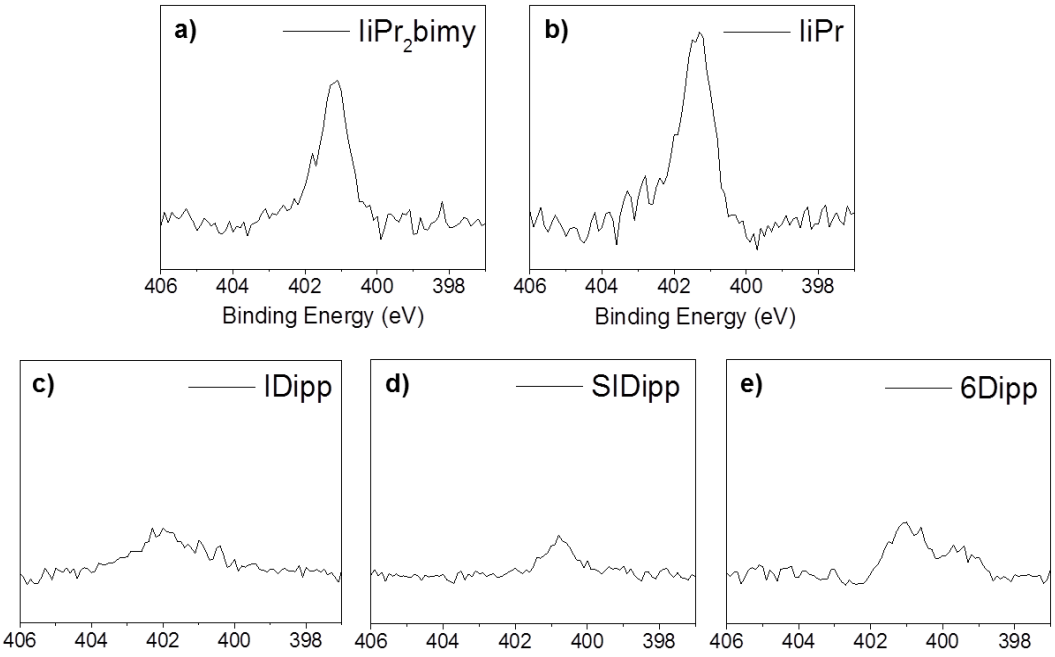

Figure 4.2: Representative XPS N 1s spectra for NHCs on Au. XPS Spectra courtesy of Hye Kyung Kim of the Marder Group at Georgia Tech.

Table 4.2 summarizes the molecular footprint for each geometry-optimized NHC in the calculations, the ideal absolute close-packed, non-interacting coverage value (in molecules cm^{-2}) from the calculated footprint (Figure 4.3a), the experimental absolute coverage as estimated from XPS N/Au ratios, and the percentage ideal monolayer values obtained from the comparison of experimental coverage compared to those calculated for a full monolayer. As in the experimental data, the calculated molecular footprints suggest the coverage attainable should depend on the *N,N′*-substituents, with the bulkier NHCs with bis(2,6-diisopropylphenyl) substituents being present at one half to one third the coverage of the diisopropyl-substituted NHCs. The results also show that the experimental estimated coverages are rather close to that estimated for complete monolayers at 89-121% and track

fairly linearly (Figure 4.3b). This suggests that the NHCs are tightly packed and, therefore, leave little room for contaminants to interact with the surface.

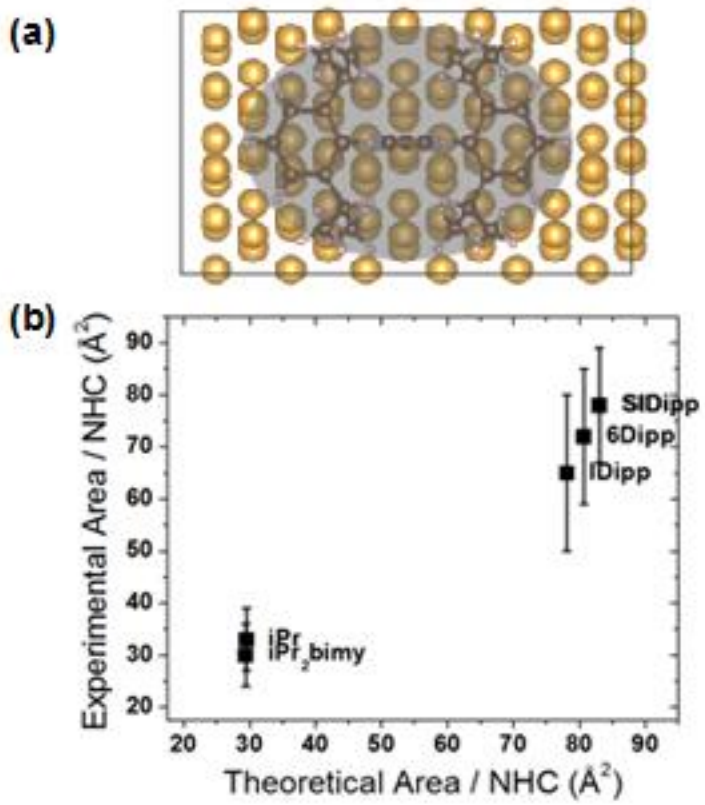

Figure 4.3: Representative footprint of an NHC (IDipp) on a Au(111) surface from DFT calculations (a) and plot of experimental vs. calculated footprints (b). Experimental data courtesy of Hye Kyung Kim of the Marder group at Georgia Tech.

Table 4.2: Calculated and Experimental Footprints and Coverages for NHCs on Gold.

	Footprint / Å^2		Coverage / 10^{14} molecule cm^{-2}		% Ideal
NHC	**Calc.**	**Exp.**[a]	**Ideal**[b]	**Exp.**[c]	**Monolayer**[d]
iPr$_2$bimy	29.4	30 ± 6	3.40	3.3 ± 0.6	99
IiPr	29.5	33 ± 6	3.39	3.0 ± 0.5	89
SIiPr	29.5	*e*	3.39	*e*	*e*
IDipp	78.1	65 ± 15	1.28	1.5 ± 0.3	121
SIDipp	83.0	78 ± 11	1.21	1.3 ± 0.2	106
6Dipp	80.7	72 ± 13	1.24	1.4 ± 0.3	112

[a] The experimental footprint given is the reciprocal of the coverage. [b] Estimated as the reciprocal of the calculated footprint. Note that the footprint (Figure 4.3a) is based on an ellipse, which cannot be tessellated to fully cover the surface; however, this overlooks the possibility of overlap of the substituents of neighboring ellipses through interlocking of alkyl substituents. [c] Experimental average coverage estimated from XPS data as described in the Supporting Information; the error bars are estimated based on spot-to-spot variation of XPS peaks, but do not take into account approximations made in converting XPS ratios to atomic ratios. [d] Percentage ideal monolayer given by 100% × experimental coverage / ideal coverage. [e] Not measured. Experimental data courtesy of Hye Kyung Kim of the Marder group at Georgia Tech.

4.3.3 UPS Characterization and Work-Function Modification

The WFs of bare and NHC-modified Au were measured using UPS in vacuum, by Hye Kyung Kim of the Marder group at Georgia Tech, as well as using KP under nitrogen in ambient pressure conditions, by Felipe Larrain and Canek Fuentes-Hernandez of the Kippelen group at Georgia Tech and Hye Kyung Kim of the Marder group. Both measurement techniques indicate large WF reductions after NHC modification (Table 4.3, Figure 4.4, Figure 4.5), with UPS indicating WF values of ca. 3.3-3.5 eV and KP values of ca. 3.8-4.0 eV for all the NHCs examined; these WF reductions are larger than those typically obtained using alkanethiolates,[38-40] and comparable to those obtained using PEI or PEIE,[1] or solution doping with $(IrCp^*Cp)_2$.[41] Exposure to air for 24 h leads to an increase in WF; this is not surprising since low-WF surfaces, including intrinsically low-WF metals and dimer-doped ITO and Au,[41-42] but notably not PEI- and PEIE-modified substrates,[1] are often air sensitive, presumably due to electron transfer to atmospheric O_2 and/or water, and

since free NHCs are also oxidized in air.[43] However, even after 24 h exposure to air, the WF values obtained were ca. 4.0 eV according to UPS, *i.e.* comparable to values for alkanethiolate-modified gold in inert atmosphere[38-40] (see Table 4.4, Figure 4.7). On the other hand, the WFs (tested for **IDipp**, **SIDipp**, and **6Dipp**) showed only slight increases over 2-7 days of storage in a N_2-filled glovebox (see Figure 4.6).

Table 4.3: Experimental and Calculated Work-Functions for Gold Surfaces[a] Modified with NHCs. All units are in eV.

	UPS		Kelvin Probe		DFT				
NHC	**Φ**	**ΔΦ**[b]	**Φ**	**ΔΦ**[b]	**Φ**	**ΔΦ**[b]	**Δ$V_{int.\ dip.}$**[c]	**Δ$V_{geom.}$**[c]	**Δ$V_{mol.}$**[c]
none	5.17 ± 0.13	----	5.07 ± 0.11	----	5.17	----	----	----	----
iPr$_2$bimy	3.41 ± 0.04	–1.76 ± 0.14	3.98 ± 0.11	–1.09 ± 0.16	3.90	–1.27	–1.00	0.01	–0.27
IiPr	3.29 ± 0.08	–1.88 ± 0.15	3.73 ± 0.12	–1.34 ± 0.18	3.84	–1.33	–0.88	0.01	–0.44
SIiPr	*d*	*d*	*d*	*d*	3.77	–1.40	–0.90	0.01	–0.51
IDipp	3.30 ± 0.18	–1.87 ± 0.22	3.81 ± 0.17	–1.26 ± 0.20	4.13	–1.04	–0.54	0.01	–0.48
SIDipp	3.52 ± 0.07	–1.65 ± 0.18	3.95 ± 0.15	–1.12 ± 0.19	4.23	–0.94	–0.43	0.01	–0.50
6Dipp	3.42 ± 0.14	–1.75 ± 0.19	3.85 ± 0.12	–1.22 ± 0.18	4.11	–1.06	–0.47	0.01	–0.56

[a] UPS and KP data acquired at the coverages given in Table 4.2; DFT values calculated at a constant coverage of 5.81×10^{13} molecules cm^{-2}. [b] $\Delta\Phi = \Phi_{(mod.\ Au)} - \Phi_{(bare\ Au)}$. [c] See Equation 1.5 and text for definitions. [d] Not measured.

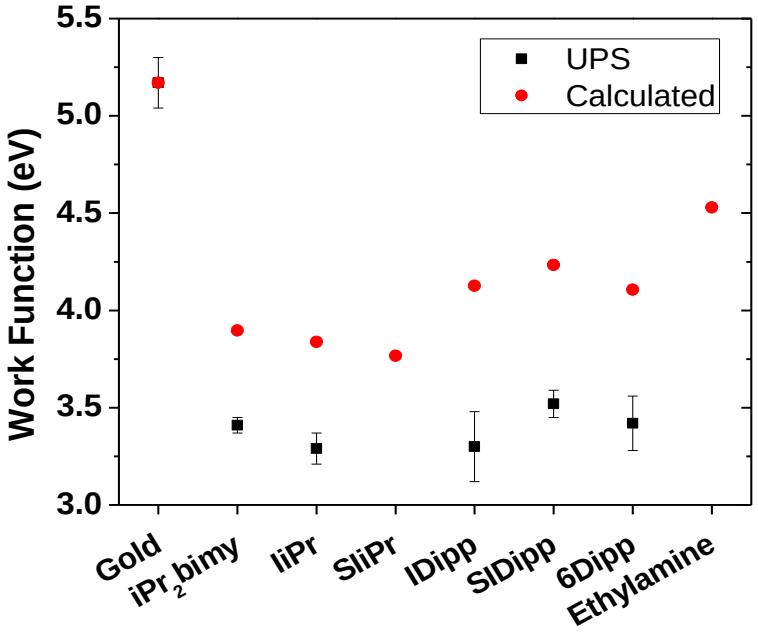

Figure 4.4: Plot showing experimental (UPS) and calculated work functions for bare and NHC-modified Au surfaces. The error bars are the standard deviations of samples over different surfaces. UPS data courtesy of Hye Kyung Kim of the Marder group at Georgia Tech.

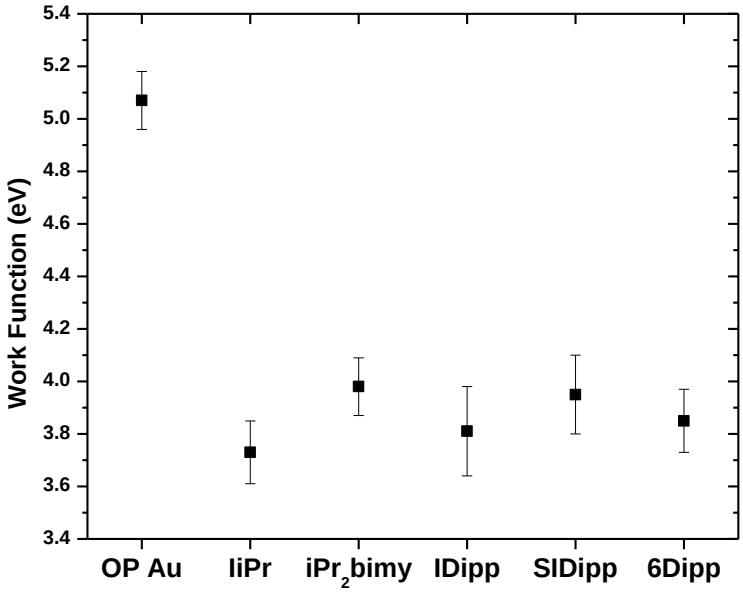

Figure 4.5: Work function values measured by Kelvin Probe under nitrogen for unmodified and NHC-modified Au substrates (modified using same procedure as UPS samples, as described in the experimental section). KP data courtesy of Felipe Larrain and Canek Fuentes-Hernandez of the Kippelen group at Georgia Tech and Hye Kyung Kim of the Marder group.

Table 4.4: Work Function Values (in eV) of NHC-Modified Surfaces after 24 h Exposed to Ambient Conditions and Measured Using UPS.

NHC	Φ after air exposure	$\Phi_{air} - \Phi_{init}$[a]
iPr$_2$bimy	3.94 ± 0.07	0.53 ± 0.17
IiPr	3.80 ± 0.13	0.51 ± 0.15
IDipp	3.94 ± 0.08	0.64 ± 0.26
SIDipp	3.97 ± 0.02	0.45 ± 0.09
	4.00 ± 0.07[b]	
6Dipp	3.95 ± 0.16	0.53 ± 0.30

[a] Difference between WF value measured before exposure to air (from Table 4.3 **Table 4.3**) and that measured after 24 h exposure. [b] After 4 min. exposure to ambient conditions. UPS data courtesy of Hye Kyung Kim of the Marder group at Georgia Tech.

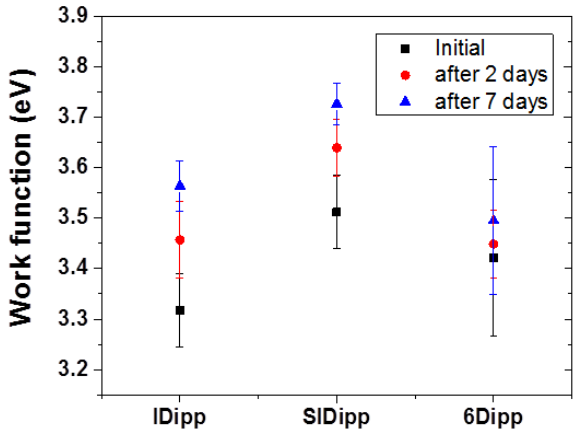

Figure 4.6: WF retention test (using UPS) after 2 days and 7 days of storage under nitrogen gas. UPS data courtesy of Hye Kyung Kim of the Marder group at Georgia Tech.

Figure 4.4 also shows DFT values of the WF for both bare and NHC-modified Au (at a constant coverage of 5.81×10^{13} molecules cm^{-2}). The WF of the bare Au(111) surface was calculated to be 5.17 eV, in excellent agreement with the UPS results obtained here and previous values obtained by experiments and calculations in the literature.[41, 44-48] The DFT-calculated WF values for the NHC-modified surfaces are somewhat larger than the experimental values, which is likely, at least partly, due to the lower coverage used in the calculations; however they are consistent with experiment in that they show that all NHCs

examined give large WF reductions. Both experimental (UPS and KP) and DFT WF values vary little with the structure of the heterocyclic core for a given *N,N′*-substitution pattern. On the other hand, the calculations suggest that, at equal coverage, the bulkier bis(diisopropylphenyl) species should lead to smaller WF reductions than their diisopropyl analogues, whereas experimentally (where the bulkier examples exhibit lower coverages) little difference is seen. ($\Delta\Phi$ arises from the interplay of contributions to $\Delta V_{\text{int.dip.}}$ from C_{carbene}—Au bonding, the "cushion" effect, and other charge reorganization, and of $\Delta V_{\text{mol.}}$, the relative importance of these evidently varies between different NHCs. The discrepancy whereby DFT values $\Delta\Phi$ are lower for Dipp than iPr species, but experimental values are similar, may result from limitations in quantitatively reproducing some of these contributions, but may also result from different dependencies of these different contributions on coverage.)

Table 4.3 Table 4.3 also decomposes the contributions to the work-function reduction, $\Delta\Phi$, of the NHC-modified Au using Equation 1.5 which was discussed extensively in our previous work,[37, 49] where $\Delta V_{\text{int.dip.}}$ is the contribution of the dipole formed at the immediate interface between molecular layer and surface due to charge redistribution; $\Delta V_{\text{mol.}}$ is the electrostatic potential energy change across an isolated molecular layer in vacuum; and $\Delta V_{\text{geom.}}$ is the WF change of the bare surface due to the geometric relaxations that take place when interacting with the NHC molecules. The variation in these quantities is discussed in more detail in the following Section. Figure 4.4 also includes as a model for PEI- and PEI(E)-modified Au,[1] the DFT-calculated WF for Au modified with $EtNH_2$ at the same coverage as the NHCs; this suggests that the WF reduction *per modifier molecule* is larger for NHCs than that for the amine (of course, it

must be borne in mind that the density of amines in PEI- or PEI(E)-modified Au is potentially much higher than that of NHCs in the monolayers studied here).

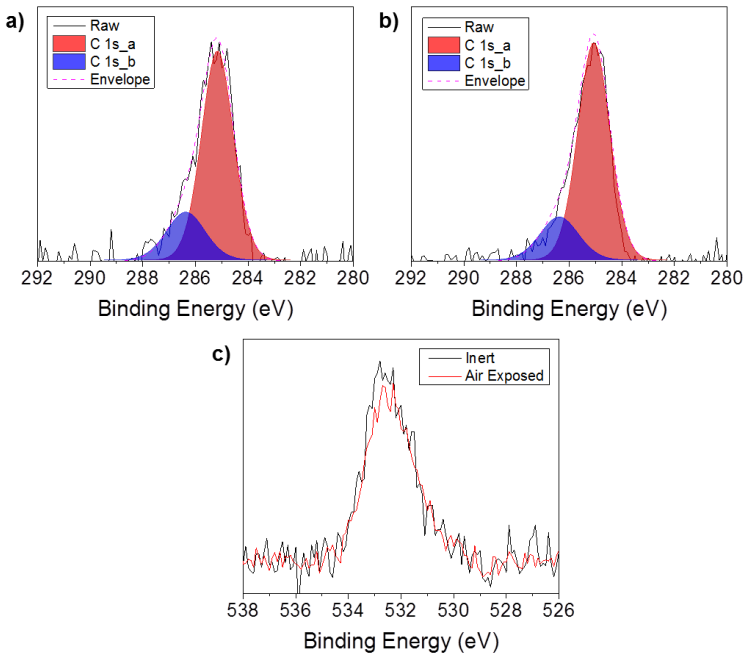

Figure 4.7: XPS spectra of the C 1s peak components for IiPr on Au a) after storage under inert conditions and b) after exposure to ambient conditions for 4 min. The spectra are very similar and were both fitted using two Gaussians (at 285.1 and 286.4 eV); no new component assignable to C=O is observed; c) O 1s peak before and after exposure to air exposure (presumably due to adventitious O-containing species), which shows a good overlap and no new components attributable to C=O or to additional surface oxide or hydroxide species. Spectra courtesy of Hye Kyung Kim of the Marder group at Georgia Tech.

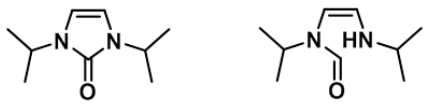

Figure 4.8: Structures of possible NHC decomposition products of IiPr.

Figure 4.7 shows XPS spectra of NHC-modified Au before and after air exposure. However, no clear evidence for decomposition products is obtained. The urea and amide shown in Figure 4.8 are possible products of oxidation and hydrolysis, respectively, of the NHC (and are calculated using DFT to result in WF reductions of 1.00 and 0.80 eV vs. bare gold, i.e. higher WFs than IiPr). However, no evidence for these species is found using XPS: carbonyl groups are expected to show peaks at around 287.5 eV, at a higher position than C-C groups.[50] The O 1s spectra for before and after also shows no change to the overall peak size as shown by the good overlap of the two trials (Figure 4.7c). Thus, the XPS is not sufficiently sensitive to enable us to determine the mechanism by which the WF is raised on exposure to air.

4.3.4 Origin of Work-Function Modification

The breakdown of DFT-calculated contributions to $\Delta\Phi$ given in Table 4.3 suggests that $\Delta V_{\text{geom.}}$ is not a significant factor and thus that $\Delta\Phi$ is dominated by $\Delta V_{\text{int.dip.}}$ and $\Delta V_{\text{mol.}}$. For a given set of *N*,*N*′-substituents, the magnitude of $\Delta V_{\text{mol.}}$ increases with the expected N—C—N angle (see Figure 4.1) and basicity, while variation in $\Delta V_{\text{int.dip.}}$ is less straightforward. More interestingly, this breakdown suggests qualitative differences between, on the one hand, the small NHCs, with isopropyl substituents, for which the majority of $\Delta\Phi$ is from $\Delta V_{\text{int.dip.}}$, and, on the other hand, the bulkier NHCs, with *N*,*N*′-bis(2,6-diisopropylphenyl) substituents. In the latter cases, the magnitudes of the $\Delta V_{\text{int.dip.}}$ values are lower, and those of ΔV_{mol} larger than for the iPr species, resulting in approximately equal contributions to $\Delta\Phi$ from interface and molecular dipoles.

Figure 4.9 shows the plane-averaged electron charge-density difference, $\Delta\rho$, for **IiPr** and **IDipp**, along with the optimized geometries (**SIiPr** and **SIDipp** are shown in Figure 4.10). The charge-density difference was calculated by subtracting from the charge density of the combined NHC-Au system the charge density of each component (NHC and Au) at the geometry it is calculated to have after interaction with the other component. Each system shows reorganization of charge density at the interface between the top of the gold and the NHC modifier above, but with larger changes in charge density for the IiPr system, consistent with the larger $\Delta V_{\text{int.dip.}}$ contribution. This interface dipole results from contributions due to charge transfer through coordination of the Lewis-basic NHC non-bonding electron pair to the surface, the "cushion" effect[51-52] (corresponding to the push-back of the electronic density spilling from the clean metal surface), and overall charge redistribution at the interface.

Examination of the optimized geometries of the NHC-modified surfaces, as well as of the evolution of the Bader partial atomic charges,[33] for the carbene carbon atoms on Au and isolated from the surface (considering the same relaxed geometry), explains the much lower magnitudes of $\Delta V_{\text{int.dip.}}$ for the Dipp NHCs (see Table 4.5, Figure 4.9). The carbene carbon of the iPr substituted NHCs are clearly coordinated to a single Au atom, which, in the relaxed geometry, is slightly displaced from the metal surface; the Au—C distances for the iPr series are comparable with those calculated in previous studies of NHC monolayers with similarly sized *N*,*N*′-substituents,[12, 19, 53] and are similar to typical bond lengths in NHC Au^{I} complexes.[54-55] On the other hand, the carbene carbons of the bulky Dipp carbenes are located at very long, non-bonded distances from the nearest gold atom. In a previous computational study of comparably bulky NHCs on Au, a C_{carbene}—Au distance

of 2.04 Å was obtained; however, the computational model involved placement of a single Au atom on the Au surface.[14] Consistent with the difference in geometries, the Bader charges indicate a significant increase in positive charge density on the carbene carbons of the NHCs with iPr substituents on binding to Au, consistent with charge transfer to the surface; on the other hand, for the NHCs with Dipp substituents, the Bader charges on the carbene carbon atoms are essentially the same as in the isolated molecules, which implies that $\Delta V_{\text{int.dip.}}$ in the Dipp series arises only from the "cushion" effect[51-52] and charge redistributions at the interface.

Table 4.5: DFT Calculated Parameters Relating to the Au—NHC Interaction.

		$C_{carbene}$ Bader Charge / |e|		NHC—Au Binding Energy / eV	
NHC	**$C_{carbene}$—Au / Å**	**NHC on Au**	**Isolated NHC**	**Total[a]**	**Dispersion[b]**
iPr$_2$bimy	2.14	0.41	0.21	-2.84	-1.33
IiPr	2.12	0.40	0.19	-2.87	-1.27
SIiPr	2.14	0.47	0.26	-2.88	-1.30
IDipp	4.11	0.26	0.24	-2.34	-2.51
SIDipp	4.54	0.33	0.32	-1.87	-2.18
6Dipp	5.06	0.33	0.31	-2.04	-2.08

[a] Total energy of the Au(111) surface with NHC, calculated using the D3 dispersion correction at the PBE-D3/PW optimized geometries, minus the sum of the energies of the isolated Au and NHC, which are considered to have the same relaxed geometry after interacting with the other component. A negative value means that the dispersion-corrected system is more stable than the original system. [b] Dispersion contribution to the total NHC—Au binding energy obtained by calculating the total energy without the D3 dispersion correction at the PBE-D3/PW optimized geometries and subtracting it from the dispersion-corrected value.

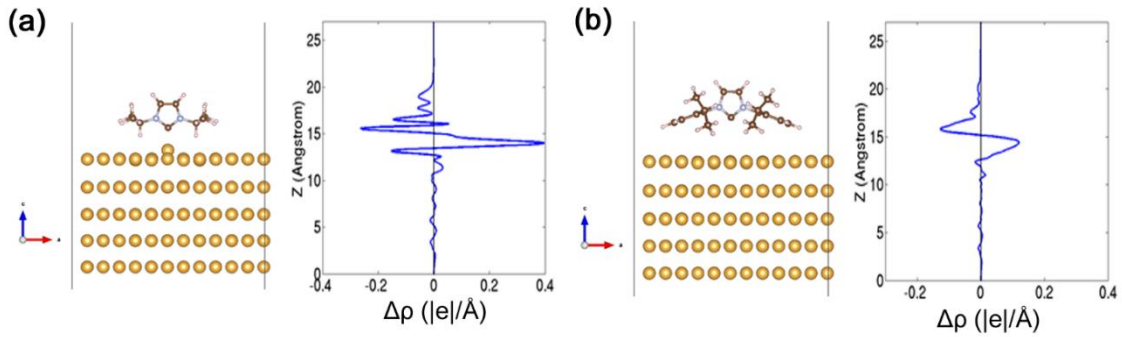

Figure 4.9: Optimized structures and plane-averaged change in charge density (Δρ) for (a) IiPr and (b) IDipp. Negative Δρ corresponds to an increased positive charge relative to the bare gold and isolated NHCs, whereas positive Δρ corresponds to increased negative charge.

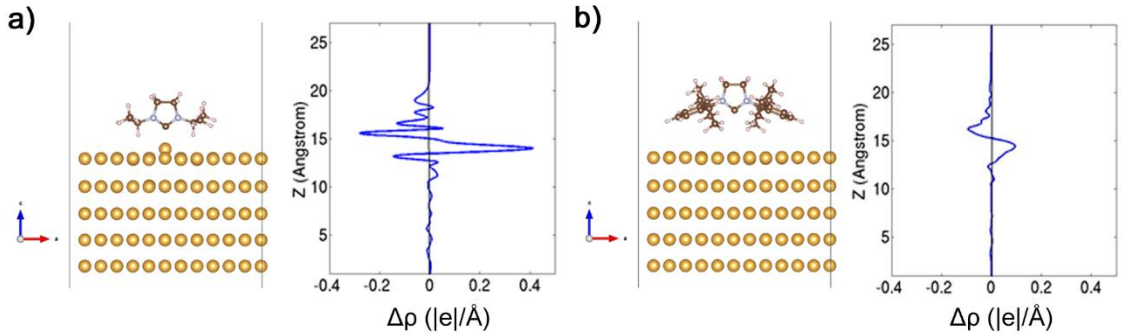

Figure 4.10: Optimized structure and plane-averaged change in charge density (Δρ) for SIiPr (a) and SIDipp (b). Negative Δρ corresponds to an increased positive charge relative to the bare gold and isolated NHCs, whereas positive Δρ corresponds to increased negative charge.

Given (i) the experimental evidence, both in this collaborative work and that of others, that bulky carbenes do bind to gold and (ii) the calculated geometries and Bader charges that indicate negligible $C_{carbene}$—Au covalent bonding, we were interested in examining why these carbenes with Dipp substituents even bind to the surface. Calculations show that the dispersion energy gained when Dipp-substituted NHCs bind to gold are, on average, 2.3 eV, whereas the iPr substituted NHCs, only gain 1.3 eV from dispersion interactions on binding to Au (see Table 4.5). Thus, the increased van der Waals

interactions in the Dipp substituted NHCs, presumably arising from the larger substituents, essentially compensate for the stabilization obtained when the iPr NHCs form a covalent bond between the lone pair of the carbene carbon and the surface.

Low-WF materials are generally expected to behave as more effective electron-injecting electrodes than high-WF materials. For example, PEIE-coated Au has previously been shown to afford lower threshold-voltage values and higher electron-mobility values than bare gold when applied as the source and drain electrodes in n-channel organic field-effect transistors.[1] To examine whether NHC-modified Au behaves in a similar way, Felipe Larrain and Canek Fuentes-Hernandez of the Kippelen group at Georgia Tech and Hye Kyung Kim of the Marder group at Georgia Tech prepared diode-like devices with the structures Au (150 nm, with or without modification)/C_{60} (100 nm)/MoO_x (10 nm)/Ag (150 nm). **SIDipp**-modified Au was used for these experiments and, in addition to bare gold, Au modified with spin-coated PEIE was used as a comparison material with similar WF (3.4 eV, UPS).[1] As shown in Figure 4.11 and Figure 4.12, **SIDipp**-modified and PEIE-modified devices gave rise to diode-like behavior with a higher rectification, which is indicative of improved electron injection from these electrodes to C_{60} than from the reference, unmodified electrodes. The highest rectification ratio (at ±1 V) for a **SIDipp**-modified device was determined to be 6×10^3.

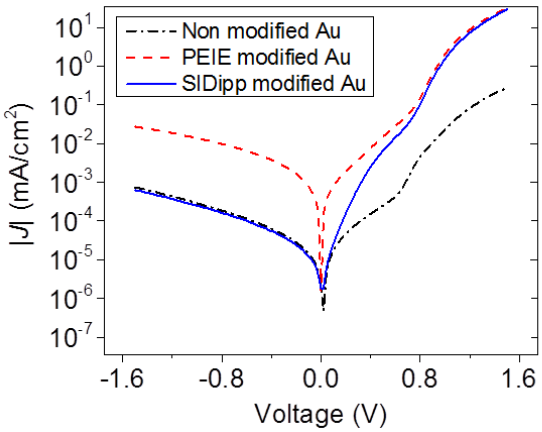

Figure 4.11: Semilogarithmic plots of J–V characteristics for diodes with Au (150 nm, with or without modification)/C_{60} (100 nm)/MoOx (10 nm)/Ag (150 nm). Spectra courtesy of Felipe Larrain and Canek Fuentes-Hernandez of the Kippelen group at Georgia Tech and Hye Kyung Kim of the Marder group at Georgia Tech.

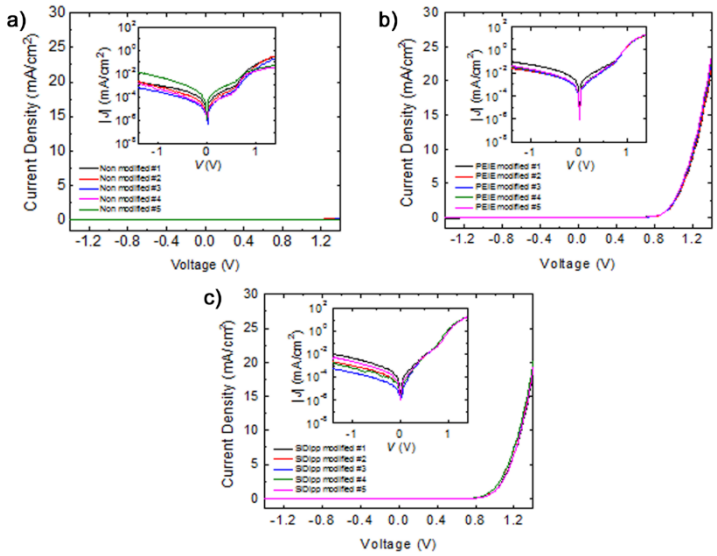

Figure 4.12: Semi-logarithmic plots of J-V characteristics showing sample-to-sample variations for devices with structure Au(with or without modification)/C_{60}(100 nm)/MoO_3(10 nm)/Ag(150 nm) using a) unmodified Au, b) PEIE-modified Au, and c) SIDipp-modified Au. The yield for PEIE modified devices was 93% and for SIDipp modified devices 40%. Spectra courtesy of Felipe Larrain and Canek Fuentes-Hernandez of the Kippelen group at Georgia Tech and Hye Kyung Kim of the Marder group at Georgia Tech.

4.4 Conclusions

NHCs are emerging as a flexible tool for materials scientists to impart functionality to metal surfaces,[9] but the accompanying effect of these modifiers on the metal WF has only been so far addressed in one computational study.[19] Here collaborators have experimentally demonstrated that NHC modification of Au surfaces results in large reductions in WF relative to unmodified gold, larger than those achieved with alkanethiolates and comparable to the effects of PEI(E) or solution-processed reducing organometallic dimers. These reductions are obtained for NHCs with both relatively small (diisopropyl) and bulky (bis(2,6-diisopropylphenyl)) *N,N′*-substituents.

DFT calculations gave good agreement of the carbene coverage obtained from XPS measurements by Hye Kyung Kim of the Marder group at Georgia Tech. Calculated results indicate very different interactions between the carbene and the gold for these two classes of NHCs. For the former, the carbene carbon atom is covalently bound to a gold atom, with the associated charge redistribution making a significant contribution to the interface dipole. In the latter, the interface dipole is smaller, but, to some extent, compensated by a larger molecular dipole. For both substituent sizes, the structure of the heterocyclic core was shown to be only a small factor (around 10% of the total work function change, or 0.1 eV) to consider for work function modification with N-heterocyclic carbenes. Bader charge analysis shows that carbenes with the smaller iPr substituents undergo charge transfer to the surface, compared to the isolated carbene molecule, while the Dipp substituted carbenes are almost the same on the surface as an isolated carbene molecule. Examining the contribution of the dispersion energy to the binding energy reveals the reason why the large carbenes with Dipp substituents even stay bound to the surface. Without dispersion

corrections, Dipp substituted carbenes are not energetically stable while interacting the gold surface. But due to dispersion stabilization by on average 2.3 eV, which is almost 1 eV more than the smaller iPr substituted carbenes, these Dipp substituted carbenes are now energetically stable when interacting with the surface.

In C_{60} diodes, NHC-modified Au was shown by collaborators to act as an effective electron-injecting electrode, behaving similarly to PEIE-modified Au, albeit with lower air stability. Therefore, NHC-modified Au electrodes may be useful in applications where low-WF electrodes are required, especially when additional functionality, besides low WF, is desired given the synthetic flexibility of NHCs and recent demonstrations of their use in attaching a variety of other species to Au surfaces.[12, 14]

4.5 References

1. Zhou, Y.; Fuentes-Hernandez, C.; Shim, J.; Meyer, J.; Giordano, A. J.; Li, H.; Winget, P.; Papadopoulos, T.; Cheun, H.; Kim, J.; Fenoll, M.; Dindar, A.; Haske, W.; Najafabadi, E.; Khan, T. M.; Sojoudi, H.; Barlow, S.; Graham, S.; Brédas, J.-L.; Marder, S. R.; Kahn, A.; Kippelen, B. "A Universal Method to Produce Low-Work Function Electrodes for Organic Electronics." *Science* **2012,** *336*, 327-332.

2. Schlenoff, J. B.; Li, M.; Ly, H. "Stability and Self-Exchange in Alkanethiol Monolayers." *J. Am. Chem. Soc.* **1995,** *117* (50), 12528-12536.

3. Schoenfisch, M. H.; Pemberton, J. E. "Air Stability of Alkanethiol Self-Assembled Monolayers on Silver and Gold Surfaces." *J. Am. Chem. Soc.* **1998,** *120* (18), 4502-4513.

4. Lin, J. C. Y.; Huang, R. T. W.; Lee, C. S.; Bhattacharyya, A.; Hwang, W. S.; Lin, I. J. B. "Coinage Metal-*N*-Heterocyclic Carbene Complexes." *Chem. Rev.* **2009,** *109* (8), 3561-3598.

5. Arnold, P. L.; Casely, I. J. "F-Block N-Heterocyclic Carbene Complexes." *Chem. Rev.* **2009,** *109* (8), 3599-3611.

6. Díez-González, S.; Marion, N.; Nolan, S. P. "N-Heterocyclic Carbene in Late Transition Metal Catalysis." *Chem. Rev.* **2009,** *109* (8), 3612-3676.

7. Samojłowicz, C.; Bieniek, M.; Grela, K. "Ruthenium-Based Olefin Metathesis Catalysts Bearing N-Heterocyclic Carbene Ligands." *Chem. Rev.* **2009,** *109* (8), 3708-3742.

8. Hindi, K. M.; Panzner, M. J.; Tessier, C. A.; Cannon, C. L.; Youngs, W. J. "The Medicinal Applications of Imidazolium Carbene−Metal Complexes." *Chem. Rev.* **2009,** *109* (8), 3859-3884.

9. Zhukhovitskiy, A. V.; MacLeod, M. J.; Johnson, J. A. "Carbene Ligands in Surface Chemistry: From Stabilization of Discrete Elemental Allotropes to Modification of Nanoscale and Bulk Substrates." *Chem. Rev.* **2015,** *115* (20), 11503-11532.

10. Vignolle, J.; Tilley, T. D. "N-Heterocyclic carbene-stabilized gold nanoparticles and their assembly into 3D superlattices." *Chem. Commun.* **2009,** (46), 7230-7232.

11. Roland, S.; Ling, X.; Pileni, M.-P. "N-Heterocyclic Carbene Ligands for Au Nanocrystal Stabilization and Three-Dimensional Self-Assembly." *Langmuir* **2016,** *32* (31), 7683-7696.

12. Crudden, C. M.; Horton, J. H.; Ebralidze, I. I.; Zenkina, O. V.; McLean, A. B.; Drevniok, B.; She, Z.; Kraatz, H.-B.; Mosey, N. J.; Seki, T.; Keske, E. C.; Leake, J. D.; Rousina-Webb, A.; Wu, G. "Ultra stable self-assembled monolayers of N-heterocyclic carbenes on gold." *Nat. Chem.* **2014,** *6* (5), 409-414.

13. Weidner, T.; Baio, J. E.; Mundstock, A.; Große, C.; Karthäuser, S.; Bruhn, C.; Siemeling, U. "NHC-Based Self-Assembled Monolayers on Solid Gold Substrates." *Aust. J. Chem.* **2011,** *64* (8), 1177-1179.

14. Zhukhovitskiy, A. V.; Mavros, M. G.; Van Voorhis, T.; Johnson, J. A. "Addressable Carbene Anchors for Gold Surfaces." *J. Am. Chem. Soc.* **2013,** *135* (20), 7418-7421.

15. Arduengo III, A. J.; Harlow, R. L.; Kline, M. "A Stable Crystalline Carbene." *J. Am. Chem. Soc.* **1991,** *113* (1), 361-363.

16. Magill, A. M.; Cavell, K. J.; Yates, B. F. "Basicity of Nucleophilic Carbenes in Aqueous and Nonaqueous Solvents-Theoretical Predictions." *J. Am. Chem. Soc.* **2004,** *126* (8), 8717-8724.

17. Nuzzo, R. G.; Dubois, L. H.; Allara, D. L. "Fundamental Studies of Microscopic Wetting on Organic Surfaces. 1. Formation and Structural Characterization of a Self-Consistent Series of Polyfunctional Organic Monolayers." *J. Am. Chem. Soc.* **1990,** *112* (2), 558-569.

18. Lavrich, D. J.; Wetterer, S. M.; Bernasek, S. L.; Scoles, G. "Physisorption and Chemisorption of Alkanethiols and Alkyl Sulfides on Au(111)." *J. Phys. Chem. B* **1998,** *102* (18), 3456-3465.

19. Adhikari, B.; Meng, S.; Fyta, M. "Carbene-mediated self-assembly of diamondoids on metal surfaces." *Nanoscale* **2016,** *8* (16), 8966-8975.

20. Huynh, H. V.; Han, Y.; Ho, J. H. H.; Tan, G. K. "Palladium(II) Complexes of a Sterically Bulky, Benzannulated N-Heterocyclic Carbene with Unusual Intramolecular C−H···Pd and $C_{carbene}$···Br Interactions and Their Catalytic Activities." *Organometallics* **2006,** *25* (13), 3267-3274.

21. Ryan, S. J.; Schimler, S. D.; Bland, D. C.; Sanford, M. S. "Acyl Azolium Fluorides for Room Temperature Nucleophilic Aromatic Fluorination of Chloro- and Nitroarenes." *Org. Lett.* **2015,** *17* (8), 1866-1869.

22. Hintermann, L. "Expedient syntheses of the N-heterocyclic carbene precursor imidazolium salts IPr·HCl, IMes·HCl and IXy·HCl." *Beilstein J. Org. Chem.* **2007,** *3*, No. 22.

23. Arduengo III, A. J.; Krafczyk, R.; Schmutzler, R.; Craig, H. A.; Goerlich, J. R.; Marshall, W. J.; Unverzagt, M. "Imidazolylidenes, imidazolinylidenes and imidazolidines." *Tetrahedron* **1999,** *55* (51), 14523-14534.

24. Kolychev, E. L.; Portnyagin, I. A.; Shuntikov, V. V.; Khrustalev, V. N.; Nechaev, M. S. "Six- and seven-membered ring carbenes: Rational synthesis of amidinium salts, generation of carbenes, synthesis of Ag(I) and Cu(I) complexes." *J. Organomet. Chem.* **2009,** *694* (15), 2454-2462.

25. Wildöer, J. W. G.; Venema, L. C.; Rinzler, A. G.; Smalley, R. E.; Dekker, C. "Electronic structure of atomically resolved carbon nanotubes." *Nature* **1998,** *391* (6992), 59-62.

26. Reckien, W.; Janetzko, F.; Peintinger, M. F.; Bredow, T. "Implementation of Empirical Dispersion Corrections to Density Functional Theory for Periodic Systems." *J. Comput. Chem.* **2012,** *33* (25), 2023-2031.

27. Kresse, G.; Furthmüller, J. "Efficiency of ab-inito total energy calculations for metals and semiconductors using a plane-wave basis set." *Comput. Mater. Sci.* **1996,** *6* (1), 15-50.

28. Kresse, G.; Furthmüller, J. "Efficient iterative schemes for ab initio total-energy calculations using a plane-wave basis set." *Phys. Rev. B* **1996,** *54* (16), 11169-11186.

29. Perdew, J. P.; Burke, K.; Ernzerhof, M. "Generalized Gradient Approximation Made Simple." *Phys. Rev. Lett.* **1996,** *77* (18), 3865-3868.

30. Perdew, J. P.; Burke, K.; Ernzerhof, M. "Generalized Gradient Approximation Made Simple [Phys. Rev. Lett. 77, 3865 (1996)] Errata." *Phys. Rev. Lett.* **1997,** *78* (7), 1396.

31. Grimme, S.; Antony, J.; Ehrlich, S.; Krieg, H. "A consistent and accurate ab initio parametrization of density functional dispersion correction (DFT-D) for the 94 elements H-Pu." *J. Chem. Phys.* **2010,** *132*, 154104(1-19).

32. Goerigk, L.; Grimme, S. "A thorough benchmark of density functional methods for general main group thermochemistry, kinetics, and noncovalent interactions." *Phys. Chem. Chem. Phys.* **2011,** *13* (14), 6670-6688.

33. Tang, W.; Sanville, E.; Henkelman, G. "A grid-based Bader analysis algorithm without lattice bias." *J. Phys.: Condens. Matter* **2009,** *21*, 084204(1-7).

34. Frisch, M. J.; Trucks, G. W.; Schlegel, H. B.; Scuseria, G. E.; Robb, M. A.; Cheeseman, J. R.; Scalmani, G.; Barone, V.; Mennucci, B.; Petersson, G. A.; Nakatsuji, H.; Caricato, M.; Li, X.; Hratchian, H. P.; Izmaylov, A. F.; Bloino, J.; Zheng, G.; Sonnenberg, J. L.; Hada, M.; Ehara, M.; Toyota, K.; Fukuda, R.; Hasegawa, J.; Ishida, M.; Nakajima, T.; Honda, Y.; Kitao, O.; Nakai, H.; Vreven, T.; Montgomery, J. A., Jr.; ; Peralta, J. E.; Ogliaro, F.; Bearpark, M.; Heyd, J. J.; Brothers, E.; Kudin, K. N.; Staroverov, V. N.; Kobayashi, R.; Normand, J.; Raghavachari, K.; Rendell, A.; Burant, J. C.; Iyengar, S. S.; Tomasi, J.; Cossi, M.; Rega, N.; Millam, J. M.; Klene, M.; Knox, J. E.; Cross, J. B.; Bakken, V.; Adamo, C.; Jaramillo, J.; Gomperts, R.; Stratmann, R. E.; Yazyev, O.; Austin, A. J.; Cammi, R.; Pomelli, C.; Ochterski, J. W.; Martin, R. L.; Morokuma, K.; Zakrzewski, V. G.; Voth, G. A.; Salvador, P.; Dannenberg, J. J.; Dapprich, S.; Daniels, A. D.; Farkas, Ö.; Foresman, J. B.; Ortiz, J. V.; Cioslowski, J.; Fox, D. J. *Gaussian 09*, Gaussian, Inc.: Wallingford, CT, 2009.

35. Kendall, R. A.; Dunning, T. A.; Harrison, R. J. "Electron affinities of the first-row atoms revisited. Systematic basis sets and wave functions." *J. Chem. Phys.* **1992,** *96*, 6796-6806.

36. Paniagua, S. A.; Li, E. L.; Marder, S. R. "Adsorption studies of a phosphonic acid on ITO: film coverage, purity, and induced electronic structure changes." *Phys. Chem. Chem. Phys.* **2014,** *16* (7), 2874-2881.

37. Li, H.; Paramonov, P. B.; Brédas, J.-L. "Theoretical study of the surface modification of indium tin oxide with trifluorophenyl phosphonic acid molecules: impact of coverage density and binding geometry." *J. Mater. Chem.* **2010,** *20*, 2630-2637.

38. de Boer, B.; Hadipour, A.; Mandoc, M. M.; van Woudenbergh, T.; Blom, P. W. M. "Tuning of Metal Work Functions with Self-Assembled Monolayers." *Adv. Mater.* **2005,** *17* (5), 621-625.

39. Alloway, D. M.; Hofmann, M.; Smith, D. L.; Gruhn, N. E.; Graham, A. L.; Colorado, J., Ramon; ; Wysocki, V. H.; Lee, T. R.; Lee, P. A.; Armstrong, N. R. "Interface Dipoles Arising from Self-Assembled Monolayers on Gold: UV-Photoemission Studies of Alkanethiols and Partialy Fluorinated Alkanethiols." *J. Phys. Chem. B* **2003,** *107*, 11690-11699.

40. Narasimha, K. T.; Ge, C.; Fabbri, J. D.; Clay, W.; Tkachenko, B. A.; Fokin, A. A.; Schreiner, P. R.; Dahl, J. E.; Carlson, R. M. K.; Shen, Z. X.; Melosh, N. A. "Ultralow effective work function surfaces using diamondoid monolayers." *Nat. Nanotechnol.* **2016,** *11* (3), 267-272.

41. Giordano, A. J.; Pulvirenti, F.; Khan, T. M.; Fuentes-Hernandez, C.; Moudgil, K.; Delcamp, J. H.; Kippelen, B.; Barlow, S.; Marder, S. R. "Organometallic Dimers: Application to Work Function Reduction of Conducting Oxides." *ACS Appl. Mater. Interfaces* **2015,** *7* (7), 4320-4326.

42. Akaike, K.; Nardi, M. V.; Oehzelt, M.; Frisch, J.; Opitz, A.; Christodoulou, C.; Ligorio, G.; Beyer, P.; Timpel, M.; Pis, I.; Bondino, F.; Moudgil, K.; Barlow, S.; Marder, S. R.; Koch, N. "Effective Work Function Reduction of Practical Electrodes Using an Organometallic Dimer." *Adv. Funct. Mater.* **2016,** *26* (15), 2493-2502.

43. Sander, W. "Carbonyl Oxides: Zwitterions or Diradicals?" *Angew. Chem., Int. Ed.* **1990,** *29* (4), 344-354.

44. Li, F.; Zhou, Y.; Zhang, F.; Liu, X.; Zhan, Y.; Fahlman, M. "Tuning Work Function of Noble Metals As Promising Cathodes in Organic Electronic Devices." *Chem. Mater.* **2009,** *21*, 2798-2802.

45. Li, H.; Duan, Y.; Coropceanu, V.; Brédas, J.-L. "Electronic structure of the pentacene-gold interface: A density-functional theory study." *Org. Electron.* **2009,** *10*, 1571-1578.

46. Fenwick, O.; Van Dyck, C.; Murugavel, K.; Cornil, D.; Reinders, F.; Haar, S.; Mayor, M.; Cornil, J.; Samorì, P. "Modulating the charge injection in organic field-effect transistors: fluorinated oligophenyl self-assembled monolayers for high work function electrodes." *J. Mater. Chem. C* **2015,** *3* (13), 3007-3015.

47. Li, H.; Duan, Y.; Paramonov, P. B.; Coropceanu, V.; Brédas, J.-L. "Electronic structure of self-assembled (fluoro)methylthiol monolayers on the Au(111) surface: Impact of fluorination and coverage density." *J. Electron Spectrosc. Relat. Phenom.* **2009,** *174*, 70-77.

48. Cornil, D.; Cornil, J. "Work-function modification of the (111) gold surface upon deposition of self-assembled monolayers based on alkanethiol derivatives." *J. Electron Spectrosc. Relat. Phenom.* **2013,** *189*, 32-38.

49. Wood, C.; Li, H.; Winget, P.; Brédas, J.-L. "Binding Modes of Fluorinated Benzylphosphonic Acids on the Polar ZnO Surface and Impact on Work Function." *J. Phys. Chem. C* **2012,** *116*, 19125-19133.

50. Ago, H.; Kugler, T.; Cacialli, F.; Salaneck, W. R.; Shaffer, M. S. P.; Windle, A. H.; Friend, R. H. "Work Functions and Surface Functional Groups of Multiwall Carbon Nanotubes." *J. Phys. Chem. B* **1999,** *103* (38), 8116-8121.

51. Chen, Y. C.; Cunningham, J. E.; Flynn, C. P. "Dependence of rare-gas-adsorbate dipole moment on substrate work function." *Phys. Rev. B* **1984,** *30* (12), 7317-7319.

52. Hwang, J.; Wan, A.; Kahn, A. "Energetics of metal-organic interfaces: New experiments and assessment of the field." *Mat. Sci. Eng. R* **2009,** *64*, 1-31.

53. Rodríguez-Castillo, M.; Laurencin, D.; Tielens, F.; van der Lee, A.; Clément, S.; Guari, Y.; Richeter, S. "Reactivity of gold nanoparticles towards N-heterocyclic carbenes." *Dalton Trans.* **2014,** *43* (16), 5978-5982.

54. Wang, H. M. J.; Chen, C. Y. L.; Lin, I. J. B. "Synthesis, Structure, and Spectroscopic Properties of Gold(I)−Carbene Complexes." *Organometallics* **1999,** *18* (7), 1216-1223.

55. de Frémont, P.; Scott, N. M.; Stevens, E. D.; Nolan, S. P. "Synthesis and Structural Characterization of *N*-Heterocyclic Carbene Gold(I) Complexes." *Organometallics* **2005,** *24* (10), 2411-2418.

CHAPTER 5

PHOSPHONIC ACID SURFACE MODIFIERS WITH ELECTRON-WITHDRAWING MOIETIES: IMPACT ON MOLECULAR ORIENTATION, COVERAGE, AND WORK FUNCTION OF INDIUM TIN OXIDE

5.1 Introduction

As we have documented already, surface modifiers have been used to improve the performance of electronic devices including OLEDs[1-7], OFETs[8-9] and OPVs;[1, 10-11] they can improve adhesion/wettability of the active layers,[12-13] control blend phase separation and morphology,[14-17] and are useful for tuning work functions and interfacial charge injection barriers.[3, 6, 18] Phosphonic acids (PAs) in particular are known to form robust monolayers that increase interfacial compatibility between a transparent conductive oxide and the organic device layer in optoelectronic devices.[12, 19-22] While the properties of surface modifiers such as thiols on coinage metals[23-24] are well-studied, the molecular-level details of technologically relevant modifiers, such as aromatic PAs on transparent conductive oxides, are just starting to be explored.[25-28] Alkyl, phenyl, and benzyl PA surface modifiers have been investigated previously for their work function modification abilities.[3-6, 12, 18, 28-35]

Phosphonic acid binding mode, orientation, and surface coverage can affect the contact angle and work function (WF) of modified oxide surfaces.[36-38] These details are critical to the design and performance of modified interfaces in thin film electronics. The work-function modification, $\Delta\Phi$, is described by Equation 1.5. In a simplified picture without considering the interface dipole[2, 18, 20, 29, 39], the magnitude of $\Delta\Phi$ induced by a molecular layer is given by:

$$\Delta\Phi = \frac{ne \cdot \mu_{\mathrm{mol}} \cos\theta}{\varepsilon_0 \cdot \varepsilon} \tag{5.1}$$

Here, n is the coverage density, e is the fundamental charge, μ_{mol} is the molecular dipole moment, θ is the angle the dipole moment makes with the surface normal, ε is the dielectric constant, and ε_0 is the vacuum permittivity.[40-41] However, while quantum-chemical calculations can provide ε, as well as μ_{mol}, at the single molecule level, the other parameters needed to calculate $\Delta\Phi$, notably n and θ, have to be determined experimentally, in order to understand what is physically happening in these systems.

Perylene tetracarboxylic diimide (PDI) and its derivatives have been widely used for many different applications, including organic solar cells,[42-44] organic field-effect transistors,[43] solid-state lighting,[45] laser,[46] and sensor applications.[47] PDI has high thermal and photo-stability, strong absorption in the visible part of the spectrum between 450 and 650 nm, decent electron mobilities of 10^{1}-10^{-3} $cm^2/(V\ s)$, high fluorescence quantum yield and high electron affinity.[42-43, 48-49] The chemical structures of the PDIs also offer a large number of positions that can be functionalized or modified for a specific property, such as preventing aggregation[45] or increasing solubility. Symmetric, doubly PA-modified PDIs have been used for surface modification,[28] but to the best of our knowledge, singly PA-

modified PDIs have not been used as monolayers bound to a surface to cause work function changes.

In a previous work[26], the molecular orientation of a model phosphonic acid, phenyl phosphonic acid was studied systematically on indium zinc oxide. The system was found to be well ordered, with a well-defined orientation, and an absence of inter-molecular (i.e. steric) effects. In this chapter, DFT calculations are used to evaluate the interfacial electronic structure, the molecular orientation, and the work function modification of 15 phosphonic acid molecules on ITO. In particular, we consider molecules with strong electron-withdrawing groups, including nitro functional group and PDIs, to complement the fluorinated phosphonic acid molecules previously examined in the literature and to compare their effects on the work function modification ability and mechanism.

5.2 Computational Methodology

To describe the ITO(222) surface, we use the repeated-slab approach and a surface structural model described in Section 3.2. All of the benzyl PAs (see the chemical structures in Figure 5.1), including unmodified as well as functionalized with fluoro, trifluoromethyl, or nitro groups, are bound in site 1 in the ITO surface unit cell (see below and Figure 5.2), resulting in a molecular coverage density of 2.82×10^{13} molecules cm^{-2}. In order to evaluate the effect of intermolecular interactions on the variation of the tilt angle, we consider a higher coverage density of 1.1×10^{14} molecules cm^{-2} using the unmodified benzyl-phosphonic acid (BPA) as an example, which is equivalent to four PA molecules per unit cell. For all of the PDI-linker-PAs, known hereafter as PDI-PAs, calculations were performed with two molecules per ITO unit cell in sites 1 and 2, in accordance with

preliminary results from cyclic voltammetry, performed by Yilong Zheng of the Saavedra group at the University of Arizona, yielding a coverage density of 5.64×10^{13} molecules cm^{-2}. The atomic positions of the top In(Sn)-O layer, surface hydroxyls, and any molecular adsorbate are allowed to relax over the course of geometry relaxations while the bottom two layers of the slab remain fixed.

As described in Section 3.2, all calculations were carried out using the Vienna Ab Initio Simulation Package (VASP).[50-51] The generalized gradient approximation (GGA) exchange-correlation functional of Perdew, Burke, and Ernzerhof (PBE)[52-53] was used. The k-point grid and smearing value are the same as the IrCpCp* work on ITO presented in Section 3.2. The improved tetrahedron method with Blöchl corrections[54] occupation scheme was used for the benzylphosphonic acids, while the PDI-PA calculations required the Methfessel-Paxton[55] occupation scheme, due to charge sloshing in the systems. Geometry optimizations and compensation for possible dipole-dipole interactions between the asymmetric slabs were the same as presented in Section 3.2. After the PA/ITO interface geometry was optimized, the tilt angle for each phosphonic acid molecule was obtained simply by using the coordinates of their component atoms.

5.3 Results and Discussion

5.3.1 Phosphonic Acid Molecules of Interest

The benzyl and PDI PA molecules investigated in this study were chosen to better understand the nature of the interaction of these types of molecules with the ITO surface. In particular, fluoro and trifluoromethyl substituted, hereafter denoted as fluorinated, and nitro-benzyl phosphonic acids were chosen due to their ability to drastically alter the work

function of a substrate because of the molecular dipoles induced by the presence of the electron-withdrawing groups. Moreover, fluorination also has the benefit of allowing straightforward characterization of the surface after modification by XPS analysis[56] as fluorine is not a common contaminant deposited on the surface by standard processing techniques. Fluorine (along with the other halogens) has a large relative sensitivity factor compared with other elements and therefore even small concentrations of fluorine on the surface of a substrate can be readily detected by XPS, which is ideal for the analysis of monolayers.[56] The phosphonic acids that have been chosen for this study and their respective abbreviations, which will be used throughout, are summarized in Figure 5.1. Some of the fluorinated benzyl phosphonic acids (BPAs) have already been well characterized in terms of work function changes,[3-4, 6, 12, 18, 30, 32-33] but the selection of these fluorinated BPAs, nitro BPA, and PDI PAs allows for a comparison of the mechanism of work function modification. As discussed in the "Computational Methodology" section, site 1 is the adsorption site for all benzyl PAs, including unmodified and functionalized at the lowest coverage (1 molecule/unit cell), while sites 1 and 2 are considered for the PDI-PAs (2 molecules/unit cell), and all four sites are used for the highest coverage unmodified BPA (see Figure 5.2 below).

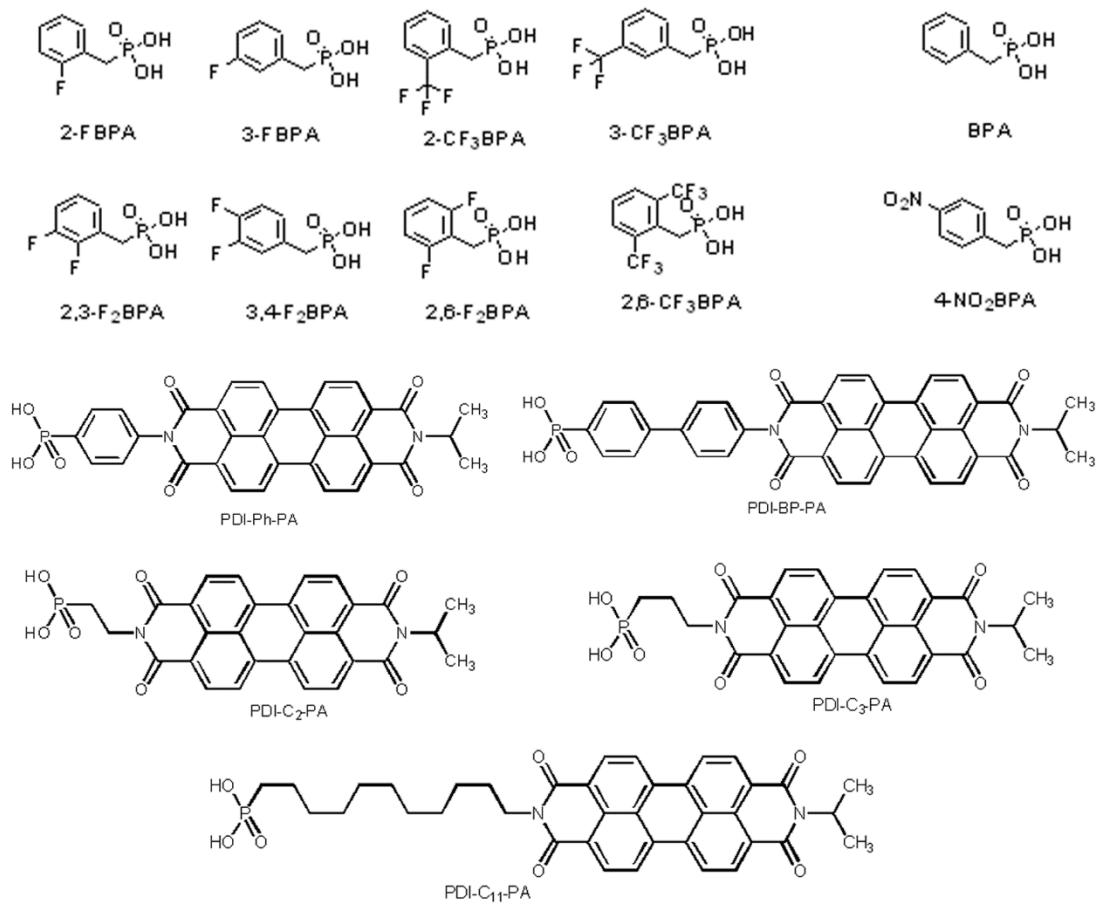

Figure 5.1: Chemical structures of phosphonic acids used in this study along with the abbreviations that will be used throughout.

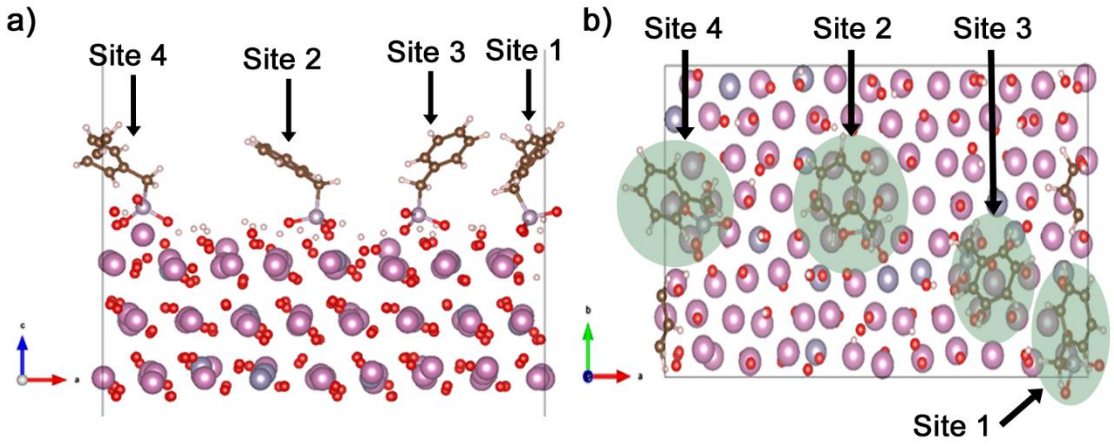

Figure 5.2: Binding sites in the ITO structural model used in this study viewed from the side (a) and the top (b). The benzyl PAs are in site 1, PDI-PAs have two molecules which are in sites 1 and 2, and the high coverage BPAs have four molecules which are in sites 1, 2, 3, and 4.

5.3.2 Orientation of the PAs

Optimized geometries of the PAs on the ITO surface were used to determine the orientation of the PA with respect to the surface normal. The general structure of the BPAs and PDI-PAs examined in the study can be found below in Figure 5.3, with the tilt angle between the normal of the benzene ring and the surface normal, denoted as α. With this definition, the PAs that are standing straight up have α values close to 90°, while those lying parallel to the surface have an α value close to 0°. All tilt angles are reported in Figure 5.4 and Table 5.1.

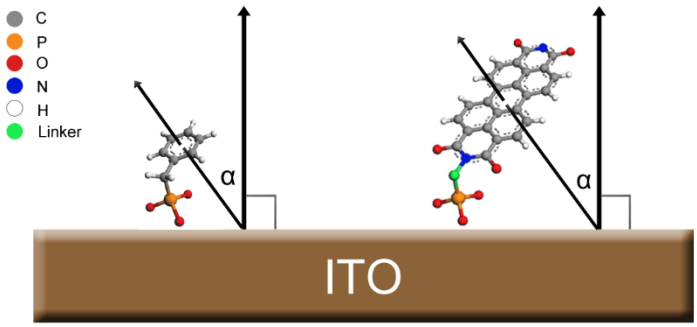

Figure 5.3: Cartoon structures of the benzyl phosphonic acids (left) and PDI-PAs (right) used in this study along with the definition of the tilt angle α.

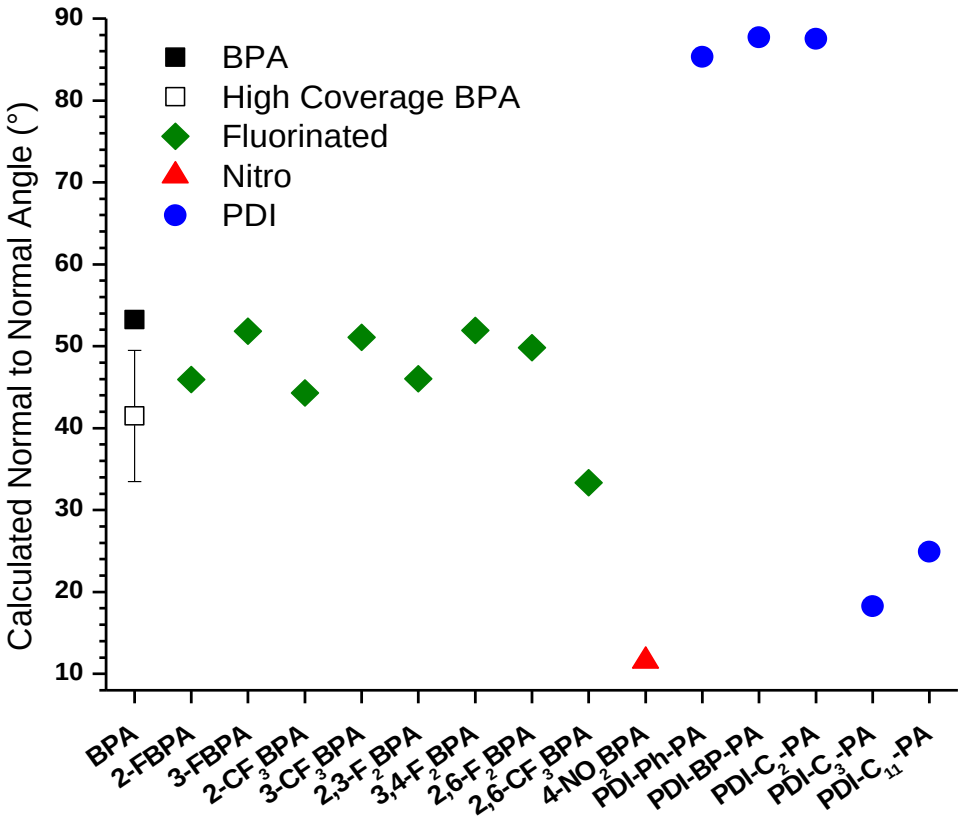

Figure 5.4: Graph of the tilt angle of the benzyl phosphonic acids from a single geometry optimized PA in binding site 1. The high coverage BPA case is presented as the average and standard deviation of the orientation of four modifiers in the same ITO unit cell in binding sites 1-4. The PDI-PA tilt angle values for the PDI in site 1 only are presented. The tilt angles for the PDI-PA in site 2, which are very close to the values in site 1, can be found in Table 5.1.

The orientations of the fluorinated BPA derivatives show a grouping of tilt angles between 44° and 52°, except for the 2,6-CF_3BPA (with a tilt angle of 33°), which is about 10° closer to the parallel orientation than the next closest fluorinated BPA. The nitro BPA is the most parallel one to the surface with an α value of 12°. The PDI PAs have two groupings, one standing almost perpendicular to the surface and the other more parallel to the surface. This can be rationalized by looking at the linkers between the PA binding group and the PDI. The phenyl, biphenyl, and C_2 linkers are enforcing an upright positioning of

the PDI, while the C_3 and C_{11} linkers with an odd number of carbons orient the PDI in a more lying down configuration.

Orientation has been shown to vary based on different binding geometries and different surface coverage.[20] Intermolecular interactions among densely packed surface modifiers may change the orientation of each modifier compared to less densely packed cases. Table 5.1 shows the tilt angles of all of the PA modifiers, including benzyl PA at higher coverage, with four PAs per ITO unit cell (1.1×10^{14} molecules/cm^2), and the PDI-PA modifiers, which are at twice the coverage of the fluorinated and nitro BPAs. The average tilt angle along with the standard deviation for the BPA at high coverage are shown in Figure 5.4. Since the average of the PDI-PA tilt angle results are nearly the same as the results for site 1 (see Table 5.1), only the tilt angle of the PDI in site 1 is presented in Figure 5.4. This also suggests weak intermolecular interactions between the PDI-PA modifiers in this case, which can be rationalized by large intermolecular distance between the PDI-PAs. In contrast, for the unmodified BPA, the 12° difference between the average orientation of the high coverage and its orientation in the low coverage case (in site 1) shows that intermolecular interactions can have a large effect on the molecular orientation, when the molecules become densely packed.

Table 5.1: Tilt angles for the phosphonic acids on ITO from geometry optimized atomic positions and from near-edge x-ray absorption fine structure spectroscopy (NEXAFS) measurements by Gliboff.[57] NEXAFS results are presented as the average with an uncertainty due to systematic errors in background subtraction and uncertainty of beam polarization. If the system does not specify a binding site, then the tilt angle presented is for the PA molecule in Site 1. Average tilt angles are presented as the average and standard deviation of the tilt angles. All values are in °.

System	Tilt Angle	Average Tilt Angle	NEXAFS Tilt Angles
1 BPA	53.26	----	47 ± 3
4 BPA Site 1	50.85	41.47 ± 8.01	
4 BPA Site 2	30.83		
4 BPA Site 3	43.30		
4 BPA Site 4	40.88		
2-FBPA	45.91	----	52 ± 2
3-FBPA	51.81	----	60 ± 2
2-CF_3BPA	44.30	----	59 ± 2
3-CF_3BPA	51.09	----	62 ± 3
2,3-F_2BPA	46.02	----	61 ± 3
3,4-F_2BPA	51.92	----	60 ± 2
2,6-F_2BPA	49.84	----	53 ± 4
2,6-CF_3BPA	33.32	----	50 ± 5
4-NO_2BPA	11.57	----	60 ± 3
2 PDI-Ph-PA Site 1	85.30	85.26 ± 0.06	----
2 PDI-Ph-PA Site 2	85.22		
2 PDI-BP-PA Site 1	87.69	87.70 ± 0.03	----
2 PDI-BP-PA Site 2	88.72		
2 PDI-C_2-PA Site 1	87.54	87.75 ± 0.29	----
2 PDI-C_2-PA Site 2	87.95		
2 PDI-C_3-PA Site 1	18.25	18.35 ± 0.14	----
2 PDI-C_3-PA Site 1	18.45		
2 PDI-C_{11}-PA Site 1	24.92	24.91 ± 0.01	----
2 PDI-C_{11}-PA Site 2	24.91		

Comparison between the calculated tilt angles and the NEXAFS tilt angles cannot be made without a reminder from Section 1.3.2 about NEXAFS. NEXAFS experiments are performed with collection of two different data sets at the same time, total electron yield (TEY) and Auger electron yield (AEY). While the angle of incidence is changed during the experiment, the maximum values of both TEY and AEY are recorded and then the respective points are each fit to a distribution given in Equation 1.6 to describe the tilt angle of the system. Since there will most likely be local variations of the tilt angle of the

molecules with respect to the surface normal, due to surface roughness or changes in binding configuration, the NEXAFS tilt angle is actually a convolution of the distribution of angles, specifically the expectation value of $\cos^2(\alpha)$.[58] The expectation value also means that if there is no order to the system, or if there are only random orientations of the molecules in the monolayer, the NEXAFS tilt angle will be 54.7°, denoted as the magic angle. In general, the farther away that the NEXAFS tilt angle is from the magic angle, the more the orientation can be trusted as the representation of the distribution of tilt angles for a well-ordered system. A well-ordered system should also show strong angular dependence in the measured peak areas, as shown in Figure 1.7a.

With this in mind, 2,6-F_2BPA represents a case where it is difficult to determine whether it adopts orientations close to the calculated and measured results, or if these molecules are largely disordered, because of the proximity to the magic angle. Many of the calculated tilt angles are on the other side of the magic angle with respect to the NEXAFS tilt angles, with 4-NO_2BPA showing the largest deviation between calculated and NEXAFS tilt angles. It is encouraging that when comparing the highest coverage BPA average tilt angle and the low coverage BPA (site 1) tilt angle to the NEXAFS value, that the highest coverage BPA case is closer to the NEXAFS value. The unmodified BPA case molecular coverage is expected to be on par with an optimal monolayer of the singly substituted BPAs, which are on the order of 2 - 4 × 10^{14} molecules/cm^2. This expectation means that this highest coverage BPA case is still not quite at the experimental molecular coverage obtained by XPS (see the next section), but it is closer than the low coverage BPA case. This indicates that molecular coverage and intermolecular interactions between the

molecules are important in the calculations, in order to better describe an actual surface modified system.

5.3.3 Estimated Optimal Coverage of Phosphonic Acids on ITO

As demonstrated both through theoretical calculations[20] and experimental characterizations,[59] the coverage of phosphonic acids has a strong impact on the work function modification of the ITO surface. In order to better understand the role that coverage plays in changing the orientation of the modifiers on the surface as well as the measured work function, the optimal coverage of the surface modifiers, that is, the coverage of a fully-packed, non-interacting, and spatially-limited molecular layer, is needed. Computing the optimal coverage values allows for a close examination of the role that sterics play in the ability of a phosphonic acid to modify a surface. Experimentally, coverage can be quantitatively determined using the ratio of peak areas of different element-specific excitations from XPS spectra.[56] Calculations can provide a projection of the PA onto the surface, using the geometry of the optimized PA, which may be extrapolated to form an optimal fully-packed monolayer. A comparison of the experimentally-derived (with XPS) coverage to the optimal monolayer coverage can give insight into the amount of intermolecular interactions for each PA system. Coverage values from XPS were calculated following the procedure described by Paniagua et al.[59-61] The calculated molecular footprint for each optimized phosphonic acid, the optimal coverage value (in molecules/cm^2) estimated using the calculated footprint, the percent coverage value obtained from the comparison of the experimentally-derived coverage to the optimal

coverage, the percent coverage in each calculation, and the experimental absolute coverage as translated from the percent coverage are summarized in Table 5.2.

Table 5.2: Comparison of phosphonic acid coverage values. The molecular footprints were calculated at the PBE level for surface-bound, geometry optimized phosphonic acids in site 1 on a slab of ITO. The optimal coverage values are obtained using the footprint of the phosphonic acid, the calculated percent coverage relates the coverage used in the calculations to the optimal coverage, and the experimental percent coverage values for the fluorinated PAs were obtained from Reference 56. The experimental percent coverage values can then be expressed in absolute terms of molecules/cm^2.

Phosphonic Acid	**Molecular Footprint (Å^2)**	**Ideal Coverage (10^{14} molecules/cm^2)**	**Calculated % Coverage**	**Experimental % Coverage**	**Experimental Coverage (10^{14} molecules/cm^2)**
BPA	22.54	4.44	6	----	----
2-FBPA	22.47	4.45	6	71	3.16
3-FBPA	20.57	4.86	6	78	3.80
2-CF_3BPA	29.04	3.44	8	78	2.69
3-CF_3BPA	31.25	3.20	9	91	2.91
2,3-F_2BPA	22.99	4.35	6	69	3.02
3,4-F_2BPA	20.56	4.86	6	78	3.80
2,6-F_2BPA	20.97	4.77	6	42	2.02
2,6-CF_3BPA	35.91	2.78	10	35	0.97
4-NO_2BPA	36.72	2.72	10	----	----
PDI-Ph-PA	41.92	2.39	24	----	----
PDI-BP-PA	37.97	2.63	22	----	----
PDI-C_2-PA	23.06	4.34	12	----	----
PDI-C_3-PA	118.98	0.84	68	----	----
PDI-C_{11}-PA	246.59	0.41	138	----	----

From Table 5.2, it becomes evident that, in general, fluorinated benzyl phosphonic acids produce experimental coverage values on the order of ~ 2 – 4 × 10^{14} molecules/cm^2 and are present at 70 – 90% of the ideal coverage. It is apparent that di-substitution in the more sterically hindered 2 *and* 6 positions leads to a dramatic decrease in the ability of the molecule to form a well-packed monolayer as shown by their low experimental percent coverage. It appears that these two modifiers in particular (2,6-F_2BPA and 2,6-CF_3BPA) are leaving a large amount of the ITO unmodified and thus potentially allowing for the

deposition of a far greater amount of adventitious contaminants on the surface. The nitro BPA leads to a smaller ideal coverage because the orientation of the PA is close to parallel with the surface, which takes up more surface area. PDI-PAs generally have larger footprints than the fluorinated BPAs examined here, because of the size of PDI compared to the benzene ring with any substituents, resulting in lower coverages.

If we compare fluorinated PAs with one withdrawing group, there is a clear trend in the experimental absolute coverage (number of molecules per area) observed for the molecules. The PA modifiers with the larger trifluoromethyl group have smaller experimental coverages than their counterparts with a fluoro group. This trend is not necessarily evident when looking at experimental percent coverage values. This is because the experimental percent coverage values take into account the differences in the molecular footprints of the modifiers. For instance, consider the case of 3-FBPA and 3-CF_3BPA. The 3-FBPA has a percent coverage value of 78 % and 3-CF_3BPA 91%; however, experimental coverage values are 3.80 and 2.91×10^{14} molecules/cm^2, respectively for 3-FBPA and 3-CF_3BPA. Thus, by looking at the higher coverage percentage, one might think that the 3-CF_3BPA would have a larger coverage, but this is not the case due to the differing molecular footprints of the PA modifiers. 3-CF_3BPA covers the surface more closely to an optimal monolayer than the 3-FBPA modifier, but there are more 3-FBPA modifiers present per unit area. It should be borne in mind that the percent coverage values are a comparison to the optimal monolayer and do not take into account the footprint, in order to obtain the total number of molecules present in a given area (experimental coverage). Thus, steric bulk and molecular footprint are interrelated in determining the coverage of a phosphonic acid on ITO.

5.3.4 Electronic Density of States

The electronic structure of the PAs can be examined by looking at the density of states projected onto atoms (PDOS). The PDOS for BPA, a fluoro and a trifluoromethyl substituted BPA, nitro BPA, and two PDI-PAs, one with an aromatic linker and the other with an alkyl linker, are shown below in Figure 5.5 and Figure 5.6. The PDOS of the atoms in the PA have been summed in order to give the total DOS of the PA modifier. The PDI-PAs have a different electronic structure than the fluorinated PAs, as seen by the broader, less intense peaks between 2.5 and 1 eV below the Fermi level energy (associated with the PDI fragment, see Figure 5.7) and electronic states being present at the Fermi level energy of the system. The presence of DOS at the Fermi level energy for the PDI-PA as well as the nitro-BPA systems is intriguing, and the charge densities corresponding to these states are found to distribute mainly on the phenyl linker for the PDI-Ph-PA and on the nitro group for the nitro-BPA (see Figure 5.6).

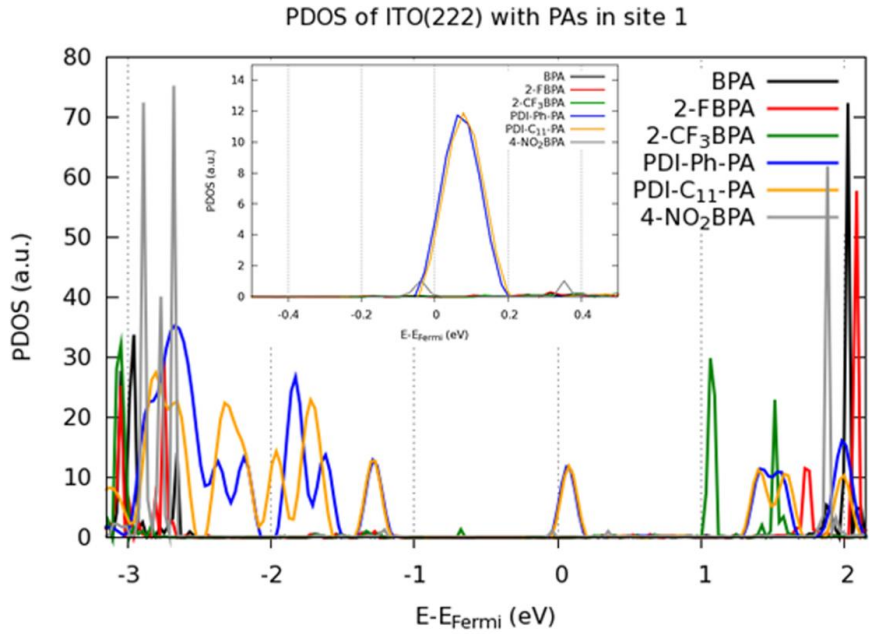

Figure 5.5: Graph of the projected density of states (PDOS) of representative phosphonic acids. Inset: PDOS zoomed in to show the range (E-E$_{Fermi}$) ± 0.5 eV.

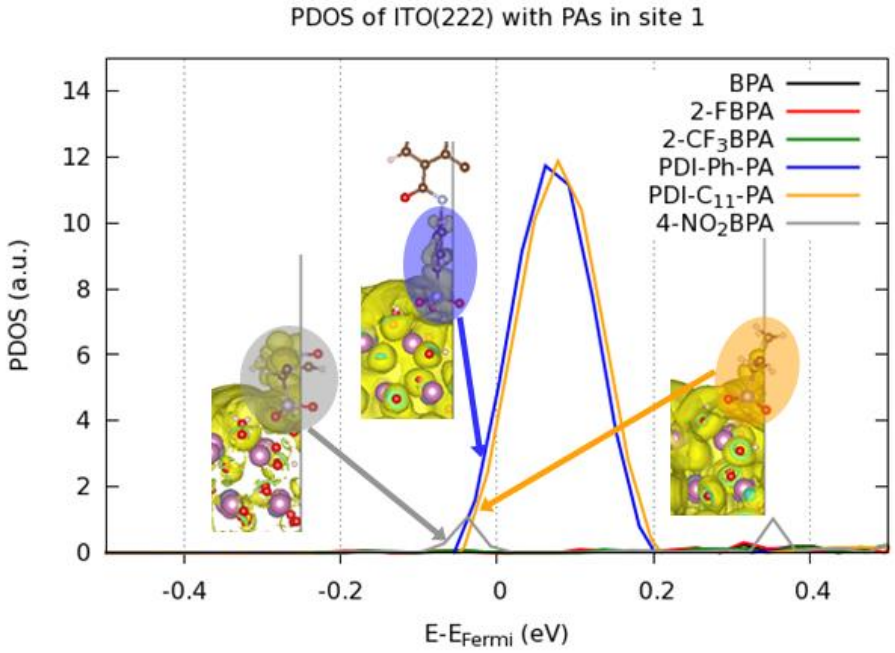

Figure 5.6: Graph of the projected density of states (PDOS) of representative phosphonic acid modifiers within 0.5 eV of the Fermi level energy. Insets: partial charge density plots for the PA modifier for the peaks just below the Fermi level energy. These show the nitro group and the linker of the PDI-PAs are responsible for these peaks.

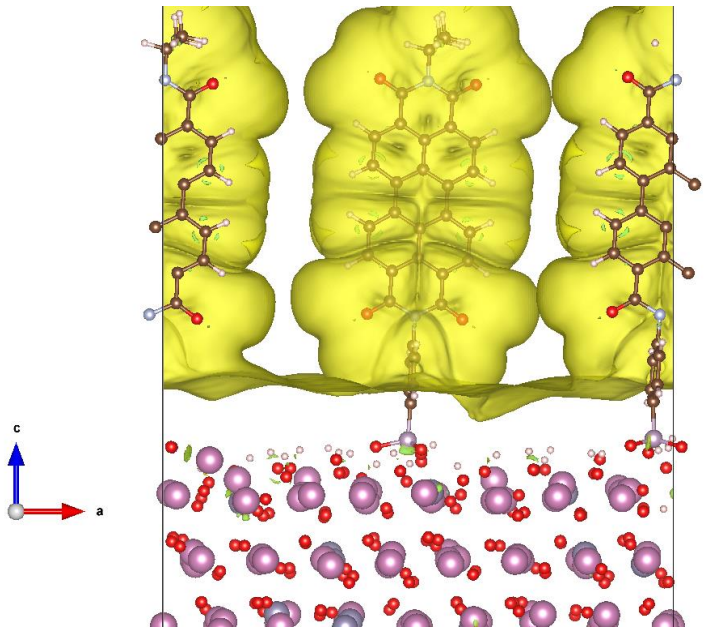

Figure 5.7: Partial charge density plot of PDI-Ph-PA for the energy range of 2.5 to 1 eV below the Fermi level energy, as shown in the projected density of states (PDOS) graph in Figure 5.5. The isosurface value is the same as the partial charge density plots presented in Figure 5.6.

While the molecules' DOS appear different in Figure 5.5, the contribution of the PA binding group (PO_3) in each molecule is found to be similar regardless of the rest of the molecule. The summed DOS of the phosphorus and three oxygen atoms of the PO_3 binding group, from each PA molecule in Figure 5.5 are shown in Figure 5.8, where we can see they do not have contribution within a large energy regime near the Fermi level energy, especially to the states crossing the Fermi level energy shown in Figure 5.5.

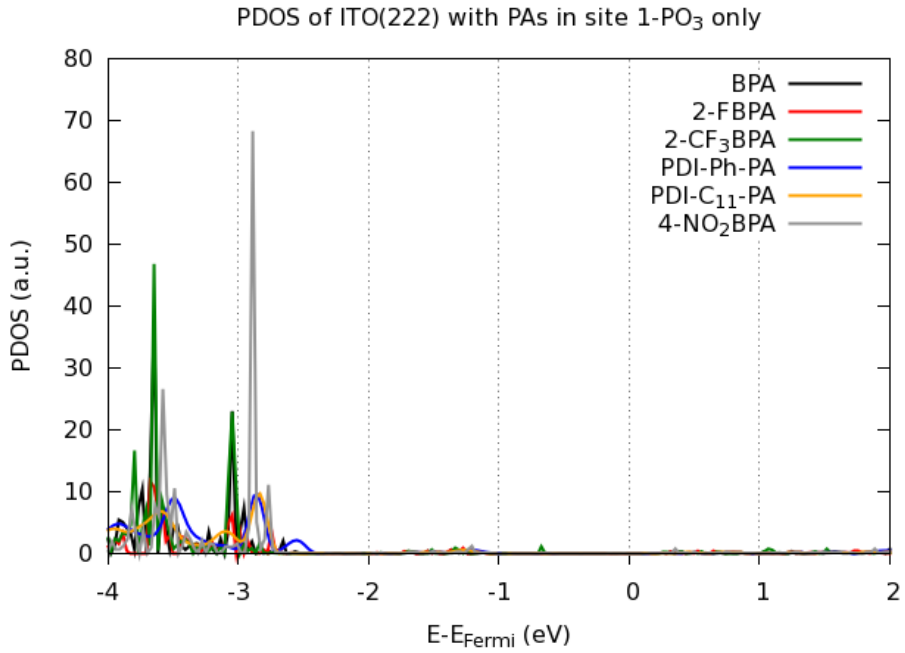

Figure 5.8: Graph of the projected density of states (PDOS) of the PO_3 binding group of representative phosphonic acid modifiers.

5.3.5 Work Function Modification of the PAs

The work function (Φ) of a bare or modified surface is calculated using Equation 1.1. The work function of the completely hydroxylated ITO surface considered here is 3.15 eV, which is substantially smaller than the experimental results that are in the range 4.0 – 6.1 eV.[62-65] We note that the experimental value is sensitive to preparation conditions and nature of measurements;[62-65] also, when the surface OH coverage is reduced to 1/6 of the current value (6.76×10^{14} /cm^2), the calculated work function of the model ITO surface reaches 4.24 eV.[66] We have shown earlier that, in spite of the low value of the calculated Φ for ITO, the work-function modifications upon deposition of various monolayers on the surface were reproduced accurately.[18] The calculated and experimental UPS[56] WF measurements for the PA modified ITO can be found below in Figure 5.9 and Table 5.3. It

should be noted that the coverage is twice as large for the PDI-PA systems as in the BPA systems, so caution should be used before direct comparisons can be made. It should also be noted that the coverage in the calculations is usually around 10 times lower than the experimental coverage (see Table 5.2). If calculations were performed at coverages closer to the experimental coverage, it is expected that there would be larger depolarization, as mentioned in Section 3.3.2.

Figure 5.9 shows that most of these fluorinated BPAs increased the work function up to 0.2 eV, while the 2-CF_3BPA and 2,6-F_2BPA were able to lower the work function by up to 0.07 eV. The nitro BPA was able to increase the work function of ITO by about 0.4 eV, which is twice as much as the fluorinated BPAs. The PDI-PAs had the greatest change in work function, with increases in work function calculated to be between 1 – 1.4 eV. It should be noted again that the coverage is twice as large for the PDI-PA systems as in the BPA systems. If half of the values of the work function increase for the PDI-PA systems are taken, the PDI-PAs still cause the greatest increase in work function of any of the PAs studied. The WF values presented in Figure 5.9 and Table 5.3 agree with previously published values for fluorinated BPAs.[3-4, 6, 12, 18, 30, 32-33] While the Φ values are systematically smaller than the experimental values, due to the much lower coverage used in the calculations, the calculated work functions appear to follow a similar trend, with a few exceptions. For instance, 2-FBPA and 2-CF_3BPA have rather noticeable changes from the experimental results. In the calculations, 2-FBPA leads to almost no change from the unmodified ITO surface, while UPS measurements showed that Φ increased by about 0.2 eV. 2-CF_3BPA lead to a 0.1 eV decrease of the work function in calculations, while an increase of about 0.2 eV was observed experimentally.

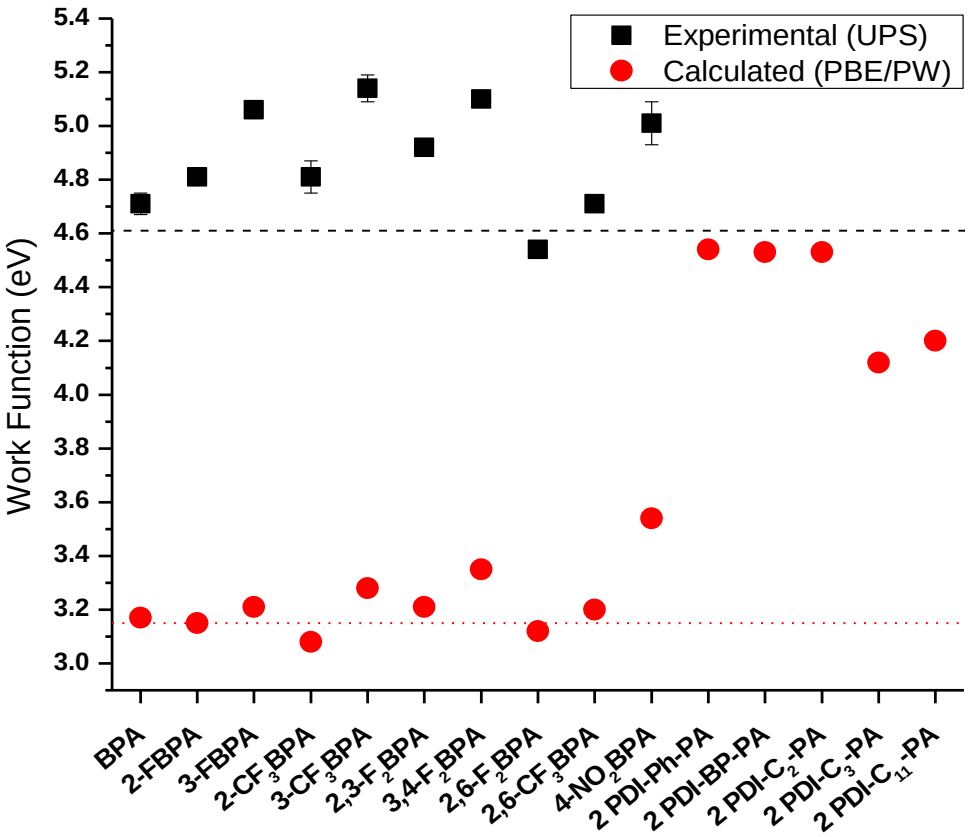

Figure 5.9: Graph of the experimental and calculated work function of ITO surface after modification with PA modifiers. UPS measurements are from Reference 56. The error bars in the experimental results represent the standard deviation from UPS measurements of at least 5 different spots on the surface. The lines represent the work function of the detergent solvent cleaned (DSC) ITO (black, dashed) and bare ITO (red, dotted) for the experimental and calculated results, respectively.

A decomposition scheme, discussed extensively in our earlier work,[20, 38] can be used to gain a better understanding of the factors leading to the total work function change. The $\Delta\Phi$ of the surfaces due to the adsorption of a molecular layer can be decomposed into three terms, as described in Equation 1.5, where $\Delta V_{int.dip.}$ is the contribution of the dipole formed at the very interface between molecular layer and surface; $\Delta V_{mol.}$ is the electrostatic potential energy change across an isolated molecular layer in vacuum; and $\Delta V_{geom.}$ is the work function change of the bare surface due to geometric relaxations when interacting with a layer of PA modifiers. All these terms are collected in Table 5.3. If these respective

values for the PDI systems are halved, the values for the geometrical rearrangement of the surface ($\Delta V_{geom.}$) and the potential drop across the isolated molecular layer ($\Delta V_{mol.}$) are now on the same order of magnitude as their corresponding components in the BPA systems. Since the components due to surface rearrangement and isolated molecular layers are about the same in the fluorinated, nitro, and PDI-PA systems, there must be some inherent difference in these substituents causing the observed differences in the interface dipole component of the work function. If we look at the Bader charges in Table 5.3, there appears to be a trend in the magnitude of the Bader charge and the electron withdrawing group strength. The unmodified and fluorinated BPAs have charge transfer on the order of 0.19 – 0.24 |e|, which then increases to 0.31 |e| with the stronger nitro group, and increases further to 0.5 – 0.8 |e| for the two PDI-PAs, which are the strongest electron-withdrawing groups examined in this study.

Figure 5.10 shows the plane-averaged electron charge-density difference, $\Delta\rho$, for 4-NO_2BPA and 2 PDI-Ph-PAs on ITO, along with the optimized geometries. The charge-density difference was calculated by subtracting from the charge density of the combined ITO-PA system the charge density of each component (PA and ITO) at the geometry it is calculated to have after interaction with the other component. In order to calculate the true charge density of the PA, the bonds between the oxygen atoms of the PO_3 binding group and indium or tin atoms of the ITO surface were cleaved and a hydrogen atom was added to two of the three oxygen atoms, returning the PA to a neutral molecule. The newly added hydrogen atoms were then allowed to relax, while the rest of the molecule was held fixed in the optimized geometry. Then, each of the two hydrogen atoms (per PA) were isolated and the charge density of each hydrogen was subtracted from the neutral, hydrogenated PA

system. Comparing the plane-averaged charge density difference for the nitro-BPA and PDI-Ph-PA (Figure 5.10), we observe that the charge accumulation on the latter extends largely into the long PDI fragments, which finally lead to much larger interface-dipole contribution than the nitro-BPA. Thus, although the contributions of the molecular dipole are small for both cases (though in opposite directions, see Table 5.3), the contribution of the interface dipole in the PDI-Ph-PA, which has a much larger conjugated head-group than the nitro-BPA, and thus more delocalized charge transfer, leads to a much larger work-function change. Furthermore, the discovery here also shows that the electrostatic potential change induced by the interface dipole can be delocalized over a large space crossing a physically thin interface.

Table 5.3: Experimental and calculated Φ measurements, calculated ΔΦ, work function breakdown and Bader charge of the surface modifier, without the PO_3 binding group.

System	UPS Φ [a,b] (eV)	Calc. Φ (eV)	Calc. ΔΦ (eV)	$\Delta V_{int.\ dip.}$ (eV)	$\Delta V_{geom.}$ (eV)	$\Delta V_{mol.}$ (eV)	Bader Charge (|e|)
ITO(222) [c]	4.62 ± 0.02	3.15	----	----	----	----	----
BPA	4.71 ± 0.04	3.17	0.02	0.12	-0.10	-0.06	-0.19
2-FBPA	4.81 ± 0.01	3.15	0.00	0.14	-0.08	-0.12	-0.20
3-FBPA	4.80 ± 0.01	3.21	0.06	0.13	-0.08	-0.03	-0.21
2-CF_3BPA	4.81 ± 0.06	3.08	-0.07	0.14	-0.08	-0.18	-0.22
3-CF_3BPA	5.14 ± 0.05	3.28	0.13	0.15	-0.10	0.02	-0.21
2,3-F_2BPA	4.92 ± 0.02	3.21	0.06	0.15	-0.10	-0.06	-0.21
3,4-F_2BPA	5.10 ± 0.01	3.35	0.20	0.14	-0.09	0.10	-0.21
2,6-F_2BPA	4.54 ± 0.01	3.12	-0.03	0.13	-0.10	-0.13	-0.21
2,6-CF_3BPA	4.71 ± 0.02	3.20	0.05	0.14	-0.10	-0.06	-0.24
4-NO_2BPA	5.01 ± 0.08	3.54	0.39	0.26	-0.12	0.18	-0.31
2 PDI-Ph-PA	----	4.54[d]	1.39[d]	1.78[d]	-0.21[d]	-0.17[d]	-0.74[e]
2 PDI-BP-PA	----	4.53[d]	1.38[d]	1.56[d]	-0.18[d]	0.02[d]	-0.79[e]
2 PDI-C_2-PA	----	4.53[d]	1.38[d]	1.79[d]	-0.17[d]	-0.25[d]	-0.77[e]
2 PDI-C_3-PA	----	4.12[d]	0.97[d]	1.56[d]	-0.26[d]	-0.34[d]	-0.81[e]
2 PDI-C_{11}-PA	----	4.20[d]	1.05[d]	1.47[d]	-0.31[d]	-0.18[d]	-0.52[e]

[a] Reference 56 [b] Values are obtained from an average of at least 5 spots on each substrate and standard deviation is the variation in WF from spot to spot. [c] Experimentally, the ITO work function is from a detergent solvent cleaned (DSC) sample. [d] Data is presented from calculations with 2 PDI-PAs in the same unit cell. [e] Sum of the Bader charges for both PDI-PAs in the same unit cell.

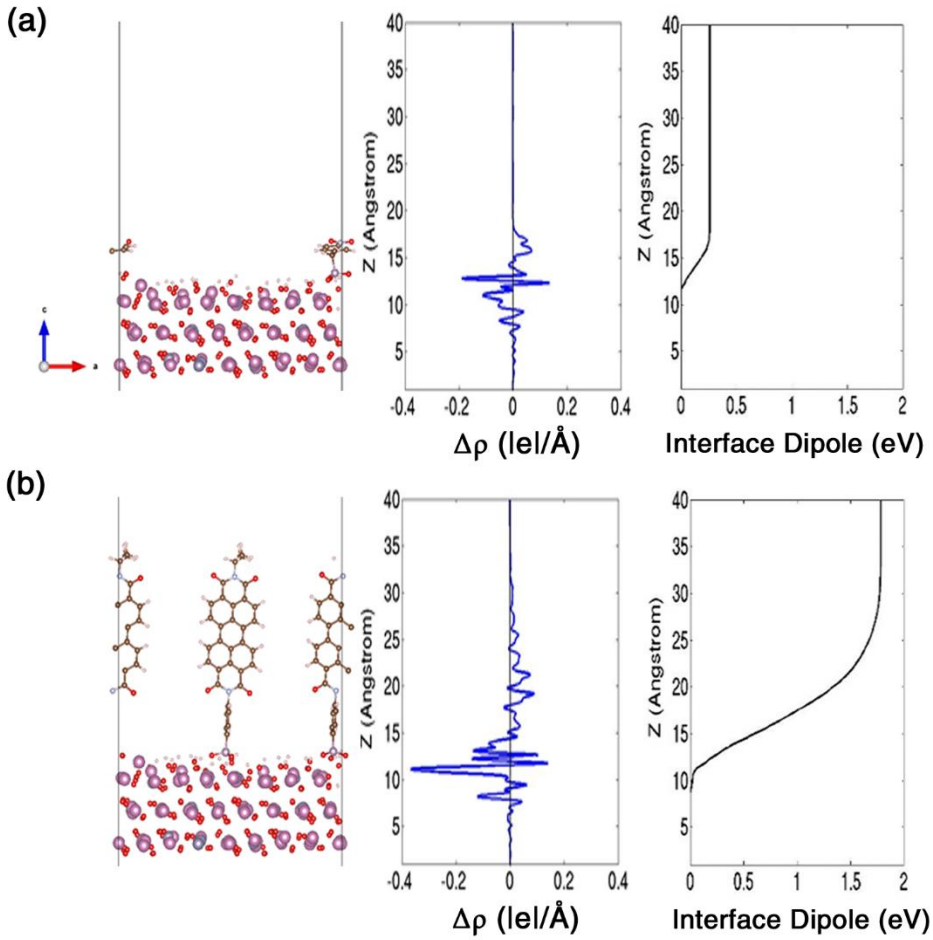

Figure 5.10: Optimized structures, plane-averaged change in charge density (Δρ) (shown in blue), and interface dipole (shown in black) for (a) 4-NO_2BPA and (b) 2 PDI-Ph-PAs on ITO. Negative Δρ corresponds to an increased positive charge relative to the bare ITO and isolated PAs, whereas positive Δρ corresponds to increased negative charge.

Much of the previous work into PA modifiers has focused on using electron-withdrawing substituents, such as fluorine atoms and trifluoromethyl groups, on the core away from the PA binding group in order to lead to an increase of the vacuum level on that side of the dipolar layer, thus increasing the work function.[3-5, 12, 18, 27, 32-33, 58, 67] This can be generalized for dipolar modifiers in that the magnitude and direction of the dipole moment of the molecular layer are related to the amount of ΔΦ observed. ΔV_{mol}, by the way it is

calculated, is intimately related to the dipole of the molecular layer, as shown in Equation 5.2:[68]

$$\Delta V_{\text{mol}} = \frac{e\,\mu_{\perp}}{\varepsilon_0 A} \tag{5.2}$$

where e is the fundamental charge, $\mu_{\perp}$ is the dipole moment of the molecular layer perpendicular to the surface, ε_0 is the vacuum permittivity, and A is the area of the unit cell. In order to test how these systems compare to the literature trend, dipole moments of the PAs were calculated at the optimized geometries of the PA on the ITO surface. The dipole moments were calculated for the neutral, hydrogenated PAs, with a similar procedure to produce these neutral PAs as described for the charge density difference, without the final charge density calculation step. The dipole moment reported is the calculated component which is parallel to the z-axis of the unit cell, or $\mu_{\perp}$ from Equation 5.2, in all cases. The dipole moments of the PAs are shown below in Figure 5.11a along with a cartoon denoting the dipole convention while comparing the BPAs calculated here to phenyl phosphonic acids examined in the literature (Figure 5.11b).

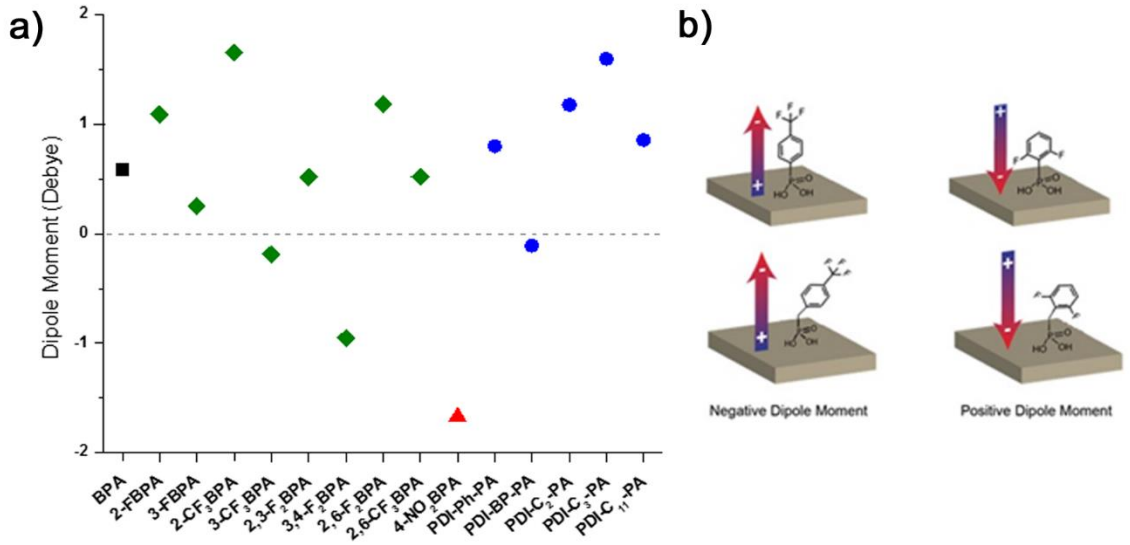

Figure 5.11: Graph of the portion of the dipole moment perpendicular to the surface of the PAs examined in this study (a) and a cartoon of the dipole moment convention used along with a comparison between the benzyl PAs examined here and the phenyl PAs examined previously, showing the extra rotational degree of freedom in benzyl PAs. (b)

When the dipole moment data are plotted versus the calculated $\Delta\Phi$ as in Figure 5.12, there seems to be some different trends that appear. Again, due to the different coverages, the PDI-PAs have been plotted with half of the dipole moment and half of the calculated $\Delta\Phi$, for a better comparison to the benzyl PA systems. The fluorinated BPAs show a strong correlation between stronger dipole moments pointing away from the surface with larger increases in work function. The nitro BPA is similar to, but does not align with the fluorinated BPA trend. The PDI-PAs have an entirely different behavior than the fluorinated or nitro BPAs. There is almost no dependence of the calculated change in work function upon the dipole moment. Bader charges of these PA modifiers, without the PO_3 binding groups (see Table 5.3), show that the nitro BPA has more charge transferred to the modifier than the fluorinated BPA systems. Also, half of the PDI-PAs Bader charges still indicates more charge transfer than the fluorinated BPA systems and is on par with or

greater than the nitro BPA case. It appears that the stronger electron-withdrawing nitro and PDI substituents are undergoing much stronger charge transfer from the surface than the fluorinated BPA systems and this charge transfer seems to be part of the reason why these systems do not follow the fluorinated BPA trend seen here and in the literature. Since the interface dipole component of the work function modification breakdown is associated with charge transfer, the "cushion" effect,[69] and/or redistribution at the interface, the largely increased charge transfer in the nitro and PDI systems should lead to larger interface dipole contributions (see the discussion about Figure 5.10) which has been confirmed by our computational results.

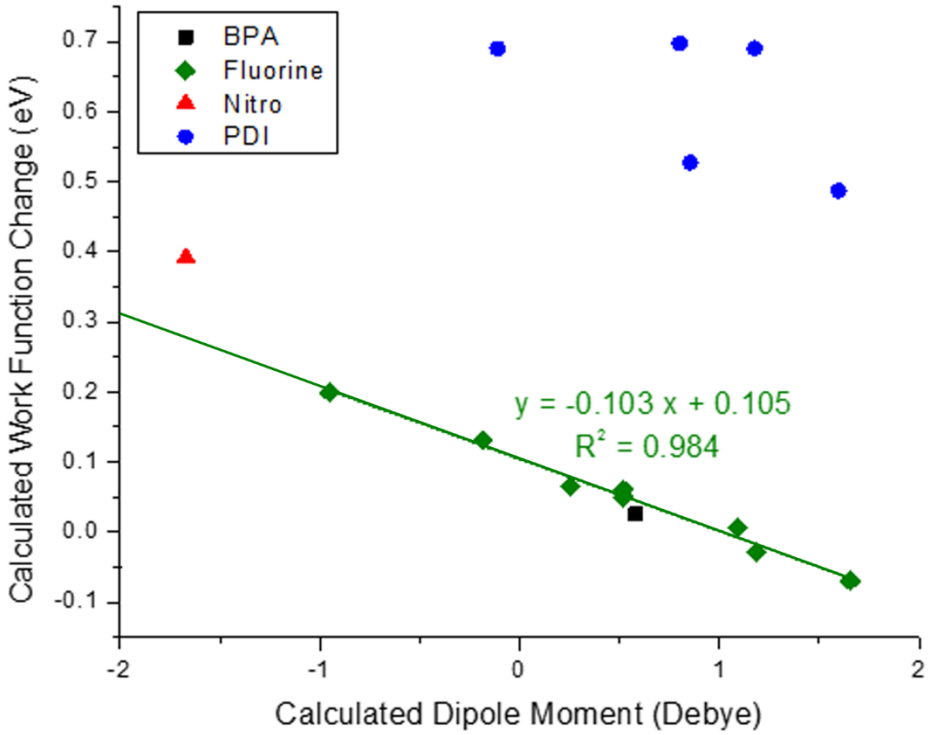

Figure 5.12: Graph of the calculated work function change versus calculated dipole moment. The trend line has been manually extended to the y-axis to give an easier comparison of the Nitro BPA to the fluorinated BPA trend.

5.4 Conclusions

We have investigated the effects of PA surface modifiers with a variety of electron-withdrawing substituents when deposited on the surface of ITO, on the work function, coverage, and molecular ordering. The work function of ITO can be drastically varied based on judicious selection of the electron withdrawing group. DFT calculations and experimental results corroborate the impact of these modifiers on the surface of ITO, as the trends for WF modification of the surface fit well with one another. It was also shown that the work function of ITO is not greatly decreased by any of the phosphonic acids discussed within this study, and that steric hindrance likely plays a key role in determining the overall ability of a phosphonic acid to form a complete monolayer. In general, however, the majority of fluorinated benzyl phosphonic acids form a rather dense monolayer on the surface of ITO as shown by XPS. While it is not a complete monolayer, XPS indicated that the monolayer was 70 – 90 % of an ideal monolayer. The calculated results indicate that most of the tilt angles for the fluorinated BPAs were within a range of approximately 10° from one another. The PDI-PAs had two major orientations with one standing perpendicular and the other more parallel to the surface, depending on the structure of linker between the PDI and the binding group. No direct relationship was found between the measured tilt angle and the molecular coverage or work function modification.

The fluorinated BPAs generally follow the trend that the dipole moment primarily determines the amount of work function modification. However, the dipole moment is not *the* determining factor for work function modification for PAs that trigger significant charge transfer from the surface, as in the nitro BPA and PDI-PAs. Thus, nitro-benzyl and

PDI phosphonic acids have proven to be far more complex systems than what was previously examined with phenyl and alkyl phosphonic acids.

5.5 References

1. Liu, S.-W.; Lee, C.-C.; Wu, K.-Y.; Huang, J.-C.; Su, W.-C.; Lin, C.-F.; Chen, C.-T.; Tao, Y.-T.; Lee, J.-H. "Stamped Self-Assembled Monolayers on Electrode for Connecting Organic Light-Emitting Diode and Organic Photovoltaic Device." *J. Disp. Technol.* **2011,** *7* (5), 229-234.

2. Hanson, E. L.; Guo, J.; Koch, N.; Schwartz, J.; Bernasek, S. L. "Advanced Surface Modification of Indium Tin Oxide for Improved Charge Injection in Organic Devices." *J. Am. Chem. Soc.* **2005,** *127*, 10058-10062.

3. Sharma, A.; Haldi, A.; Hotchkiss, P. J.; Marder, S. R.; Kippelen, B. "Effect of phosphonic acid surface modifiers on the work function of indium tin oxide and on the charge injection barrier into organic single-layer diodes." *J. Appl. Phys.* **2009,** *105*, 074511(1-6).

4. Sharma, A.; Hotchkiss, P. J.; Marder, S. R.; Kippelen, B. "Tailoring the work function of indium tin oxide electrodes in electrophosphorescent organic light-emitting diodes." *J. Appl. Phys.* **2009,** *105*, 084507(1-6).

5. Sharma, A.; Kippelen, B.; Hotchkiss, P. J.; Marder, S. R. "Stabilization of the work function of indium tin oxide using organic surface modifiers in organic light-emitting diodes." *Appl. Phys. Lett.* **2008,** *93*, 163308(1-3).

6. MacLeod, B. A.; Horwitz, N. E.; Ratcliff, E. L.; Jenkins, J. L.; Armstrong, N. R.; Giordano, A. J.; Hotchkiss, P. J.; Marder, S. R.; Campbell, C. T.; Ginger, D. S. "Built-In Potential in Conjugated Polymer Diodes with Changing Anode Work Function: Interfacial States and Deviation form the Schottky-Mott Limit." *J. Phys. Chem. Lett.* **2012,** *3*, 1202-1207.

7. Knesting, K. M.; Hotchkiss, P. J.; MacLeod, B. A.; Marder, S. R.; Ginger, D. S. "Spatially Modulating Interfacial Properties of Transparent Conductive Oxides: Patterning Work Function with Phosphonic Acid Self-Assembled Monolayers." *Adv. Mater.* **2012,** *24*, 642-646.

8. Miozzo, L.; Yassar, A.; Horowitz, G. "Surface engineering for high performance organic electronic devices: the chemical approach." *J. Mater. Chem.* **2010,** *20*, 2513-2538.

9. Cheng, X.; Noh, Y.-Y.; Wang, J.; Tello, M.; Frisch, J.; Blum, R.-P.; Vollmer, A.; Rabe, J. P.; Koch, N.; Sirringhaus, H. "Controlling Electron and Hole Charge Injection in Ambipolar Organic Field-Effect Transistors by Self-Assembled Monolayers." *Adv. Funct. Mater.* **2009,** *19*, 2407-2415.

10. Beaumont, N.; Hancox, I.; Sullivan, P.; Hatton, R. A.; Jones, T. S. "Increased efficiency in small molecule organic photovoltaic cells through electrode modification with self-assembled monolayers." *Energy Environ. Sci.* **2011,** *4*, 1708-1711.

11. Bulliard, X.; Ihn, S.-G.; Yun, S.; Kim, Y.; Choi, D.; Choi, J.-Y.; Kim, M.; Sim, M.; Park, J.-H.; Choi, W.; Cho, K. "Enhanced Performance in Polymer Solar Cells by Surface Energy Control." *Adv. Funct. Mater.* **2010,** *20*, 4381-4387.

12. Paniagua, S. A.; Hotchkiss, P. J.; Jones, S. C.; Marder, S. R.; Mudalige, A.; Marrikar, F. S.; Pemberton, J. E.; Armstrong, N. R. "Phosphonic Acid Modification of Indium-Tin Oxide Electrodes: Combined XPS/UPS/Contact Angle Studies." *J. Phys. Chem. C* **2008,** *112*, 7809-7817.

13. Besbes, S.; Ltaief, A.; Reybier, K.; Ponsonnet, L.; Jaffrezic, N.; Davenas, J.; Ben Ouda, H. "Injection modifications by ITO functionalization with a self-assembled monolayer in OLEDs." *Synth. Met.* **2003,** *138*, 197-200.

14. Coffey, D. C.; Ginger, D. S. "Patterning Phase Separation in Polymer Films with Dip-Pen Nanolithography." *J. Am. Chem. Soc.* **2005,** *127*, 4564-4565.

15. DeLongchamp, D. M.; Kline, R. J.; Fischer, D. A.; Richter, L. J.; Toney, M. F. "Molecular Characterization of Organic Electronic Films." *Adv. Mater.* **2011,** *23*, 319-337.

16. Park, L. Y.; Munro, A. M.; Ginger, D. S. "Controlling Film Morphology in Conjugated Polymer:Fullerene Blends with Surface Patterning." *J. Am. Chem. Soc.* **2008,** *130*, 15916-15926.

17. Wei, J. H.; Coffey, D. C.; Ginger, D. S. "Nucleating Pattern Formation in Spin-Coated Polymer Blend Films with Nanoscale Surface Templates." *J. Phys. Chem. B* **2006,** *110*, 24324-24330.

18. Hotchkiss, P. J.; Li, H.; Paramonov, P. B.; Paniagua, S. A.; Jones, S. C.; Armstrong, N. R.; Brédas, J.-L.; Marder, S. R. "Modification of the Surface Properties of Indium Tin Oxide with Benzylphosphonic Acids: A Joint Experimental and Theoretical Study." *Adv. Mater.* **2009,** *21*, 4496-4501.

19. Hatton, R. A.; Day, S. R.; Chesters, M. A.; Willis, M. R. "Organic electroluminescent devices: enhanced carrier injection using an organosilane self assembled monolayer (SAM) derivatized ITO electrode." *Thin Solid Films* **2001,** *394*, 291-296.

20. Li, H.; Paramonov, P. B.; Brédas, J.-L. "Theoretical study of the surface modification of indium tin oxide with trifluorophenyl phosphonic acid molecules: impact of coverage density and binding geometry." *J. Mater. Chem.* **2010,** *20*, 2630-2637.

21. Schulmeyer, T.; Paniagua, S. A.; Veneman, P. A.; Jones, S. C.; Hotchkiss, P. J.; Mudalige, A.; Pemberton, J. E.; Marder, S. R.; Armstrong, N. R. "Modification of $BaTiO_3$ thin films: adjustment of the effective surface work function." *J. Mater. Chem.* **2007,** *17*, 4563-4570.

22. Hotchkiss, P. J.; Malicki, M.; Giordano, A. J.; Armstrong, N. R.; Marder, S. R. "Characterization of phosphonic acid binding to zinc oxide." *J. Mater. Chem.* **2011,** *21*, 3107-3112.

23. Vericat, C.; Vela, M. E.; Benitez, G.; Carro, P.; Salvarezza, R. C. "Self-assembled monolayers of thiols and dithiols on gold: new challenges for a well-known system." *Chem. Soc. Rev.* **2010,** *39*, 1805-1834.

24. Xia, Y.; Zhao, X.-M.; Whitesides, G. M. "Pattern transfer: Self-assembled monolayers as ultrathin resists." *Microelectron. Eng.* **1996,** *32*, 255-268.

25. Losego, M. D.; Guske, J. T.; Efremenko, A.; Maria, J.-P.; Franzen, S. "Characterizing the Molecular Order of Phosphonic Acid Self-Assembled Monolayers on Indium Tin Oxide Surfaces." *Langmuir* **2011,** *27*, 11883-11888.

26. Gliboff, M.; Sang, L.; Knesting, K. M.; Schalnat, M. C.; Mudalige, A.; Ratcliff, E. L.; Li, H.; Sigdel, A. K.; Giordano, A. J.; Berry, J. J.; Nordlund, D.; Seidler, G. T.; Brédas, J.-L.; Marder, S. R.; Pemberton, J. E.; Ginger, D. S. "Orientation of Phenylphosphonic Acid Self-Assembled Monolayers on a Transparent Conductive Oxide: A Combined NEXAFS, PM-IRRAS, and DFT Study." *Langmuir* **2013,** *29*, 2166-2174.

27. Hotchkiss, P. J.; Jones, S. C.; Paniagua, S. A.; Sharma, A.; Kippelen, B.; Armstrong, N. R.; Marder, S. R. "The Modification of Indium Tin Oxide with Phosphonic Acids: Mechanism of Binding, Tuning of Surface Properties, and Potential for Use in Organic Electronic Applications." *Acc. Chem. Res.* **2012,** *45*, 337-346.

28. Paniagua, S. A.; Giordano, A. J.; Smith, O. N. L.; Barlow, S.; Li, H.; Armstrong, N. R.; Pemberton, J. E.; Brédas, J.-L.; Ginger, D.; Marder, S. R. "Phosphonic Acids for Interfacial Engineering of Transparent Conductive Oxides." *Chem. Rev.* **2016,** *116* (12), 7117-7158.

29. Koh, S. E.; McDonald, K. D.; Holt, D. H.; Dulcey, C. S.; Chaney, J. A.; Pehrsson, P. E. "Phenylphosphonic Acid Functionalization of Indium Tin Oxide: Surface Chemistry and Work Functions." *Langmuir* **2006,** *22*, 6249-6255.

30. Lacher, S.; Matsuo, Y.; Nakamura, E. "Molecular and Supramolecular Control of the Work Function of an Inorganic Electrode with Self-Assembled Monolayer of Umbrella-Shaped Fullerene Derivatives." *J. Am. Chem. Soc.* **2011,** *133* (42), 16997-17004.

31. Jee, S. H.; Kim, S. H.; Ko, J. H.; Yoon, Y. S. "Study on Work Function Change of ITO Modified by Using a Self-Assembled Monolayer for Organic based Devices." *J. Korean Phys. Soc.* **2006,** *49* (5), 2034-2039.

32. Ratcliff, E. L.; Garcia, A.; Paniagua, S. A.; Cowan, S. R.; Giordano, A. J.; Ginley, D. S.; Marder, S. R.; Berry, J. J.; Olson, D. C. "Investigating the Influence of Interfacial Contact Properties on Open Circuit Voltages in Organic Photovoltaic Performance: Work Function Versus Selectivity." *Adv. Energy Mater.* **2013,** *3* (5), 647-656.

33. Sharma, A.; Haldi, A.; Potscavage Jr., W. J.; Hotchkiss, P. J.; Marder, S. R.; Kippelen, B. "Effects of surface modification of indium tin oxide electrodes on the performance of molecular multilayer organic photovoltaic devices." *J. Mater. Chem.* **2009,** *19*, 5298-5302.

34. Bardecker, J. A.; Ma, H.; Kim, T.; Huang, F.; Liu, M. S.; Cheng, Y.-J.; Ting, G.; Jen, A. K.-Y. "Self-assembled Electroactive Phosphonic Acids on ITO: Maximizing Hole-Injection in Polymer Light-Emitting Diodes." *Adv. Funct. Mater.* **2008,** *18* (24), 3964-3971.

35. Wang, H.; Gomez, E. D.; Guan, Z.; Jaye, C.; Toney, M. F.; Fischer, D. A.; Kahn, A.; Loo, Y.-L. "Tuning Contact Recombination and Open-Circuit Voltage in Polymer Solar Cells via Self-Assembled Monolayer Adsorption at the Organic–Metal Oxide Interface." *J. Phys. Chem. C* **2013,** *117* (40), 20474-20484.

36. Romaner, L.; Heimel, G.; Zojer, E. "Electronic structure of thiol-bonded self-assembled monolayers: Impact of coverage." *Phys. Rev. B: Condens. Matter Mater. Phys.* **2008,** *77*, 045113(1-9).

37. Alloway, D. M.; Graham, A. L.; Yang, X.; Mudalige, A.; Colorado, J., Ramon; ; Wysocki, V. H.; Pemberton, J. E.; Lee, T. R.; Wysocki, R. J.; Armstrong, N. R. "Tuning the Effective Work Function of Gold and Silver Using ω-Functionalized Alkanethiols: Varying Surface Composition through Dilution and Choice of Terminal Groups." *J. Phys. Chem. C* **2009,** *113*, 20328-20334.

38. Wood, C.; Li, H.; Winget, P.; Brédas, J.-L. "Binding Modes of Fluorinated Benzylphosphonic Acids on the Polar ZnO Surface and Impact on Work Function." *J. Phys. Chem. C* **2012,** *116*, 19125-19133.

39. Crispin, X.; Geskin, V.; Crispin, A.; Cornil, J.; Lazzaroni, R.; Salaneck, W. R.; Brédas, J.-L. "Characterization of the Interface Dipole at Organic/Metal Interfaces." *J. Am. Chem. Soc.* **2002,** *124*, 8131-8141.

40. Appleyard, S. F. J.; Willis, M. R. "Electroluminescence: enhanced injection using ITO electrodes coated with a self assembled monolayer." *Opt. Mater.* **1998,** *9*, 120-124.

41. Koch, N. "Energy levels at interfaces between metals and conjugated organic molecules." *J. Phys.: Condens. Matter* **2008,** *20*, 184008-184019.

42. Lu, Z.; Jiang, B.; Zhang, X.; Tang, A.; Chen, L.; Zhan, C.; Yao, J. "Perylene-Diimide Based Non-Fullerene Solar Cells with 4.34% Efficiency through Engineering Surface Donor/Acceptor Compositions." *Chem. Mater.* **2014,** *26*, 2907-2914.

43. Zhan, X.; Tan, Z. a.; Domercq, B.; An, Z.; Zhang, X.; Barlow, S.; Li, Y.; Zhu, D.; Kippelen, B.; Marder, S. R. "A High-Mobility Electron-Transport Polymer with Broad Absorption and Its Use in Field-Effect Transistors and All-Polymer Solar Cells." *J. Am. Chem. Soc.* **2007,** *129*, 7246-7247.

44. Ichikawa, M.; Deguchi, S.; Onoguchi, T.; Jeon, H.-G.; de Romeo Banoukepa, G. "N,N'-diphenylperylene diimide functioning as a sensitizing light absorber based on excitation transfer for organic thin-film solar cells." *Org. Electron.* **2013,** *14*, 464-468.

45. Shi, M.-M.; Tung, V. C.; Nie, J.-J.; Chen, H.-Z.; Yang, Y. "Bulky rigid substitutions: A route to high electron mobility and high solid-state luminescence efficiency of perylene diimide." *Org. Electron.* **2014,** *15*, 281-285.

46. Sadrai, M.; Bird, G. R. "A new laser dye with potential for high stability and a broad band of lasing action: Perylene-3,4,9,10-tetracarboxylic acid-bis-N,N'(2',6' xylidyl)diimide." *Opt. Commun.* **1984,** *51* (1), 62-64.

47. Liu, X.; Zhang, N.; Zhou, J.; Chang, T.; Fang, C.; Shangguan, D. "A turn-on fluorescent sensor for zinc and cadmium ions based on perylene tetracarboxylic diimide." *Analyst* **2013,** *138*, 901-906.

48. Tang, T.; Herrmann, A.; Peneva, K.; Müllen, K.; Webber, S. E. "Energy Transfer in Molecular Layer-by-Layer Films of Water-Soluble Perylene Diimides." *Langmuir* **2007,** *23*, 4623-4628.

49. Palermo, V.; Liscio, A.; Gentilini, D.; Nolde, F.; Müllen, K.; Samorì, P. "Scanning Probe Microscopy Investigation of Self-Organized Perylenetetracarboxdiimide Nanostructures at Surfaces: Structural and Electronic Properties." *Small* **2007,** *3* (1), 161-167.

50. Kresse, G.; Furthmüller, J. "Efficiency of ab-inito total energy calculations for metals and semiconductors using a plane-wave basis set." *Comput. Mater. Sci.* **1996,** *6* (1), 15-50.

51. Kresse, G.; Furthmüller, J. "Efficient iterative schemes for ab initio total-energy calculations using a plane-wave basis set." *Phys. Rev. B* **1996,** *54* (16), 11169-11186.

52. Perdew, J. P.; Burke, K.; Ernzerhof, M. "Generalized Gradient Approximation Made Simple." *Phys. Rev. Lett.* **1996,** *77* (18), 3865-3868.

53. Perdew, J. P.; Burke, K.; Ernzerhof, M. "Generalized Gradient Approximation Made Simple [Phys. Rev. Lett. 77, 3865 (1996)] Errata." *Phys. Rev. Lett.* **1997,** *78* (7), 1396.

54. Blöchl, P. E.; Jepsen, O.; Andersen, O. K. "Improved tetrahedron method for Brillouin-zone integrations." *Phys. Rev. B* **1994,** *49* (23), 16223-16233.

55. Methfessel, M.; Paxton, A. T. "High-precision sampling for Brillouin-zone integration in metals." *Phys. Rev. B* **1989,** *40* (6), 3616-3621.

56. Giordano, A. J. "Altering the Work Function of Surfaces: The Influential Role of Surface Modifiers for Tuning Properties of Metals and Transparent Conducting Oxides." Ph.D. Dissertation, Georgia Institute of Technology, 2014.

57. Gliboff, M. "Molecular Level Understanding of Interfaces and Excited State Electronic Structure in Organic Solar Cells Using Soft X-ray Techniques." Ph.D. Dissertation, University of Washington, 2013.

58. Gliboff, M.; Li, H.; Knesting, K. M.; Giordano, A. J.; Nordlund, D.; Seidler, G. T.; Brédas, J.-L.; Marder, S. R.; Ginger, D. S. "Competing Effects of Fluorination on the Orientation of Aromatic and Aliphatic Phosphonic Acid Monolayers on Indium Tin Oxide." *J. Phys. Chem. C* **2013,** *117* (29), 15139-15147.

59. Paniagua, S. A.; Li, E. L.; Marder, S. R. "Adsorption studies of a phosphonic acid on ITO: film coverage, purity, and induced electronic structure changes." *Phys. Chem. Chem. Phys.* **2014,** *16* (7), 2874-2881.

60. Paniagua, S. A.; Baltazar, J.; Sojoudi, H.; Mohapatra, S. K.; Zhang, S.; Henderson, C. L.; Graham, S.; Barlow, S.; Marder, S. R. "Production of heavily n- and p-doped CVD graphene with solution-processed redox-active metal–organic species." *Mater. Horiz.* **2014,** *1*, 111-115.

61. Paniagua-Barrantes, S. A. "Interfacial Engineering of Transparent Conductive Electrodes and Nanoparticles with Phosphonic Acids and Metal-Organic Dopants for Organic Electronic Applications." Ph.D. Dissertation, Georgia Institute of Technology, Atlanta, GA, 2013.

62. Giordano, A. J.; Pulvirenti, F.; Khan, T. M.; Fuentes-Hernandez, C.; Moudgil, K.; Delcamp, J. H.; Kippelen, B.; Barlow, S.; Marder, S. R. "Organometallic Dimers: Application to Work Function Reduction of Conducting Oxides." *ACS Appl. Mater. Interfaces* **2015,** *7* (7), 4320-4326.

63. Zhou, Y.; Shim, J. W.; Fuentes-Hernandez, C.; Sharma, A.; Knauer, K. A.; Giordano, A. J.; Marder, S. R.; Kippelen, B. "Direct correlation between work function of indium-tin-oxide electrodes and solar cell performance influenced by ultraviolet irradiation and air exposure." *Phys. Chem. Chem. Phys.* **2012,** *14*, 12014-12021.

64. Sugiyama, K.; Ishii, H.; Ouchi, Y.; Seki, K. "Dependence of indium-tin-oxide work function on surface cleaning method as studied by ultraviolet and x-ray photoemission spectroscopies." *J. Appl. Phys.* **2000,** *87* (1), 295-298.

65. Helander, M. G.; Wang, Z. B.; Qiu, J.; Greiner, M. T.; Puzzo, D. P.; Liu, Z. W.; Lu, Z. H. "Chlorinated Indium Tin Oxide Electrodes with High Work Function for Organic Device Compatibility." *Science* **2011,** *332*, 944-947.

66. Li, H.; Winget, P.; Brédas, J.-L. "Transparent Conducting Oxides of Relevance to Organic Electronics: Electronic Structures of Their Interfaces with Organic Layers." *Chem. Mater.* **2014,** *26* (1), 631-646.

67. Li, H.; Ratcliff, E. L.; Sigdel, A. K.; Giordano, A. J.; Marder, S. R.; Berry, J. J.; Brédas, J.-L. "Modification of the Gallium-Doped Zinc Oxide Surface with Self-Assembled Monolayers of Phosphonic Acids:A Joint Theoretical and Experimental Study." *Adv. Funct. Mater.* **2014,** *24*, 3593-3603.

68. Li, H.; Duan, Y.; Paramonov, P. B.; Coropceanu, V.; Brédas, J.-L. "Electronic structure of self-assembled (fluoro)methylthiol monolayers on the Au(111) surface: Impact of fluorination and coverage density." *J. Electron Spectrosc. Relat. Phenom.* **2009,** *174*, 70-77.

69. Hwang, J.; Wan, A.; Kahn, A. "Energetics of metal-organic interfaces: New experiments and assessment of the field." *Mat. Sci. Eng. R* **2009,** *64*, 1-31.

CHAPTER 6

CONCLUSIONS AND OUTLOOK

6.1 Synopsis

Recently, organic electronic devices have undergone significant improvements, with the efficiencies of organic photovoltaics climbing rapidly and organic light-emitting displays becoming commonplace in the consumer market. This Thesis has focused on the use of two distinct, but related methods for surface modification to tune the electronic properties of metal and transparent conducting oxide electrodes, particularly gold and ITO. One method is based on physisorbed dopants that are used to treat surfaces (Chapters 3 and 4), where an interface dipole is formed through adsorption of species on the substrate, with charge transfer taking place between the dopant and the surface. In the other approach, chemisorption of phosphonic acids to the surface of the ITO substrate (Chapter 5), in which the degree of charge transfer with the surface supplements the interface dipole, thereby altering accordingly the WF of the surface that is being modified. Phosphonic acids were calculated to increase the WF of ITO by as much as 1.4 eV using perylene diimide (PDI) electron-withdrawing groups. Metal-organic dopants can decrease the WF of both ITO and

gold by 1.2 - 1.3 eV, while *N*-heterocyclic carbenes (NHCs) have been shown to decrease gold's work function by as much as 1.4 eV.

First, we described the adsorption of an organometallic sandwich complex, pentamethyliridocene (IrCpCp*), to gold and ITO surfaces to understand the mechanism of work function modification. As IrCpCp* is applied as a dimer in solution, and XPS spectra show that the monomer is present on the surface,[1] both species were calculated on the surface. The monomer on the surface was calculated to cause a larger decrease in work function than the dimer. The dimer has about half of the charge transferred to the surface as the monomer. While previous work had only hypothesized that such a charge transfer occurs,[1] our work *clearly highlights* it on surfaces with different chemistries. This reduced charge transfer, leads to a smaller interface dipole component, and therefore smaller work function modification for the dimer compared to the monomer. A synthetic byproduct, namely a hydrogen abstraction product of the monomer, was examined for its ability to modify the work function as well. The addition of a hydrogen atom to the ring farthest from the surface did not greatly change the geometry of the monomer with respect to the interaction with the surface, but it did change the electronic structure. The hydrogen abstraction modified monomers led to small decreases of the work function and Bader charges similar to the isolated monomer show that almost no charge was transferred to the surface. The modified monomer on ITO surfaces led to work functions that were almost the same as (on average only 0.03 eV lower than) unmodified ITO. This underlines that the specific features of the electronic structure of the monomer are required for the work function modification observed experimentally.

Next, we illustrated the work function decrease of gold by *N*-heterocyclic carbenes with different structures. The carbenes examined had substituents with different steric bulk and carbene backbones that were either unsaturated or fully saturated. The backbone did not seem to play a large role in the work function modification. The substituents had a larger effect on the total work function decrease than the backbone saturation in our calculations. With the same backbone but different substituents, it was calculated that carbenes with smaller isopropyl groups, led to as much as 0.46 eV larger decreases than those with bulkier diisopropylphenyl groups. The distance of the carbene carbon from the surface was found to be related to the work function change for the carbenes with different substituents. The carbenes with isopropyl groups were closer to the surface and had larger work function reductions than those with diisopropylphenyl groups, which were farther away. The isopropyl carbenes were close enough for the carbene carbon to interact with the surface and showed charge transfer directly from the carbene carbon, as denoted by larger Bader charges when interacting with the gold surface relative to the isolated carbene. Bader charges of the diisopropylphenyl carbenes on the gold surface show that they behave as if they were isolated. The larger distance of the carbene from the surface led to almost no charge transfer. This extra charge transfer for the smaller carbenes with isopropyl groups led to larger interface dipole contributions in the work function modification breakdown, while the other components (molecular dipole and surface reorganization) were on the same order of magnitude across the different variations of backbone and substituents. Further comparison with experiment will be assessed using calculations performed with the molecular coverage within the experimental range determined by XPS.

These calculations will help determine if the difference in work function modifications between the substituents is due to coverage or some other mechanism.

Finally, we examined the effect of the strength of electron withdrawing groups on the work function modification for phosphonic acids on ITO. This was the first time, to our knowledge, that singly PA-modified PDIs have been used as monolayers bound to a surface to cause work function changes. The benzyl phosphonic acids (BPAs) with fluorinated (fluoro and trifluoromethyl) groups generally had similar tilt angles, molecular coverage, and work function increases on the order of 0.1 – 0.2 eV. These work function modifications were achieved through a combination of almost equal contributions from the interface dipole, molecular dipole, and geometrical reorganization of the surface. The BPA with the stronger electron-withdrawing nitro group and the even stronger PDI-PAs had a majority of the work function modification due to the interface dipole. Bader charge analysis shows that the nitro and PDI phosphonic acids have larger charge transfer from the surface than the fluorinated BPAs. When the calculated dipole moment of the PA is plotted against the calculated change in work function, the fluorinated BPAs have a linear trend, as noted in the literature,[2-11] while nitro BPA does not align with this trend, and PDI-PAs are not correlated at all. This lack of correlation is due to the increased charge transfer in the nitro and PDI systems. This work highlights that charge transfer should be considered *in addition to* the molecular dipole for work function modification using PA modifiers.

Overall, the examples in this Thesis have shown the importance of charge transfer (or lack thereof) on the mechanism of work function modification for a range of different systems. Charge transfer has been shown to be important to surface modified systems for modulating the work function, both experimentally[12-15] and computationally.[16] While

charge transfer is not necessary in order to modify the work function, when there is significant charge transfer, Φ will be strongly modified. Increasing charge transfer to or from the surface could be used as a design principle when creating surface modifiers for tuning the effective work function for a particular application. Physisorbed and chemically bound surface modifiers have both shown that charge transfer will impact the interface dipole component of the work function modification breakdown, showing the ubiquity of the principle. Charge transfer has been shown to be a strong influence on the final work function of modified surfaces, even more so than the molecular dipole relative to the surface normal, as has been stated in the literature for phosphonic acid modifiers. [2-11] Many factors must be considered in tandem when tuning the work function of surfaces, and charge transfer is definitely a critical one.

6.2 Future Considerations

While the examples presented in this thesis have focused on organic electronics applications, it is important to put surface modification, in general, into perspective with applications in other areas of research. One such application is in the modification of properties of titanium, including alloys and oxides, for biomedical applications.[17] Modifiers can be applied to the titania (TiO_2) layer in order to increase wettability, surface activity, and adhesion, or even help create an environment where specific cell or tissue response is enhanced by immobilizing peptides, proteins, or growth factors.[17] Surface modifiers can also be a method to graft biomolecules to the surface of medical implants in order to improve the biocompatibility.[17] Another area of research is in sensing applications.[18] Silver nanoparticles with thiol modifiers were used to monitor binding

events to a poly-lysine polypeptide through a shift in surface plasmon resonance.[18] Surface modifiers with judicious choice of the structure can be used in sensors to help bind a desired analyte for detection.[19] The PDI-PAs could be used as a surface modifier in order to help attract analytes with van der Waals forces or potential π-π stacking applications. Also, surface modification is important for corrosion passivation[20] and antifouling applications.[21] Work in multiple different research areas can possibly be explored using the results and insight provided in this Thesis.

Research into the work function modification by molecular dopants presented in Chapters 3 and 4, brings up the question of the nature of the work function change for other common surface modifiers for organic electronics applications. One example that could be examined is the determination of the true nature of the species that causes the work function decrease due to the application of cesium carbonate on electrode materials. Cs_2CO_3 has been shown experimentally to decrease the work-function of different substrates, such as gold,[22] silver,[22] graphene,[23] ZnO,[24] and ITO,[25] leading to more efficient electron collection and injection into the organic compounds used in organic electronic devices, but a theoretical understanding of the nature of the work function modification has not been presented. There has also been a lot of work demonstrating efficiency improvement of organic optoelectronic devices by utilizing Cs_2CO_3 as an additional layer in the device, with some stating its use as an electron transport layer,[22, 26-27] others as a dopant to the organic compounds,[24, 28] and others still as a hole-blocking layer.[29] Calculations may provide some clarity into the function of cesium carbonate in optoelectronic devices, by giving insight to the energy level alignment with the electrode materials and the mechanism of work function modification.

While the function of cesium carbonate in devices is being debated, the nature of the compound that is actually found on the surface is also unknown. Li *et al.* have shown by quartz crystal microbalance that Cs_2CO_3 decomposes into cesium metal, CO_2, and O_2[30], while Huang *et al.* have evidence for the formation of CsO_2 and cesium suboxides[22]. Vaynzof *et al.* propose the presence of Cs metal and oxides, such as Cs_2O, CsO_2, Cs_2O_2 and other suboxides ($Cs_{11}O_3$, Cs_4O, and Cs_7O), but cannot comment on the quantitative presence of these species due to the inhomogeneous distribution near the interface with a polymer layer.[24] Huang *et al.* have identified Cs_2O along with Cs_2O_2 and CsO_2,[31] and others have used XPS to show Cs_2O is formed.[32-33] Even more state that there is decomposition of Cs_2CO_3, but do not go into the determination of the decomposition products.[26, 29, 34] Wu *et al.* claim that XPS data shows that Cs_2CO_3 does not decompose on a gold substrate.[35] Ab intio molecular dynamics could be used to give insight into the decomposition scheme, and classical molecular dynamics could give an idea of the probability of some of the decomposition pathways.

The work of Chapter 5 highlighted the importance of charge transfer on the mechanism of work function modification by phosphonic acids. This can be expanded upon by computationally examining phosphonic acids that have even stronger electron withdrawing groups, such as fullerenes and their derivatives, which are typical electron acceptors in organic photovoltaic devices. Some examples of this type of phosphonic acid have been synthesized and their work functions have been tested.[36] This can serve as a potential extension to the trend observed or it may serve as an additional case that needs to be explained by a more robust understanding of the physics at hand. Additionally, the PDI-

PAs examined in this work could be functionalized to be more electron-accepting, to test the applicability of the observed trend to other systems.

6.3 References

1. Giordano, A. J.; Pulvirenti, F.; Khan, T. M.; Fuentes-Hernandez, C.; Moudgil, K.; Delcamp, J. H.; Kippelen, B.; Barlow, S.; Marder, S. R. "Organometallic Dimers: Application to Work Function Reduction of Conducting Oxides." *ACS Appl. Mater. Interfaces* **2015,** *7* (7), 4320-4326.

2. Hotchkiss, P. J.; Li, H.; Paramonov, P. B.; Paniagua, S. A.; Jones, S. C.; Armstrong, N. R.; Brédas, J.-L.; Marder, S. R. "Modification of the Surface Properties of Indium Tin Oxide with Benzylphosphonic Acids: A Joint Experimental and Theoretical Study." *Adv. Mater.* **2009,** *21*, 4496-4501.

3. Hotchkiss, P. J.; Jones, S. C.; Paniagua, S. A.; Sharma, A.; Kippelen, B.; Armstrong, N. R.; Marder, S. R. "The Modification of Indium Tin Oxide with Phosphonic Acids: Mechanism of Binding, Tuning of Surface Properties, and Potential for Use in Organic Electronic Applications." *Acc. Chem. Res.* **2012,** *45*, 337-346.

4. Paniagua, S. A.; Hotchkiss, P. J.; Jones, S. C.; Marder, S. R.; Mudalige, A.; Marrikar, F. S.; Pemberton, J. E.; Armstrong, N. R. "Phosphonic Acid Modification of Indium-Tin Oxide Electrodes: Combined XPS/UPS/Contact Angle Studies." *J. Phys. Chem. C* **2008,** *112*, 7809-7817.

5. Sharma, A.; Kippelen, B.; Hotchkiss, P. J.; Marder, S. R. "Stabilization of the work function of indium tin oxide using organic surface modifiers in organic light-emitting diodes." *Appl. Phys. Lett.* **2008,** *93*, 163308(1-3).

6. Sharma, A.; Hotchkiss, P. J.; Marder, S. R.; Kippelen, B. "Tailoring the work function of indium tin oxide electrodes in electrophosphorescent organic light-emitting diodes." *J. Appl. Phys.* **2009,** *105*, 084507(1-6).

7. Sharma, A.; Haldi, A.; Hotchkiss, P. J.; Marder, S. R.; Kippelen, B. "Effect of phosphonic acid surface modifiers on the work function of indium tin oxide and on the charge injection barrier into organic single-layer diodes." *J. Appl. Phys.* **2009,** *105*, 074511(1-6).

8. Sharma, A.; Haldi, A.; Potscavage Jr., W. J.; Hotchkiss, P. J.; Marder, S. R.; Kippelen, B. "Effects of surface modification of indium tin oxide electrodes on the performance of molecular multilayer organic photovoltaic devices." *J. Mater. Chem.* **2009,** *19*, 5298-5302.

9. Gliboff, M.; Li, H.; Knesting, K. M.; Giordano, A. J.; Nordlund, D.; Seidler, G. T.; Brédas, J.-L.; Marder, S. R.; Ginger, D. S. "Competing Effects of Fluorination on the Orientation of Aromatic and Aliphatic Phosphonic Acid Monolayers on Indium Tin Oxide." *J. Phys. Chem. C* **2013,** *117* (29), 15139-15147.

10. Ratcliff, E. L.; Garcia, A.; Paniagua, S. A.; Cowan, S. R.; Giordano, A. J.; Ginley, D. S.; Marder, S. R.; Berry, J. J.; Olson, D. C. "Investigating the Influence of Interfacial Contact Properties on Open Circuit Voltages in Organic Photovoltaic Performance: Work Function Versus Selectivity." *Adv. Energy Mater.* **2013,** *3* (5), 647-656.

11. Li, H.; Ratcliff, E. L.; Sigdel, A. K.; Giordano, A. J.; Marder, S. R.; Berry, J. J.; Brédas, J.-L. "Modification of the Gallium-Doped Zinc Oxide Surface with Self-Assembled Monolayers of Phosphonic Acids:A Joint Theoretical and Experimental Study." *Adv. Funct. Mater.* **2014,** *24*, 3593-3603.

12. Osikowicz, W.; Crispin, X.; Tengstedt, C.; Lindell, L.; Kugler, T.; Salaneck, W. R. "Transparent low-work function indium tin oxide electrode obtained by molecular scale interface engineering." *Appl. Phys. Lett.* **2004,** *85*, 1616-1618.

13. Lindell, L.; Unge, M.; Osikowicz, W.; Stafström, S.; Salaneck, W. R.; Crispin, X.; de Jong, M. P. "Integer charge transfer at the tetrakis(dimethylamino)ethylene/Au interface." *Appl. Phys. Lett.* **2008,** *92*, 163302(1-3).

14. Bröker, B.; Blum, R.-P.; Frisch, J.; Vollmer, A.; Hofmann, O. T.; Rieger, R.; Müllen, K.; Rabe, J. P.; Zojer, E.; Koch, N. "Gold work function reduction by 2.2 eV with an air-stable molecular donor layer " *Appl. Phys. Lett.* **2008,** *93*, 243303(1-3).

15. Li, F.; Zhou, Y.; Zhang, F.; Liu, X.; Zhan, Y.; Fahlman, M. "Tuning Work Function of Noble Metals As Promising Cathodes in Organic Electronic Devices." *Chem. Mater.* **2009,** *21*, 2798-2802.

16. Hyla, A. S.; Winget, P.; Li, H.; Risko, C.; Brédas, J.-L. "Work function reduction by a redox-active organometallic sandwich complex." *Org. Electron.* **2016,** *37*, 263-270.

17. Liu, X.; Chu, P. K.; Ding, C. "Surface modification of titanium, titanium alloys, and related materials for biomedical applications." *Mat. Sci. Eng. R* **2004,** *47* (3-4), 49-121.

18. Malinsky, M. D.; Kelly, K. L.; Schatz, G. C.; Van Duyne, R. P. "Chain Length Dependence and Sensing Capabilities of the Localized Surface Plasmon Resonance of Silver Nanoparticles Chemically Modified with Alkanethiol Self-Assembled Monolayers." *J. Am. Chem. Soc.* **2001,** *123* (7), 1471-1482.

19. Mrksich, M.; Whitesides, G. M. "Using Self-Assembled Monolayers to Understand the Interactions of Man-Made Surfaces with Proteins and Cells." *Annu. Rev. Biophys. Biomol. Struct.* **1996,** *25*, 55-78.

20. Zamborini, F. P.; Crroks, R. M. "Corrosion Passivation of Gold by n-Alkanethiol Self-Assembled Monolayers: Effect of Chain Length and End Group." *Langmuir* **1998,** *14* (12), 3279-3286.

21. Bearinger, J. P.; Terrettaz, S.; Michel, R.; Tirelli, N.; Vogel, H.; Textor, M.; Hubbell, J. A. "Chemisorbed poly(propylene sulphide)-based copolymers resist biomolecular interactions." *Nat. Mater.* **2003,** *2* (4), 259-264.

22. Huang, J.; Xu, Z.; Yang, Y. "Low-Work-Function Surface Formed by Solution-Processed and Thermally Deposited Nanoscale Layers of Cesium Carbonate." *Adv. Funct. Mater.* **2007,** *17*, 1966-1973.

23. Kwon, K. C.; Choi, K. S.; Kim, B. J.; Lee, J.-L.; Kim, S. Y. "Work Function Decrease of Graphene Sheet sing Alkali Metal Carbonates." *J. Phys. Chem. C* **2012,** *116*, 26586-26591.

24. Vaynzof, Y.; Kabra, D.; Chua, L. L.; Friend, R. H. "Improved electron injection in poly(9,9'-dioctylfluorene)-co-benzothiodiazole via cesium carbonate by means of coannealing." *Appl. Phys. Lett.* **2011,** *98*, 113306 (1-3).

25. Xu, Z.; Chen, L.-M.; Chen, M.-H.; Li, G.; Yang, Y. "Energy level alignment of poly(3-hexylthiophene): [6,6]-phenyl C_{61} butyric acid methyl ester bulk heterojunction." *Appl. Phys. Lett.* **2009,** *95*, 013301 (1-3).

26. Bolink, H. J.; Coronado, E.; Orozco, J.; Sessolo, M. "Efficient Polymer Light-Emitting Diode Using Air-Stable Metal Oxides as Electrodes." *Adv. Mater.* **2009,** *21*, 79-82.

27. Cheng, G.; Tong, W.-Y.; Low, K.-H.; Che, C.-M. "Thermal-annealing-free inverted polymer solar cells using ZnO/Cs_2CO_3 bilayer as electron-selective layer." *Sol. Energy Mater. Sol. Cells* **2012,** *103*, 164-170.

28. Shinmura, Y.; Yamashina, Y.; Kaji, T.; Hiramoto, M. "Ionization sensitization of doping in co-deposited organic semiconductor films." *Appl. Phys. Lett.* **2014,** *105*, 183306 (1-5).

29. Morii, K.; Kawase, T.; Inoue, S. "High efficiency and stability in air of the encapsulation-free hybrid organic-inorganic light-emitting diode." *Appl. Phys. Lett.* **2008,** *92*, 213304 (1-3).

30. Li, Y.; Zhang, D.-Q.; Duan, L.; Zhang, R.; Wang, L.-D.; Qiu, Y. "Elucidation of the electron injection mechanism of evaporated cesium carbonate interlayer for organic light-emitting diodes." *Appl. Phys. Lett.* **2007,** *90*, 012119 (1-3).

31. Huang, J.-H.; Fang, J.-H.; Liu, C.-C.; Chu, C.-W. "Effective Work Function Modulation of Graphene/Carbon Nanotube Composite Films As Transparent Cathodes for Organic Optoelectronics." *ACS Nano* **2011,** *5* (8), 6262-6271.

32. Liao, H.-H.; Chen, L.-M.; Xu, Z.; Li, G.; Yang, Y. "Highly efficient inverted polymer solar cell by low temperature annealing of Cs_2CO_3 interlayer." *Appl. Phys. Lett.* **2008,** *92*, 173303(1-3).

33. Li, G.; Chu, C.-W.; Shrotriya, V.; Huang, J.; Yang, Y. "Efficient inverted polymer solar cells." *Appl. Phys. Lett.* **2006,** *88*, 253503 (1-3).

34. Sessolo, M.; Bolink, H. J. "Hybrid Organic-Inorganic Light-Emitting Diodes." *Adv. Mater.* **2011,** *23*, 1829-1845.

35. Wu, C.-I.; Lin, C.-T.; Chen, Y.-H.; Chen, M.-H.; Lu, Y.-J.; Wu, C.-C. "Electronic structures and electron-injection mechanisms of cesium-carbonate incorporated cathode structures for organic light-emitting devices." *Appl. Phys. Lett.* **2006,** *88* (15), 152104(1-3).

36. Lacher, S.; Matsuo, Y.; Nakamura, E. "Molecular and Supramolecular Control of the Work Function of an Inorganic Electrode with Self-Assembled Monolayer of Umbrella-Shaped Fullerene Derivatives." *J. Am. Chem. Soc.* **2011,** *133* (42), 16997-17004.